The Geometry of Risk:

Novel Metrics for Assessing Satellite Collision Threats

Anne Baak

The Geometry of Risk:

Novel Metrics for Assessing Satellite Collision Threats

by

Anne Baak

to obtain the degree of Master of Science
at Delft University of Technology,
to be defended publicly on Thursday February 6, 2025 at 09.00 AM.

Student number:	5429986	
Project duration:	May 13, 2024 - February 6, 2025	
Chair:	Dr.ir. M.J. Heiligers	TU Delft
Examiner:	Dr. S. Speretta	TU Delft
Supervisor:	Dr. S. Gehly	TU Delft
Supervisor:	Dr.ir. J. Geul	TNO

Cover: Visualization of satellites passing by each other in a crowded space debris environment generated using Microsoft Designer

An electronic version of this thesis is available at: `https://repository.tudelft.nl/`.

Preface

With this thesis, I conclude an academic journey of eight years, bringing to a close an important chapter of my life. Before diving into the core of this work, I would like to express a few words of gratitude.

I would like to thank my supervisors, Steve and Jacco, for their invaluable guidance and support throughout the project. Steve, your expertise and trust during the project have been incredibly helpful, and I sincerely appreciate your endless patience in explaining the geometry of two orbits to me time and again. Jacco, it has been a privilege to have you as my supervisor for both my internship and graduation at TNO. Your guidance has been instrumental in my growth as a researcher and has greatly shaped my journey toward graduation. It has been a true pleasure to work with you both. Furthermore, I would like to thank all satellite operators who took the time to complete the survey on data usage in conjunction analysis. Your insights have proven to be invaluable.

Lastly, I would like to express my heartfelt gratitude to my parents, brother, sister and friends for always believing in me and supporting me throughout my entire academic journey. And of course, Jordi, for bringing me so much laughter and joy.

Anne Eline Baak
The Hague, January 2025

Summary

The growing space debris environment poses a significant threat to operational satellites and the future of spaceflight. Due to the high velocities in orbit even a small debris fragment can pose a considerable collision hazard to active satellites. A collision can either destroy satellites, or further increase the already growing debris population. The worst-case scenario is the realization of the Kessler syndrome, in which an unstoppable chain reaction of collisions occurs. As satellites have become an integrated part of society, the accessibility to space should be maintained. Conjunction analysis is focused on analysing close approaches between objects in orbit. This analysis consists of assessing the collision risk at the time of closest approach. To this end, often probabilistic methods are used, which suffer from the fact that very uncertain states will lead to a low probability of collision, a phenomenon described as the dilution effect. Apart from this drawback, satellite operators are required to decide whether to mitigate a risk well before the time of closest approach. However, the time horizon in which this decision can be made reliably, may be too short to adequately plan for a collision avoidance maneuver. This research aimed to study whether novel risk assessment metrics could complement current practices in conjunction analysis. Furthermore, this research set out to explore whether the time horizon available for decision making can be extended or improved. Last, since operators are considered the end-users of the risk assessment metrics, as they have to make the critical decision of whether or not to mitigate a collision risk, the operational application of the novel metrics has been investigated. Specifically, it has been studied how operators would prefer new metrics to be presented to them. The study aimed to understand their perspectives and to ensure that proposed metrics are not only theoretically valuable but also operationally relevant.

To determine how conjunction analysis can be improved, current practices used in conjunction analysis have been analysed and evaluated, along with the limitations thereof. This has been done using various test cases, including simulated collisions, near misses, and large misses, for both satellite and debris combinations. It has been found that the probability of collision metric works well for high-relative velocity conjunctions if the uncertainty on the states is small, as expected. However, for larger state uncertainties, the probability becomes diluted and the risk is often underestimated. A metric that can mitigate this effect has already been established, that is, the maximum probability of collision can be used to address the dilution effect. This research investigated the reliability of the metric and identified some limitations.

Potential novel risk metrics that could enhance conjunction analysis have been identified, implemented, and tested on said test cases. The two metrics that have been studied in detail are the outer probability measures metric [21] and the relative orbital parameters metric [19]. The former metric distinguishes random from systematic errors, to mitigate the dilution effect. In current practice, the uncertainty, or the knowledge an operator is missing, is often considered as random. In this approach however, this missing knowledge is treated explicitly as systematic uncertainty. Using this approach, the collision risk can be categorized as safe, unacceptable or undetermined. The metric has a highly conservative nature, as was also found when evaluating the performance of the metric. So, the metric can correctly mitigate the dilution effect, but may lead to more false alarms. Therefore, the metric requires care in its interpretation. The relative orbital parameters metric focuses on the relative geometry of the objects' orbits. Using the geometry, it can be determined whether a risky situation occurs by studying the potential vanishing of the separation in the radial and cross-track directions. The concept is currently already used for formation control, however a meaningful use of the metric for conjunction analysis has found to be difficult to establish. This is due to the complicated interpretation of the metric, the absence of a clear safety threshold, and the large uncertainties in the metric as a result of the initial state uncertainties.

The practical needs of satellite operators were explored through an online survey. It was found that when presenting new risk analysis metrics, transparency and replicability of the metrics are of utmost importance. The conservative nature of each metric is inherent to its design. This means that every metric should be interpreted differently, based on how the metric handles uncertainty and balances risk. This can complicate the decision-making process when one is presented with multiple metrics, underscoring the importance of having transparency in the process of the risk quantification.

Contents

List of Figures

List of Tables

Nomenclature

Abbreviations

Abbreviation	Definition
18SDS	18^{th} Space Defense Squadron
19SDS	19^{th} Space Defense Squadron
ANCAS	Alfano Negron Close Approach Software
ASAT	Anti-Satellite
BS	Bulirsch–Stoer
BSK	Big Sky Theory
CA	Conjunction Analysis
CARA	Conjunction Assessment Risk Analysis
CATCH	Conjunction Assessment Through Chebsyshev Polynomials
CCSDS	Consultative Committee for Space Data Systems
CDF	Cumulative Distribution Function
CDM	Conjunction Data Message
CNES	Centre National D'études Spatiales
COLA	Collision Avoidance
CPP	Chebsyshev Proxy Polynomials
CRASS	Collision Risk Assessment
CW	Clohessy Wiltshire
DISCOS	Database and Information System Characterising Objects in Space
DLR	Deutsches Zentrum für Luft- und Raumfahrt
ECI	Earth-Centered Inertial
ESA	European Space Agency
EU	European Union
EUSST	European Union Space Surveillance & Tracking
GEO	Geostationary Orbit
GNSS	Global Navigation Satellite System
HAC	High Accuracy Catalog
HBR	Hard-Body Radius
HEO	Highly-Elliptical Orbit
HRE	High-Risk Event
JAXA	Japan Aerospace Exploration Agency
KS	Kolmogorov–Smirnov
LEO	Low Earth Orbit
MD	Miss Distance
MEO	Medium Earth Orbit
N/A	Not Applicable
NASA	National Aeronautics and Space Administration
NEO	Near Earth Objects
OEM	Orbit Ephemerides Message
O/O	Owner/Operator
OPM	Outer Probability Measures
PDF	Probability Density Distribution
PM	Point Mass
RAAN	Right Ascension of the Ascending Node
RE	Relativistic Effects
RKDP	Runge-Kutta Dormand–Prince

Abbreviation	Definition
RK	Runge-Kutta
RKF	Runge-Kutta-Fehlberg
RP	Radiation Pressure
RTN	Right, Tangential, Normal
SSA	Space Situational Awareness
SBO	Surrogate-Based Optimization Method
SDK	Software Development Toolkit
SDO	Space Debris Office
SGP4	Simplified General Perturbations Model 4
SP	Special Perturbations
SPH	Spherical Harmonics
SSN	Space Surveillance Network
STM	Space Traffic Management
TCA	Time of Closest Approach
TDX	TanDEM-X
TIRA	Tracking and Imaging Radar
TLE	Two Line Element
TRACCS	Traffic Coordination System for Space
TSX	TerraSAR-X
TUDAT	TU Delft Astrodynamics Toolbox
UNOOSA	United Nations Office for Outer Space Affairs
US	United States
USSTRATCOM	United States Strategic Command
WSPRT	Wald Sequential Probability Ratio Test

Symbols

Symbol	Definition	Unit
$\mathbf{A}$	Companion matrix	[-]
a	Semi-major axis	[m]
$\breve{a}$	Lower bound interval on which nodes are defined	[-]
a_j	Coefficients used to defined CPP	[-]
B	Integer number of sections	[-]
$\breve{b}$	Upper bound interval on which nodes are defined	[-]
C_d	Drag parameter	[-]
C_r	Radiation pressure coefficient	[-]
d	Distance metric	[m]
E	Eccentric anomaly	[rad]
e	Eccentricity	[-]
$\vec{e}$	Eccentricity vector	[-]
e_i	i^{th} Eigenvalue	[-]
$f(t)$	Distance function	[m]
$\dot{f}(t)$	Time derivative of distance function	[ms^{-1}]
$\ddot{f}(t)$	Second time derivative of distance function	[ms^{-2}]
$g(x)$	General function	[-]
g_k	Samples from $g(x)$	[-]
$g_N(x)$	CPP for general function	[-]
$\mathbf{H}$	Design matrix	[m, ms^{-1}]
$\vec{h}$	Angular momentum vector	[m^{2}s^{-1}]
i	Inclination	[rad]
J	Cost function	[-]
j	Point index	[-]

Symbol	Definition	Unit
k	Sample number	[-]
L	Arbitrary scale factor	[-]
l	Integer equal to 1 or 2	[-]
M	Mean anomaly	[rad]
N	Order of polynomial	[-]
$\mathcal{N}$	Gaussian probability density function	[-]
$\bar{\mathcal{N}}$	Gaussian possibility function	[-]
N_c	Sub-sample set size	[-]
$\dot{N}_c$	Expected collision rate	[s^{-1}]
N_R	Number of iterations for sub-sample set size	[-]
N_s	Sample size	[-]
$\mathbf{P}$	Covariance matrix	[m^2, $\mathrm{m}^2\mathrm{s}^{-4}$]
$\mathbf{P}_0$	Initial Covariance matrix	[m^2, $\mathrm{m}^2\mathrm{s}^{-4}$]
P_c	Probability of collision	[-]
$P_{c_{Elrod}}$	Probability of collision formulated by Elrod	[-]
$P_{c_{Foster}}$	Probability of collision formulated by Foster and Estes	[-]
$P_{c_{initial}}$	Probability of collision as a result of unscaled $\mathbf{P}$	[-]
$P_{c_{max}}$	Maximum probability of collision	[-]
$P_{c_{Hall}}$	Probability of collision formulated by Hall	[-]
$P_{c_{MC}}$	Probability of collision formulated using Monte Carlo	[-]
$P(R)$	General probability distribution function	[-]
$\bar{P}(R)$	Outer Probability Measure	[-]
$\mathbf{P}_{xx}$	Covariance matrix of parameters $\vec{x}$	[m^2, $\mathrm{m}^2\mathrm{s}^{-4}$]
$\mathbf{P}_{yy}$	Measurement noise covariance matrix	[m^2, $\mathrm{m}^2\mathrm{s}^{-4}$]
p	Semi-latus rectum	[m]
$p(x)$	General probability	[-]
$\mathbf{Q}$	Matrix with the uncertainties in acceleration	[$\mathrm{m}^2\mathrm{s}^{-4}$]
$\hat{s}$	Unit vector of the cross product of $\vec{h}$ and $\vec{r}$	[-]
$\mathbf{R}$	Rotation matrix	[-]
R	Subset	[-]
$\vec{r}$	Position vector	[m]
$\vec{r}_d$	Miss distance vector	[m]
r_d	Miss distance	[m]
r_{d_x}	Miss distance in x direction	[m]
r_{d_y}	Miss distance in y direction	[m]
r_{d_z}	Miss distance in z direction	[m]
r_i	Sample in radius	[m]
$r_{N_{d_x}}$	CPP for miss distance in x direction	[m]
$r_{N_{d_y}}$	CPP for miss distance in y direction	[m]
$r_{N_{d_z}}$	CPP for miss distance in z direction	[m]
T	Orbital period	[s]
T_{min}	Minimal orbital period	[s]
t	Time	[s]
t_0	Initial time	[s]
t_{TCA}	Time of closest approach	[s]
U_c	Credibility	[-]
u	Argument of latitude	[rad]
$\vec{\tilde{u}}$	Vector defined for distance metric	[m]
$\mathbf{V}$	Column matrix of eigenvectors	[-]
$\vec{v}$	Velocity vector	[ms^{-1}]
$\vec{\tilde{v}}$	Vector defined for distance metric	[m]
v_x	Velocity in x	[ms^{-1}]
v_y	Velocity in y	[ms^{-1}]
v_z	Velocity in z	[ms^{-1}]

Symbol	Definition	Unit
$\mathbf{W}$	Weight matrix	[-]
$\vec{\bar{w}}$	Vector defined for distance metric	[m]
X	Random variable	[-]
x	Position in x	[m]
$\vec{x}$	Orbital state	[m, ms^{-1}]
x^*	Roots for which $g(x)$ equals zero	[-]
$\vec{x}_d$	Deviated state	[m, ms^{-1}]
$\bar{\vec{x}}_d$	Mean deviated state	[m, ms^{-1}]
$\vec{x}_{d_i}$	Deviated state sample	[m, ms^{-1}]
x_j	Chebsyshev-Gauss-Lobatto nodes	[-]
x_k	Data samples for $g(x)$	[-]
y	Position in y	[m]
$\vec{y}$	Vector of observations	[m, rad]
z	Position in z	[m]
Γ	Subinterval	[s]
$\mathbf{\Gamma}$	Time component for noise matrix	[s^2, s]
Δa	Drift in semi major axis	[m]
Δe	Drift in eccentricity	[-]
$\Delta\vec{e}$	Relative eccentricity vector	[-]
Δi	Drift in inclination	[rad]
$\Delta\vec{i}$	Relative inclination vector	[-]
$\Delta\vec{r}$	Linearization error for covariance propagation	[m]
$\Delta\vec{r}_{95\%}$	Linearization error 95th percentile	[m]
$\Delta\vec{r}_i$	Linearization error for a sample	[m]
$\Delta\vec{r}_{L_i}$	Deviated sampled position for linear analysis	[m]
$\Delta\vec{r}_{MC_i}$	Deviated sampled position for Monte Carlo analysis	[m]
Δr_N	Separation in cross-track direction	[m]
Δr_R	Separation in radial direction	[m]
Δr_T	Separation in-along direction	[m]
Δt	General timestep	[s]
Δt_{back}	Time backpropagated	[s]
Δu	Drift in argument of latitude	[rad]
Δx_{ij}	Sampled x deviation	[m]
$\Delta\vec{x}_K$	Difference in states in Keplerian elements	[m, rad]
$\Delta\vec{x}_L$	Deviation for linear analysis	[m, ms^{-1}]
$\Delta\vec{x}_{L_i}$	Deviated samples for linear analysis	[m, ms^{-1}]
$\Delta\vec{x}_{MC_i}$	Deviated samples for Monte Carlo analysis	[m, ms^{-1}]
Δy_{ij}	Sampled y deviation	[m]
$\Delta\gamma$	Angle separation	[rad]
$\Delta\Psi$	Variable defined for distance metric	[rad]
$\Delta\Omega$	Drift in RAAN	[rad]
$\Delta\omega$	Drift in argument of perigee	[rad]
$\Delta\%_{KS}$	Allowed change in KS	[-]
$\Delta\%_{\Delta\vec{r}}$	Allowed change in linearization error	[-]
$\Delta\%_{\Delta\gamma}$	Allowed change in angle separation	[-]
δ	Integer equal to 1 or 2	[-]
δ_e	Norm of relative eccentricity vector	[-]
δ_i	Norm of relative inclination vector	[-]
$\vec{\varepsilon}$	Residuals	[m]
ζ	Interpolation matrix	[-]
$\vec{\eta}$	Vector defined for distance metric	[m^{3}s^{-2}]
θ	Angle used to define the relative inclination vector	[rad]
θ_j	Sample in angle	[rad]
λ_{clip}	Clipping threshold	[-]

Symbol	Definition	Unit
$\boldsymbol{\lambda}_{clipped}$	Diagonal matrix of clipped eigenvalues	[-]
$\boldsymbol{\lambda}_{init}$	Diagonal matrix of initial eigenvalues	[-]
λ_{init_i}	Individual eigenvalue	[-]
μ	Earth gravitational parameter	[$\mathrm{m^3s^{-2}}$]
$\mu_{\Delta\gamma}$	Mean of angle separation	[rad]
ν	True anomaly	[rad]
$\vec{\xi}$	Vector defined for distance metric	[$\mathrm{m^3s^{-2}}$]
σ_N	Uncertainty in N	[m]
σ_R	Uncertainty in R	[m]
σ_T	Uncertainty in T	[m]
σ_x	Uncertainty in x	[m]
σ_y	Uncertainty in y	[m]
σ_z	Uncertainty in z	[m]
$\sigma_{\ddot{x}}$	Uncertainty in $\ddot{x}$	[$\mathrm{ms^{-2}}$]
$\sigma_{\ddot{y}}$	Uncertainty in $\ddot{y}$	[$\mathrm{ms^{-2}}$]
$\sigma_{\ddot{z}}$	Uncertainty in $\ddot{z}$	[$\mathrm{ms^{-2}}$]
$\sigma_{\Delta\gamma}$	Uncertainty in angle separation	[rad]
τ_a	Lower boundary risk assessment interval	[s]
τ_b	Upper boundary risk assessment interval	[s]
$\boldsymbol{\Phi}$	State transition matrix	[-]
φ	Angle used to define the relative eccentricity vector	[rad]]
Ω	Right ascension of the ascending node	[rad]
ω	Argument of perigee	[rad]

1 Introduction

In 2009, the first accidental collision between two intact satellites in-orbit took place. The American Iridium-33 satellite and the Russian Kosmos2251 satellite had a relative speed of 11.7 km/s when colliding in Low Earth Orbit (LEO). The collision was estimated to cause the generation of at least 2300 trackable pieces of debris, and both satellites were destroyed [27]. The risk of satellite collisions was a subject of discussion even before spaceflight became reality, initially focusing on impacts with natural satellites such as meteoroids. Some history on this matter has been described by Hall [41]: due to the concern of having a spacecraft impact with a celestial object, a search for natural satellites orbiting the Earth began. The search project ran from 1953 up until 1958 and was conducted using optical telescopes. During this period, no evidence suggested the existence of objects that could possibly endanger spaceflight. Thus, spaceflight was deemed safe from the potential risk of impacting with natural satellites [41]. Then, the space race began with Sputnik 1 launched in 1957. During this period, a competition initiated between the United States and the Soviet Union to achieve breakthroughs in space exploration. This led to the first manned spaceflight in 1961 [60] and the first landing on the Moon in 1969 [61]. The space race also led to a fast increase in the number of satellites present in space, introducing the chance of collisions between artificial satellites. In 1978, a problematic scenario in which satellite collisions would lead to an unstoppable chain reaction of collisions, reducing access to certain regions of Earth orbit, was suggested by Kessler et al. [49]. Contrary to this worrisome theory, others believed in the so called Big Sky Theory (BSK). The Big Sky Theory philosophized that due to the immensity of space and the relatively small size of the objects launched into it, the probability of collision between man-made objects is near zero [64]. The theory proved false after the former mentioned first accidental collision in 2009 and thus it can be concluded that the sky is not big enough to prevent in-orbit collisions [64]. At present, the high number of satellites launched into space and the expansion of the space debris population yield an increasing collision risk between any of these objects. This poses a significant threat to spaceflight operations, as a collision could cause the destruction of operational satellites and the generation of even more debris fragments. When new debris fragments are created, this may in its turn again lead to an even higher collision risk, as envisioned by Kessler et al. [49]. The occupation of space objects in highly populated orbits has gone from nearly zero to a problematic number of objects in the short time span of fifty-five years [41].

As mentioned, there are multiple different reasons for the growing number of objects present in space. The space debris population is defined by ESA as “all non-functional, human-made objects, including no longer functioning spacecraft or fragments of them, in orbit or reentering Earth’s atmosphere” [28]. The space debris environment arises due to various reasons. First, nonactive satellites can stay in their orbit for a very long time, depending on the altitude at which they are orbiting. For example, the second American satellite to ever be launched (Vanguard 1) is still in orbit and is estimated to stay there for another 200 years [41]. Second, debris fragments can be generated through in-orbit collisions, mission-related fragmentation, or satellite break-ups (e.g. explosions) [41]. Moreover, so called anti-satellite (ASAT) tests are conducted to test anti-satellite weapons and to demonstrate the capability of destroying satellites, causing numerous amounts of space debris fragments. The first ASAT test was conducted in 1959 by the US, only two years after the first satellite ever launched [73]. The Soviets have demonstrated their ASAT capabilities as well [73]. Similarly, China tested their ASAT capabilities on their own defunct weather satellite FengYun 1C in 2007. This event caused the generation of approximately 2000 pieces of trackable space debris [64]. Even 60 years after the first test was conducted in 1959, ASAT capabilities are currently still being tested. That is, in 2021 Russia performed an ASAT test on one of their own satellites, again generating thousands of debris pieces [76]. Space debris fragments generated through an ASAT test or a collision will quickly spread over the orbit in which they are generated. Each fragment poses a significant threat to operational satellites as they all represent potential collision hazards, increasing the overall collision risk. To cite ESA: "Any collision or explosion creating large number of debris pieces would be catastrophic for all satellites sharing a busy orbit – as well as for all spacecraft having to pass through these orbits" [26]. Figure 1.1 shows a representation of the dispersion of the debris fragments generated during the Iridium33-Kosmos2251 collision.

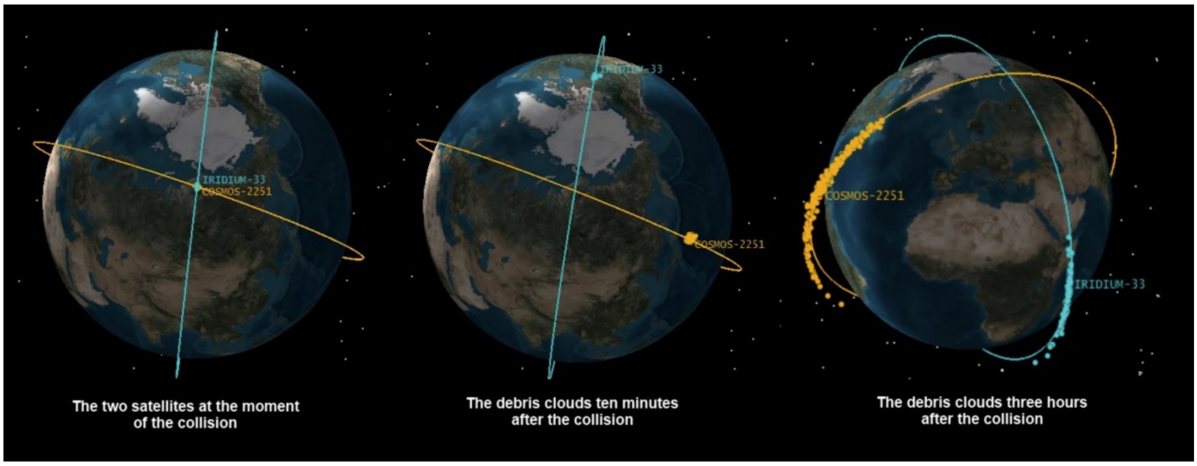

Figure 1.1: Evolution of debris generated after collision of Iridium33 and Kosmos2251, from Reference [58].

As can be seen in the figure, it is only a matter of hours before the fragments are spread out over the orbit. Currently, there are approximately 35,000 space debris fragments with a size larger than 10 cm present in orbit that can be tracked [30]. On top of these tracked objects, there are almost one million objects of a size larger than 1 cm and more than 128 million objects in orbit of sizes larger than 1 mm [30]. Due to the improvement of sensors, such as the new space fence radar, the number of tracked objects will increase [69]. Moreover, the multitude of satellites launched every year could also cause an increase in the number of fragments generated. Figure 1.2 shows the number of objects launched in LEO over the course of time. As can be seen, from approximately 2016 onward, the number of objects has increased drastically due to the rising number of commercial providers.

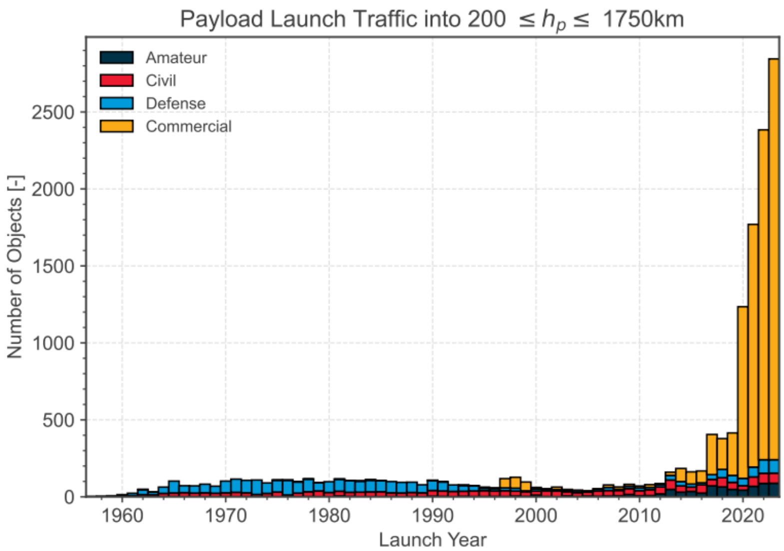

Figure 1.2: Objects launched into LEO over the course of time, from Reference [30].

At present, mega-constellations are launched more often, further increasing the risk of collisions [2]. Figure 1.3 gives an overview of the objects present in space over the course of time. When studying the pink dashed line, representing fragmentation debris, it can be observed that this line shows some steep increases. The in-orbit collision between Iridium33 and Kosmos2251 and the various ASAT tests performed all resulted in the growth of the debris population. The blue line indicates the number of spacecraft present, in which there is also a high increase to be noted. This is due to the rise of constellations and the increase of commercial providers, which could also be noticed in Figure 1.2.

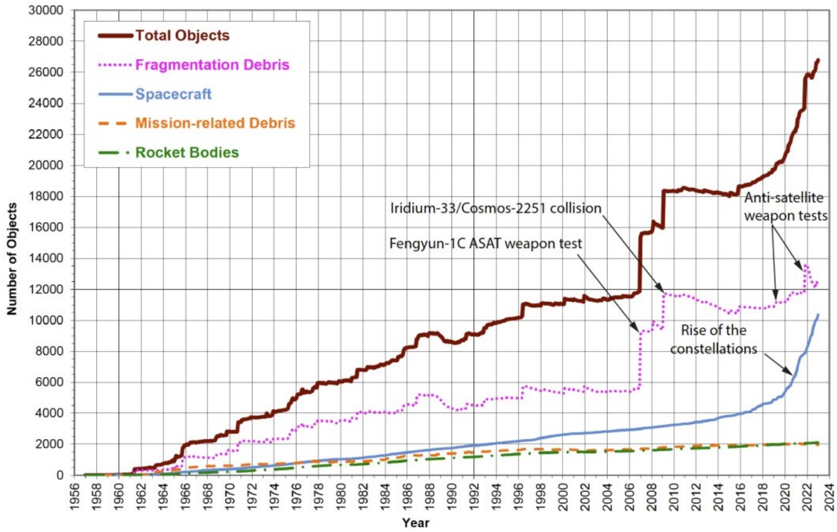

Figure 1.3: Objects in space over the course of time, from Reference [58].

The most problematic scenario resulting from in-orbit collisions is called the Kessler syndrome. The chain reaction that would arise in this scenario is the result of the fact that every collision will cause the generation of debris fragments, which in turn will cause more collisions [49]. To prevent the Kessler syndrome, multiple measures can be taken. First, space debris can be actively removed. An example of active space debris removal is the Clearspace-1 mission, which is planned to launch in 2028. The goal of the mission is to remove the PROBA-1 satellite from its orbit and to make it re-enter and burn up in the atmosphere using robotic arms [25]. Active debris removal is currently still under development and will be prohibitively expensive to apply on a large scale. Second, orbits can be cleared once a satellite reaches its mission end-of-life. The United Nations Office for Outer Space Affairs (UNOOSA) published sustainability guidelines that advise to de-orbit satellites after the mission end-of-life [77]. De-orbiting can either mean that a satellite moves to a graveyard orbit, in other words, an orbit without operational satellites, or that the satellite re-enters back to Earth. Third, new satellites launched into space can be protected from small debris impacts by shielding critical components. Last, the collision risk between space objects can be analysed, such that possible collisions can be prevented using collision avoidance (COLA) maneuvers if necessary and possible. It must be noted that performing unnecessary collision avoidance maneuvers is not desirable due to the limited propellant budget satellites have and the possible interference of the mission objective. This fact emphasizes the need for a reliable risk assessment. All these measures fall under the term Space Traffic Management (STM) [43]. The focus of this thesis will be on analysing the risk of a collision, which is a part of conjunction analysis (CA).

One speaks of a conjunction “when the objects approach one another within a certain distance” [59]. In a conjunction assessment, the catalog of tracked objects is studied, and the collision risk is identified. Since the number of tracked objects (both operational satellites as well as space debris pieces) is high, CA is often divided into multiple steps: screening, analysing, action. The screening part of CA consists of filtering all tracked objects by determining which objects have a realistic potential to collide. This is needed since a complete conjunction analysis of all objects, called an all-on-all analysis, is very inefficient [48]. Possible filters that can be used during the screening process are shown in Figure 1.4. During the second step of conjunction assessment, the analysis stage, the collision risk between two objects is quantified and assessed. This step will be the focus of the research. Last, during the action stage, mitigation measures might be taken.

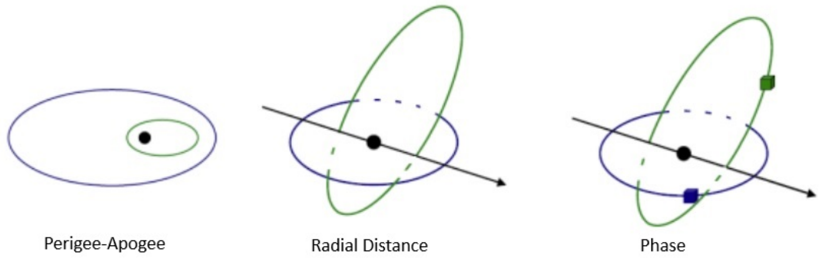

Figure 1.4: Commonly used filters to eliminate impossible conjunctions, adapted from Reference [48].

Spaceflight has become an integrated part of society. Applications of spaceflight are used for science, civil, and military purposes [35] and therefore it is important to maintain the availability of space and avoid the reality of the Kessler syndrome. The research objective of this thesis is to contribute to current conjunction assessment methods. This is done by studying the current practices used in analysing the collision risk and assessing whether these methods can be expanded or improved. In the remainder of this chapter, the current practices of CA are introduced and the limitations thereof are identified. The chapter concludes with the research questions.

1.1. Current Practices in Conjunction Analysis

In this section, the current practices used in conjunction analysis are introduced.

1.1.1. Conjunction Warnings

The United States Strategic Command (USSTRATCOM) tracks satellites and fragments of space debris. Furthermore, USSTRATCOM has been studying conjunction events for US satellites that need to be protected already before the first collision between two intact satellites. After the collision in 2009, the USSTRATCOM has started to study conjunctions for non-US satellites as well, due to the threats that in-orbit collisions yield [69]. Certain warnings (later introduced in more detail) are published when a conjunction is identified, which are used by multiple agencies.

To be able to identify possible conjunctions, first data of the space objects is needed. There are three different types of data available. The first type is observational data. This data type can be a result of radars, optical measurements or satellite laser ranging. The data is often difficult to obtain, therefore it is scarce. Using this observational data, orbital parameters can be set up which can be used to find the state of the object at a certain moment in time. This is the second datatype. Six parameters are needed to describe the orbit of a space object. This description can be given in various different coordinates systems, such as Keplerian elements or Cartesian coordinates for example. The last datatype consists of ephemerides, which give the states of the orbit over a certain time interval. Ephemerides can be used to find the state at certain moments in time by interpolation. One is thus dependent on the time window for which the ephemerides are available. The US Space Surveillance Network (SSN) tracks satellites and space debris objects using sensors located all over the world [1]. The observations generated by the network are used to find the orbital parameters of an object. The orbital parameters are published in the Two-Line Elements (TLEs) format. These TLEs are created by the United States Space Command. TLEs can only be propagated with the semi-analytical Simplified General Perturbations Model 4 (SGP4) propagators and are publicly available on Space-Track. Apart from this publicly available database, for some Space-Track users the Special Perturbations (SP) catalog is accessible. These, more accurate, ephemerides are generated by the 18th Space Defense Squadron (18SDS). As mentioned before, a drawback of using ephemerides is the length of the validity of the data, although there are methods to extend this validity. In this case the data of the SP catalog is valid for three days [48]. Another provider for orbital ephemerides is the company Privateer [66]. The ephemerides are published in the form of Orbital Ephemeris Messages (OEMs). The downside of using Privateer, is that there is no automatic data retrieval available.

Having the orbital data, possible conjunctions between different objects can be studied. When discussing a potential collision between space objects, the object that is operating (and is to be protected) is called the “primary” or the “chief” (subscript 1). The other space object (either another satellite or a fragment of space debris) that is a part of the conjunction is called the “secondary” or “deputy” (subscript 2) [69]. When one has a catalog of available data consisting of owner / operator (O/O) ephemerides, the publicly available TLE catalog, or more restricted catalogs such as the SP one, the complete database can be studied for possible conjunctions between different objects. An all-on-all analysis could be done, but as mentioned in the introduction, this is costly. So often a screening process is conducted in which filters, as shown in Figure 1.4, are used to prevent the analysis of impossible conjunctions. The first filter will for example ensure that no analysis is done for a conjunction between a LEO and a GEO satellite, as it is impossible that these will collide. The conjunction warnings, as introduced briefly before, are generated by the 19$^{\text{th}}$ Space Defense Squadron (19SDS). 19SDS performs conjunction analysis between all objects present in the 18SDS High Accuracy Catalog (HAC) and all objects for which O/O ephemerides are available [1]. The data is analysed for possible conjunctions by propagating the states of the objects for seven to ten days for near-Earth objects (NEO) and deep-space objects respectively [1]. Within these time intervals, the time of closest approach (TCA) and the miss distance (MD) at TCA can be identified. Possible calculation metrics for TCA will be discussed in Section 2.1. For near-Earth objects, the probability of collision is determined as well [1], which will be discussed in more detail in the next subsection. If TCA, MD (and P_c for NEOs) cross certain thresholds, a possible conjunction is identified, and a warning is generated and sent to the operators of the objects involved in the potential collision. The warning generated is called a Conjunction Data Message (CDM). The thresholds used to determine whether a CDM needs to be generated are shown in Table 1.1 [1]. It must be noted that some other organizations also generate their own CDMs, for which other generation criteria might be applicable. The use and regeneration of CDMs by other organizations will be discussed later in this section.

Table 1.1: Basic reporting criteria as defined by the 18$^{\text{th}}$ & 19$^{\text{th}}$ Space Defense Squadron, from Reference [1].

Objects	Space-Track Criteria	Emergency Criteria
Deep Space (GEO/MEO/HEO)	TCA ≤ 10 days Overall MD ≤ 5 km	TCA ≤ 3 days Overall MD ≤ 5 km
Near-Earth (LEO)	TCA ≤ 3 days Overall MD ≤ 1 km $P_c \geq 10^{-7}$	TCA ≤ 3 days Overall MD ≤ 1 km $P_c \geq 10^{-4}$

A CDM contains the following information [17]:

- Primary and secondary objects' positions and velocities at TCA with respect to a reference frame.
- Primary and secondary objects' covariances at TCA with respect to an object-centered reference frame.
- The relative position and velocity of the secondary object with respect to the primary object centered reference frame.
- Information relevant to how all of the above was determined.

The available object database is screened at least once every day for possible conjunctions [1]. For a certain conjunction, the first CDM is usually provided a week before TCA. The message will be updated approximately three times per day until TCA [78]. The closer the event becomes time wise, the more accurate the data of the conjunction will be. This is due to the fact that the propagation time until TCA will decrease, and hence the uncertainty will decrease. Furthermore, additional data may have been collected to refine the orbit estimate and reduce the uncertainty. The most recently updated CDM can be presumed to be the most accurate [78]. The CDM does not provide any advice on whether a collision avoidance maneuver is necessary, it merely serves as a warning. The fast increase of objects in space will also increase the amount of CDMs published [69]. CDMs are available on Space-Track. However, publicly available CDMs as found on Space-Track do not provide all the information present in the original CDM [71].

CDMs are often used as indicators for upcoming conjunctions by many agencies. NASA started with conjunction assessments in 1988 for manned space missions [64]. Operational collision avoidance began in 2005, which was expanded to all unmanned space missions by 2010 [69]. The Conjunction Assessment Risk Analysis (CARA) team at NASA is tasked with studying all conjunctions for non-manned spaceflight [69]. The team uses CDMs as provided by 19SDS and O/O ephemerides that are available to them [48]. Privateer also publishes their own CDMs, which do show more detailed information compared to the ones published on Space-Track. Most of the generation process is not known, however it is stated on their website that NASA CARA's Software Development Kit (SDK) [38] is used for the calculation of the probability of collision [66]. ESA also already studied conjunctions in the mid-1990s [69]. Operational collision avoidance again started a bit later, in 2006. ESA's Space Debris Office (SDO) formerly used the TLE catalog available to scan for conjunctions, but since 2010 they have also been using the CDMs as retrieved from Space-Track [69]. If needed, they can request additional data from the Fraunhofer Tracking and Imaging Radar (TIRA). ESA also provides services and databases that can be used for CA. DISCOS is a database consisting of information on the physical properties of space objects, such as the size and mass [48]. Furthermore, tools are available to predict conjunctions and assess the collision risk, such as CRASS [48]. The DISCOS database is also often used by other agencies, such as DLR for example. DLR previously also used the TLE catalog prior to the CDM generation. Now, DLR uses CDMs as well, together with O/O ephemerides and ESA's DISCOS database [69]. Other agencies, such as CNES and JAXA, additionally use their own catalogs and create their own CDMs [69]. The probability of collision is also often computed by agencies themselves. Agencies commonly use a threshold of $P_c > 10^{-4}$ to identify High-Risk Events (HREs) for which maneuver action should be considered [69]. As of 2021, the European Union Space Surveillance and Tracking (EUSST) became an official sub-component of the EU Space Program. Multiple different services are offered by SST, including collision avoidance, re-entry analysis and fragmentation analysis [31].

1.1.2. Probability of Collision

Multiple different formulations have been established for the calculation of the probability of collision. Many of these formulations are implemented in the open source SDK as developed by the NASA CARA team [63]. The probability of collision can be determined with 2D or 3D analytical calculations or with Monte Carlo techniques [42]. The detailed methods for determining P_c, using these different techniques, are described in Section 2.2. When using analytical techniques, a number of assumptions are required to simplify the calculations. These assumptions will limit the reliability of P_c for certain conjunctions. The assumptions are shown below, such that the corresponding limitations can be studied in further detail.

For 2D analytical calculations, the following assumptions are made [7]:

1. The potentially colliding objects are approximated as spheres. With this assumption, the relevance of the satellite attitude is removed.
2. The relative acceleration is assumed to be much lower than the relative velocity between the objects. Consequently, the relative motion between the objects can be assumed to be linear during the encounter.
3. The errors in position are considered zero-mean, Gaussian, uncorrelated and constant during the encounter.
4. The relative velocity at TCA is assumed to be large enough such that the encounter is short and the velocity uncertainty can be neglected.

For the 3D analytical calculations, the encounter does not need to be linear. In principle, the Monte Carlo analysis does not require any assumptions, although the spherical shape model is still commonly applied, as the attitude at the encounter is likely to be unknown. The different formulations represent a balance between the accuracy and efficiency of the calculations.

Since P_c is used to assess whether a conjunction is risky or not, the problem can be treated statistically. Thus it would be appropriate to define a null hypothesis, where the probability of collision determines whether this hypothesis can be rejected or not [42]. Hejduk et al. have established an appropriate null hypothesis that reads: "The actual miss distance is greater than the hard-body radius" [42]. The hard-body radius (HBR) is defined as the sum of the sizes of the two space objects. When the miss distance is greater than this hard body radius, it means that the two objects are not colliding. The base state is thus that there is no maneuver needed. Hence, if this hypothesis can be rejected, the objects could collide and a maneuver might be needed. The fundamental question that is answered with this null hypothesis is defined as: "Do the presented data justify a decision to mitigate the conjunction?" [42].

1.1.3. Limitations on Current Practices

All conjunction analysis methods have limitations. One important limitation is that during the generation of CDMs, there are many error sources which lead to uncertainties in the identification of a possible conjunction, including:

1. Sensors produce noisy measurements, with errors incurred from signal propagation through the atmosphere and ionosphere, among other sources [69].
2. Uncertainties in the dynamical model will increase the errors when propagating the state. Often states are propagated with a limited dynamical model for efficiency [20].

3. Since debris fragments are generated when already in orbit, the physical properties of these pieces have to be estimated from observations. So, the size, mass, and dynamical parameters are all estimations and thus contribute to the uncertainty of the problem.
4. When a state is propagated, the associated covariance matrix also needs to be propagated. The most accurate method of doing this is with a Monte Carlo algorithm, but this is computationally costly. Instead, local linearization methods can be used, introducing additional errors [52].
5. Estimation of TCA and MD will also initiate an additional error source in the conjunction assessment [22].
6. Unexpected maneuvers of active satellites introduce additional uncertainties [21].
7. The unknown attitude information is a source of uncertainty. This will be discussed further when analysing the limitations arising from the assumptions made in the calculation of P_c.

Researches have also found that the covariance matrices used for the calculation of P_c are often estimated to be smaller than the actual state error distribution. The reason for this is that in the computation of the covariance, no dynamical model errors are taken into account [10]. However, since many possible conjunctions present themselves in LEO, where perturbing forces such as atmospheric drag are dominant, these dynamical errors should be taken into account. The underestimation of velocity uncertainties leads to an underestimation of positional uncertainties of approximately one order of magnitude [10]. It must be noted that according to 19SDS, their P_c calculation overestimates the covariances for safety [1].

Another limitation of current conjunction analysis is the timeliness of the CDMs and conjunction information. An operator would ideally make a decision on whether to perform a collision avoidance maneuver at least one day before TCA. This time is needed to plan the maneuver and check whether the maneuver might be combined with a preplanned station-keeping maneuver, limiting propulsion costs [10]. Furthermore, it must be checked whether the maneuver will not cause additional conjunctions after the satellite has moved [48]. There have been attempts to improve the timeliness of conjunction warnings by studying whether P_c can be predicted forward using machine learning [78].

The calculation of P_c also has a significant amount of drawbacks associated with it. One important drawback of P_c is the number of different assumptions that need to be made for the calculation to hold:

- Assumption 1 states that the shapes of the objects are assumed to be spherical. In a conjunction analysis this can be problematic when the objects have large solar arrays, for example. The rotational attitude of the objects is important to take into consideration.
- Assumption 3 states that the positional covariance is zero-mean Gaussian. This may be true after the initial orbit determination process. However, when propagating the state for a longer time, the error becomes non-Gaussian. Since CA operators need to determine whether a collision avoidance maneuver is needed approximately two days before TCA (and it would be handy to have a first notice approximately one week before TCA) the propagation time may be too long to assume Gaussian behavior. Using Monte Carlo simulations, it has been shown that the effect of this was actually rather small for HREs in LEO [36].
- Assumption 4 states that the velocity at TCA is large and consequently this implies that the encounter time is short. A study has been conducted to test this assumption, carried out by Coppola [18]. As noted in the study, a short encounter assumption is reasonable, but will not hold for all encounters. Namely, the assumption will not hold when an encounter involves formation flying objects and objects in GEO for example. During Coppola's study an all-on-all analysis was done, and based on an encounter duration formula it was tested how often the assumption was actually valid by defining a short-term encounter validity interval. Most potential collisions were found to meet the short encounter requirement needed for the calculation of P_c in its present form. However, there are some cases, when an encounter involves slowly drifting objects for example, that need further investigation [18].

Alfano studied methods for determining P_c without all the aforementioned assumptions [8]. Earlier researchers often note that the calculation of P_c could be performed more accurately when using a Monte Carlo simulation, such as Carpenter [16]. However, as also mentioned by many experts in the field, the accuracy of the method is at the cost of the computational efficiency of the method. For high-fidelity analysis, the computational inefficiency of the algorithm may render the analysis prohibitive [37].

Apart from the limitations arising from the assumptions used for the calculation of the probability of collision, the method of quantifying the risk is also limited due to another phenomenon. The P_c value will namely become less useful when the uncertainties of the states are large. This will lead to a large joint covariance, and thus the probability density will be spread out over a very large area. As a result, due to the spread in the distribution within the covariance ellipsoid, P_c will be low. Whilst this probability of collision is low, it does not mean that the situation is safe, the significance of the value is low due to the uncertain data used to generate it. Hence, no conclusion can be drawn from this value. The effect of finding a low P_c for a high joint covariance is described as the dilution of probability [43]. When a probability is diluted, the value is said to lie in the dilution region. This region defines the range of covariances sizes for which the probability is diluted. To the contrary, when the uncertainty on the states are low, P_c is reliable. Hence, in that case, P_c is said to lie in the robust region [43]. Using the safety threshold for the decision to mitigate a risk, the following conclusions can be made when in diluted or robust regions [43]:

Table 1.2: Conclusions that can be drawn from P_c within the dilution or robust regions, from Reference [43].

	$P_c \geq$ Threshold	$P_c <$ Threshold
Robust region	Risky	Safe
Dilution region	Risky	No Conclusion

The limitation of P_c lies within the existence of these two regions. Although the action needed in the robust region appears clear, the problem lies in the fact that when using P_c, one is not able to separate an uncertain collision from an unlikely one [21]. Returning to the null hypothesis introduced previously, in the dilution region one cannot draw a conclusion as to whether the null hypothesis can be rejected, as can be seen in Table 1.2. When the null hypothesis cannot be rejected, the default state is maintained, and thus no mitigation action is taken. So in the dilution region, even though a low P_c does not necessarily translate to a safe situation, still no action is taken [42]. According to Hejduk et al. this does not have to be a worrisome fact, since objects with highly uncertain states might be categorized as untracked objects. That is, for some objects, no data are available at all and the risk these objects pose is accepted. So, the same may be done for possible conjunctions with data that is too uncertain. However, P_c could also be seen as an insufficiently reliable approach to be the sole decision criteria used to quantify the collision risk [42].

1.2. Research Questions

The problem description given in the previous section has led to the following research question:

How can the conjunction analysis as currently used be further expanded or improved?

This research question can be further divided into multiple sub-questions:

- How can the performance of existing CA methods be improved via the incorporation and combination of novel risk assessment methods?
- Is it possible to extend the risk analysis time horizon, in order to enable reliable decision making further in advance of the potential collision?
- How can the new methods be synthesized to produce useful output for operators?

In the remainder of the thesis one will first be introduced to the theoretical framework that provides the basis of the study. Chapter 2 consists of a description of the algorithm used to find the time of closest approach and the different formulations used to find the probability of collision. In the second theoretical chapter, Chapter 3, the novel metrics that are implemented are introduced. Then, the methodology used for the research is outlined in Chapter 4, followed by the results in Chapter 5. The thesis concludes with the final findings, conclusions, and recommendations in Chapter 6. The appendices provide further analysis and results for complementary studies conducted for the thesis.

2

Theoretical Framework

In this chapter, the various theoretical frameworks used to address the research questions are described. The chapter consists of the algorithm used for the determination of TCA, the different formulations that are currently used for the determination of P_c and an assessment of other statistical risk metrics.

2.1. Time of Closest Approach & Miss Distance

An important part of conjunction analysis is determining the time of closest approach and miss distance between two objects. There are multiple different methods available to achieve this [22]. Denenberg has given an overview of these different methods and has proposed a new one [22]. Methods often consist of root-finding algorithms to find the time for which the derivative of the distance function is zero. One of these methods, called the Alfano Negron Close Approach Software (ANCAS) [4], uses cubic proxy-polynomials to this end. This method is fast, but the estimation can cause inaccurate results [22]. Another method consists of simply propagating the orbits and finding the relative distances at every timestep. Here, the timestep taken needs to be very small, leading to a slow algorithm [22]. These two methods have been combined as the Surrogate-based Optimization method (SBO) [23]. Although the accuracy and speed of finding TCA were increased using SBO, the method still needs a high computational power [22]. The new method suggested by Denenberg tries to find a balance between the drawbacks of the formerly introduced methods. CATCH, or Conjunction Assessment Through Chebsyshev Polynomials uses Chebsyshev Proxy Polynomials (CPPs), as indicated by the name of the algorithm, to again find the roots of the distance function derivative. The difference with the ANCAS algorithm is that simple cubic polynomials are used for ANCAS, whilst CATCH uses CPPs, which are optimized to find the minimal maximum error using root finding, leading to high accuracies whilst still being computationally efficient. The algorithm will be introduced next.

The goal of the algorithm is to find the closest approach between two satellites, thus two orbits. Since the orbits are elliptical, there will be two points in time at which the distances between the orbits is maximal and two points in time at which the distance between the orbits is minimal. This is depicted in Figure 2.1. These four extreme points can all be found in the shortest orbital period of the two periods. This orbital period can then be halved to ensure that at most one local minimal point is found: $\Gamma = \frac{T_{min}}{2} = \frac{\min(T_1,T_2)}{2}$. Here, Γ represents a subinterval and T_1 and T_2 represent the orbital periods of the deputy and chief. The time interval in which to search for the local minimum is then defined as $[t_0, t_0 + \Gamma]$, with t_0 the initial time. When searching for TCA in a seven-day screening period, the search can be conducted using many subintervals. The first interval has been defined above, the second interval is defined as: $[t_0+\Gamma, t_0+2\Gamma]$ and so on, until the last interval given by $[t_0 + (B-1)\Gamma, t_0 + 7$ days $]$, with B the integer number of sections. Only the close approach corresponding to the lowest miss distance could be saved, or one could choose to save all times with approaches below a certain critical distance.

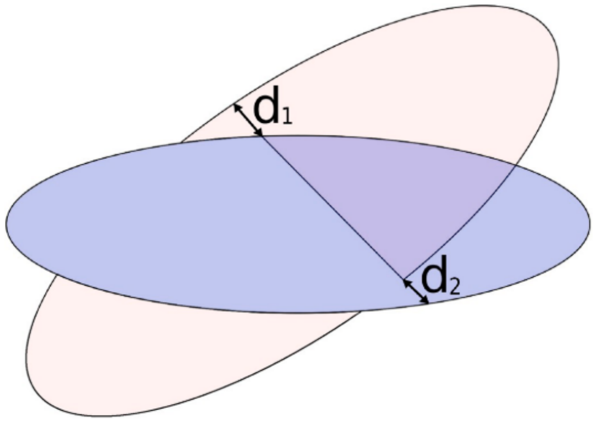

Figure 2.1: The geometry of two orbits, indicating that there are four extreme points, from Reference [22].

Within every subinterval, the extreme points of the distance between the two orbits must be found. This can thus be done by taking the derivative of the distance function and finding the associated roots. The distance function can be defined by [22]:

$$f(t) = \vec{r}_d(t) \cdot \vec{r}_d(t), \text{ with } \vec{r}_d = \vec{r}_1 - \vec{r}_2. \tag{2.1}$$

Here, $\vec{r}_1$ and $\vec{r}_2$ represent the position vectors of the two spacecraft. The local minima can then be found by finding the values t_{TCA} for which:

$$\dot{f}(t_{TCA}) = 0 \text{ and } \ddot{f}(t_{TCA}) > 0. \tag{2.2}$$

Although the function $f(t)$ can be defined as shown in Equation 2.1, the relation for the distance as a function of time $\vec{r}_d(t)$ is not known, so the roots of $\dot{f}(t)$ cannot be found analytically. Hence, a proxy polynomial can be used for which the roots can be found. If the proxy is chosen correctly, these roots will be approximately the same as those of the actual function. A Chebsyshev proxy polynomial is one of the possible proxies that can be used, and this will be done for this algorithm. To find the roots of a general function $g(x)$ defined on the interval $[\breve{a}, \breve{b}]$, the CPP reads [22]:

$$g(x) \approx g_N(x) = \sum_{j=0}^{N} a_j \cos(j \arccos(x)) \left(\frac{2x - (\breve{b} + \breve{a})}{\breve{b} - \breve{a}} \right). \tag{2.3}$$

Here N is the order of the polynomial, j is the point index and $\breve{a}, \breve{b}$ are defined by the interval in which one wants to find the roots. There are many different forms possible for the CPP, which are defined by the coefficients a_j. For every problem, the correct values for these coefficients thus need to be found. To find a_j, samples of $g(x)$ can be taken on certain points x. The ideal points to take the samples on are found using the Chebsyshev-Gauss-Lobatto Nodes, defined as:

$$x_j = \frac{\breve{b} - \breve{a}}{2} \cos\left(\pi \frac{j}{N}\right) + \frac{\breve{b} + \breve{a}}{2}. \tag{2.4}$$

The coefficients a_j can then be found by sampling some data points on the found nodes resulting in the samples $g_k = g(x_k)$, such that:

$$a_j = \sum_{k=0}^{N} \zeta_{j,k} g_k \text{ with } j = 0...N. \tag{2.5}$$

Where $\zeta_{j,k}$ is defined as the interpolation matrix, found by:

$$\zeta_{j,k} = \frac{2}{l_j l_k N} \cos\left(j\pi \frac{k}{N}\right) \text{ where } l_j = \begin{cases} 2, & j = 0, N \\ 1, & \text{otherwise.} \end{cases} \tag{2.6}$$

Now that the coefficients a_j are found, the polynomial is defined. The next step would be to check for tolerance convergence. The order N namely determines how close $g_N(x)$ will be to $g(x)$. Whether N is high enough should be checked by iteration. Denenberg found that $N = 16$ is often sufficiently high enough for a close approximation of TCA [22]. So, for this application, this step can be skipped. The next step is then to find the roots of the proxy polynomial. This can be done by building the companion matrix $\mathbf{A}$ from the CPP coefficients:

$$A_{j,k} = \begin{cases} \delta_{2,k} & j = 1,\ k = 1...N \\ \frac{1}{2}(\delta_{j,k+1} + \delta_{j,k-1}) & j = 2...N-1,\ k = 1...N \\ -\frac{a_{k-1}}{2a_N} + \frac{1}{2}\delta_{N-1,k} & j = N,\ k = 1...N \end{cases} \text{ where } \delta_{q,r} = \begin{cases} 1 & q = r \\ 0 & \text{otherwise.} \end{cases} \tag{2.7}$$

The eigenvalues of the matrix $\mathbf{A}$ represent the roots on the interval $[-1, 1]$, so these eigenvalues need to be rescaled to the search interval $[\breve{a}, \breve{b}]$. With e_i the i^{th} eigenvalue:

$$x^* = \frac{\breve{b} + \breve{a}}{2} + e_i \frac{\breve{b} - \breve{a}}{2}. \tag{2.8}$$

Using this formula, one can find the roots x^* for which $g(x)$ equals zero. This algorithm can be applied to the problem at hand, where $g(x) = \dot{f}(t)$. Therefore solving the roots will determine TCA. The next step is then to find the miss distance at TCA. As found by Denenberg, this can be done by fitting another CPP separately to each component of $\vec{r}_d(t) = (r_{d_x},\ r_{d_y},\ r_{d_z})$. The same order and sampled data as found for the calculation of TCA can be used. Then the CPP of r_{d_x} reads [22]:

$$r_{d_x}(t) \approx r_{N_{d_x}}(t) = \sum_{0}^{N} a_j \cos(j \arccos(t)) \left(\frac{2t - q\Gamma}{\Gamma}\right). \tag{2.9}$$

Here q is the section number containing the minimum. The CPP for the other two components is defined similarly. With t_{TCA} representing TCA the distance can then be found by taking the norm of the components:

$$r_d = \sqrt{r^2_{N_{d_x}}(t_{TCA}) + r^2_{N_{d_y}}(t_{TCA}) + r^2_{N_{d_z}}(t_{TCA})}. \tag{2.10}$$

During this research, the miss distance has been found by propagating the states from t_0 to the established t_{TCA} and calculating the norm of the positional difference between the primary and secondary object.

2.2. Probability of Collision

This section describes various collision risk assessment methods, with a primary focus on the probability of collision. The probability of collision is referred to as "vanilla" P_c by Hejduk et al. [42]. The NASA CARA Software Development Kit [63] has various different calculations of the probability of collision implemented. The 2D probability calculation is implemented using both the formulation developed by Foster and Estes [32] and the one proposed by Elrod [24]. The derivation outlined by Foster and Estes is often used and will thus be discussed in detail. Other implementations of the calculation, such as the 3D metric derived by Hall and a Monte Carlo analysis will also be discussed.

2.2.1. 2D P_c Calculation Foster and Estes

The assumptions used for the 2D probability of collision calculation are already provided in Section 1.1.2. It is important to keep these in mind during this description. To calculate the probability of collision between two objects, both the covariances and states are needed at TCA. Both are provided in CDMs. The covariances are combined into a joint covariance. As a result of Assumption 3 (uncorrelated errors), the joint covariance can be found by summing the individual covariances for both objects [7]. Due to the fact that the encounter duration is short, as per assumption 4, only the positional covariance needs to be taken into account [3]. The joint covariance then forms a covariance ellipsoid in three dimensions. This ellipsoid is typically placed at the center of the primary object. A collision is assumed to occur when the distance between the primary and secondary objects is less than the sum of their two radii [7]. This sum represents the joint size of the objects, called the HBR. The HBR is often defined by the user. For the determination of the HBR, some additional information is needed in addition to the information given in the CDM [43]. Information on the physical properties of an object might be available through O/Os, or ESA's DISCOS database might be used. The HBR is placed at the center of the secondary object. When this secondary object passes through the defined covariance ellipsoid, a tube-shaped path is created, also called the collision tube [7]. This is depicted in Figure 2.2a. A potential collision will take place in the plane perpendicular to the relative velocity vector. The probability perpendicular to this plane approaches unity, so it has no effect on the calculation of the probability of collision (multiplication by 1) [43]. As a result, the calculation can be simplified to a two-dimensional problem. A visualization of the so-called encounter plane can be seen in Figure 2.2b, where the covariance ellipsoid has transformed to a covariance ellipse.

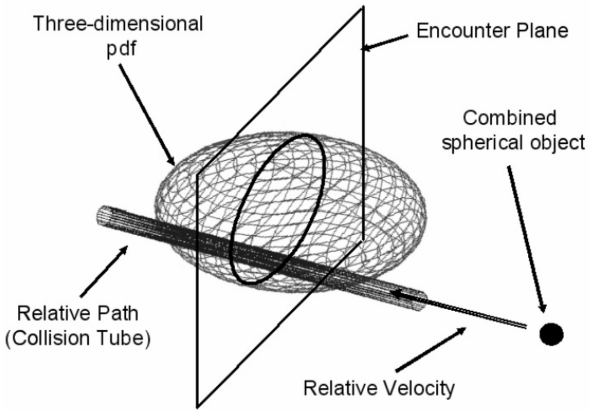

(a) Conjunction encounter visualization, from Reference [7].

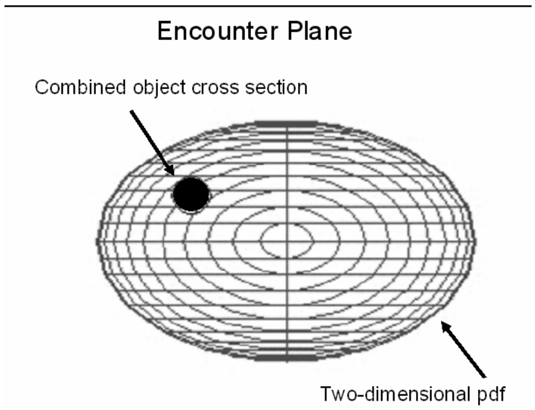

(b) Encounter plane [7], from Reference

Figure 2.2: The approach geometry between two potentially colliding objects, from Reference [7].

Alternately, the encounter plane can be represented by placing both objects on the x-axis, with the HBR placed at the origin. This results in the geometry as depicted in Figure 2.3.

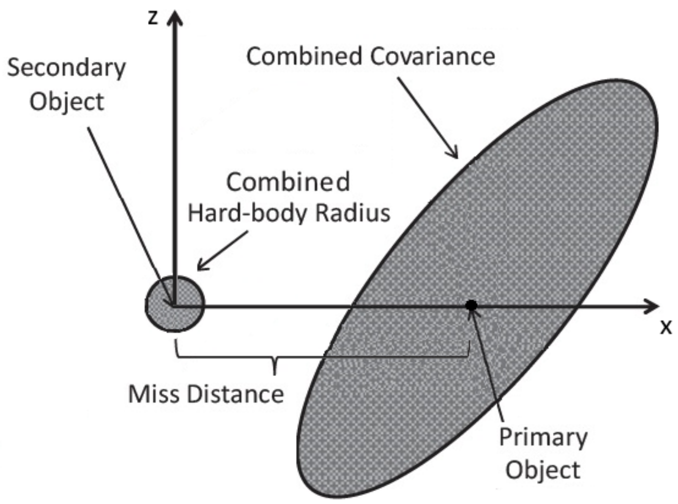

Figure 2.3: Encounter plane for the 2D P_c calculation, adapted from Reference [43].

The covariance ellipse represents the joint state uncertainty, such that the probability of collision can be determined by calculating the extent to which this distribution overlaps with the HBR [43]. Since the ellipse extends to infinity (when not setting a confidence interval), the density function always overlaps with the HBR. The spread of the density function will therefore determine the value of P_c [43]. The probability of collision can then be computed using [63]:

$$P_{c_{Foster}} = \frac{1}{2\pi\sqrt{|\mathbf{P}|}} \int_{-\text{HBR}}^{\text{HBR}} \int_{-\sqrt{\text{HBR}^2 - x^2}}^{\sqrt{\text{HBR}^2 - x^2}} e^{-\frac{1}{2}(\vec{r}-\vec{r}_d)^T \mathbf{P}^{-1} (\vec{r}-\vec{r}_d)} dz\, dx. \tag{2.11}$$

Here $\mathbf{P}$ represents the combined covariances, and the vector $\vec{r}$ and $\vec{r}_d$ are given by: $\begin{pmatrix} x \\ z \end{pmatrix}$ and $\begin{pmatrix} x_1 - x_2 \\ z_1 - z_2 \end{pmatrix}$ respectively [63]. The components x and z are defined in the relative encounter frame, as the secondary object is set at the origin. A summary of the relevant attributes of the Foster and Estes method is provided in Table 2.1, to facilitate later comparison and discussion of the available methods in Chapter 5.

Table 2.1: Relevant attributes for the 2D Foster and Estes calculation.

Objective	Rating	Explanation
Accuracy	-	Limited due to assumptions
Computationally lean	+	The analysis is fast
Mitigates dilution effect	-	2D P_c is affected by the dilution effect
Works for low velocity encounters	-	Rectilinear motion is assumed, so doed not work for low velocity, as for such encounters, the non-linear motion between the objects becomes more significant.

2.2.2. 2D P_c Calculation Elrod

Elrod further simplified the two dimensional calculation of the probability of collision, such that it can be found with even more efficiency [24]. However, the same assumptions as made for the formulation of Foster and Estes hold. Specifically, Elrod uses Cholesky decomposition for covariance matrix factoring, and Chebyshev quadrature for a faster convergence of the integration. The complete derivation for this method can be found in the dissertation of Elrod [24]. This metric is also implemented in NASA CARA's SDK. [63]. Table 2.2 summarizes the relevant attributes of the formulation derived by Elrod.

Table 2.2: Relevant attributes for the 2D Elrod calculation.

Objective	Rating	Explanation
Accuracy	-	Limited due to assumptions
Computationally lean	+	The analysis is fast and more efficient than $P_{c_{Foster}}$
Mitigates dilution effect	-	2D P_c is affected by the dilution effect
Works for low velocity encounters	-	Rectilinear motion is assumed, so does not work for low velocity encounters

2.2.3. 3D P_c Calculation Hall

The 3D calculation of the probability of collision as derived by Hall [37] can be used for single isolated conjunction cases, or cases where multi-encounters can occur. The calculation focuses on using the statistically expected collision rate $\dot{N}_c$ between the two involved objects, which can be calculated based on the uncertainty distributions of the initial states. For the implementation of the formulation in NASA CARA's SDK, it must be noted that the initial states are defined in equinoctial orbital elements, as this mitigates inaccurate covariance modeling [38]. Using the expected collision rate, the number of collisions N_c can be calculated using integration [37]:

$$N_c(\tau_a, \tau_b) = \int_{\tau_a}^{\tau_b} \dot{N}_c(t)dt. \tag{2.12}$$

Here, τ_a and τ_b define the risk assessment interval $\tau_a \leq t < \tau_b$. The statistically expected collision rate $\dot{N}_c(t)$ represents the number of collision expected to occur between the two objects at time t within the time interval [38]. This expected collision rate can be calculated with a Monte Carlo algorithm, or semi-analytically. Conceptually, a 2D $\dot{N}_c$ is calculated for the semi-analytical method, using the uncertainty distributions of the involved objects. This 2D $\dot{N}_c$ is then integrated over time. This way, the metric considers a window of time around TCA in which a collision can occur, instead of just focusing on the encounter plane at TCA. The detailed derivation of $\dot{N}_c$ can be found in the paper written by Hall [37]. When analysing single, isolated, high-relative velocity encounters, the number of collisions is equal to the probability of collision [37]:

$$P_c = N_c(\tau_a, \tau_b). \tag{2.13}$$

For intervals with multiple encounters, or low-relative velocity cases, the following holds [37]:

$$P_c \leq N_c(\tau_a, \tau_b). \tag{2.14}$$

So, the expected number of collisions can exceed the probability of collision. It thus represents an upper boundary for P_c [38]. For multiple encounters, the interval can be divided such that the expected collision rate is only determined for one encounter [37]. There is no need to assume linearity of relative motion (Assumption 2), the equation holds for non-linearity. Table 2.3 summarizes the relevant attributes of the formulation derived by Hall.

Table 2.3: Relevant attributes for the 3D Hall calculation.

Objective	Rating	Explanation
Accuracy	+	Less assumptions so more accurate
Computationally lean	+	The analysis is fast
Mitigates dilution effect	-	3D P_c is affected by the dilution effect
Works for low velocity encounters	+	N_c represents an upper boundary of the probability for low velocity

2.2.4. 3D Monte Carlo P_c Calculation

Foster and Estes have described how a Monte Carlo algorithm can be used to find P_c [32]. That is, a random number generator can be used to sample deviated states using the uncertainty distributions. The conjunction can then be simulated with these deviated states. In the code implemented by NASA CARA, the samples are taken in the equinoctial coordinate frame, taking into account the non-linearity of a satellite orbit. The individual sample pairs may have a different close approach compared to that of the mean samples, so they are propagated forward and backward for short intervals from the mean TCA to find the appropriate pair-wise close approach, deemed proper TCA. The propagation is performed using two-body Keplerian dynamics. If the miss distance at proper TCA is lower than the hard-body radius, a collision is flagged. The probability of collision is then determined using Equation 2.15.

$$P_c = \frac{\text{Number of collisions}}{\text{Number of simulations}}. \tag{2.15}$$

Note, in SDK, the required sample size for the Monte Carlo analysis is determined for every conjunction separately [62]. Table 2.4 summarizes the relevant attributes of the Monte Carlo analysis.

Table 2.4: Relevant attributes for the 3D Monte Carlo calculation.

Objective	Rating	Explanation
Accuracy	+	Accurate results as minimal assumptions are needed
Computationally lean	-	The analysis is slow to run
Mitigates dilution effect	-	When the covariance of the objects is large the resulting P_c will still be low
Works for low velocity encounters	+	No linearity assumptions are needed, so works for low velocity

2.3. Alternatives to P_c and Probability

It must be noted that many other calculations of P_c have been developed over the years. An often used derivation for the 2D P_c calculation is given by Akella and Alfriend [3]. Furthermore, Patera [65] and Alfano [5] have also developed alternative formulations for the 2D calculation of P_c. However, the methods presented in this research are deemed sufficient for this thesis work. The approaches of Akella and Alfriend are conceptually similar to those presented above and suffer the same drawbacks, stemming from the assumptions made and the dilution effect. Furthermore, the methods presented are the ones that are implemented in NASA CARA's Software Development Kit and will thus be used for the calculations carried out in this research.

Apart from the different formulations available to describe the probability of collision, Hedjuk et al. have provided an overview of alternative statistical representations of the collision risk [42]. The different representations are placed on a spectrum ranging from probability to plausibility to possibility. When a metric can be closely described as a probability, it can be said that the metric is a determination or an attempt thereof, to find the actual probability that an event will take place. When a metric leans more to a possibility, the metric tries to determine whether an event is even possible within a certain confidence interval. Metrics that cannot be characterized as quantifying the probability nor possibility, may describe the plausibility of an event [42]. As discussed before, the problem could be addressed statistically due to the probabilistic method of quantifying the collision risk. For the calculation of the vanilla probability of collision, the null-hypothesis and fundamental question have already been introduced in Subsection 1.1.2. This section provides a brief introduction to the different metrics, including their null-hypothesis and associated question, which can be categorized within the probabilistic spectrum of Hejduk et al.

2.3.1. Probability: Wald Sequential Probability Ratio Test

Apart from the vanilla P_c calculation, another possible quantification of the collision risk was suggested by Carpenter and Markley [15]. The method is called the Wald Sequential Probability Ratio Test (WSPRT). The ratio compares the collision risk at hand with the usual collision risk between the objects. The test uses an upper alarm boundary and a lower dismissal boundary. When the ratio falls between the two boundaries, further analysis is needed. A difficulty in the use of WSPRT as risk metric is the background risk value that needs to be calculated additionally. WSPRT is still under the probability part of the spectrum of Hejduk et al. [42], so the same null hypothesis as defined for vanilla P_c can be used. Due to the use of an additional background risk analysis, the fundamental question reads: "Do the presented data and background risk analysis justify a decision to mitigate the conjunction?" [42].

2.3.2. Plausibility: P_c Uncertainty, Maximum P_c and Scaled P_c

The former discussed methods can be characterized under the probability part of the spectrum. Since the probability of collision has its limitations, one might study the plausibility of collision. The metrics introduced in this section, can be categorized under the plausibility segment of the spectrum of Hejduk et al. These metrics are more conservative than the probability metrics.

P_c Uncertainty

A limitation of the calculation of P_c is that the covariance used often does not accurately reflect reality. One way of dealing with this drawback, is to create a multitude of possible covariances. Then, all the different covariances can be used to find a multitude of P_c values. This way, a probability density function of the P_c values can be created. If a large area of the P_c distribution falls above a certain threshold, a mitigation action is needed. The drawback of this method is that for the generation of the P_c distribution, much historical data is needed. This historical data is often not available [42]. The fundamental question for this metric reads: "Given the current data and historical covariance realism information, does the P_c range of values justify a decision to mitigate?". The null hypothesis is given by: "The actual miss distance is greater than the hard-body radius" [42].

2D Maximum P_c Calculation

As mentioned, there are two situations for which P_c is low. Specifically, this occurs in the case for which one is either very certain (and the conjunction is a miss) or very uncertain of the state estimates. This is an inherent consequence of the way in which P_c is calculated, as depicted in Figure 2.4a. As can be seen, for a given MD and HBR, both a large uncertainty (dotted green line) and small uncertainty (dashed blue line) can yield a small P_c when integrating over the HBR. In between these uncertainty distributions, there is an uncertainty that will produce a maximum probability, notionally depicted by the red line. This was demonstrated by Alfano [6].

Figure 2.4b shows the behavior of P_c when scaling the joint covariance and keeping MD and HBR fixed. For a low covariance size, the data is certain, and P_c is thus in the robust region. When the covariance increases, the probability of collision reaches a maximum, after which it will decrease again due to the dilution effect. This maximum P_c can be used to mitigate the dilution effect. So, when one increases or decreases the covariance from either extreme, there is a maximum P_c value to be found somewhere in between. Scaling of the covariances can be done using a brute-force technique [42], so contrary to the WSRT method, no historical data or experience is needed.

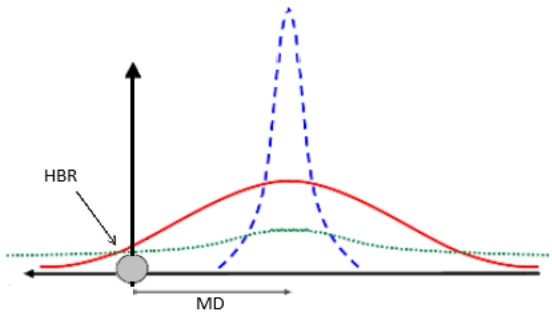

(a) Visualization of P_c calculation, adapted from Reference [48].

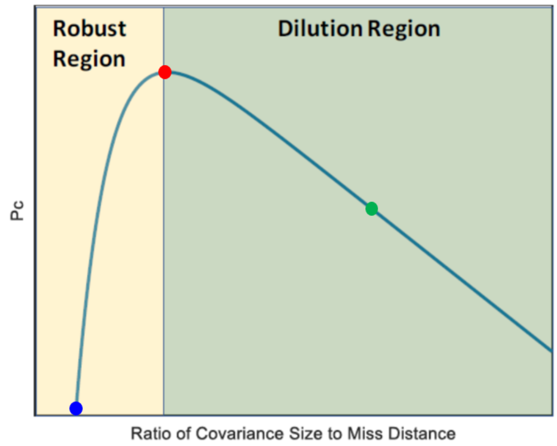

(b) Robust and dilution region, adapted from Reference [63].

Figure 2.4: Explanatory figures for the dilution effect, adapted from References [48] and [63].

The maximum P_c construct is implemented in NASA CARA's SDK. The algorithm first checks whether the conjunction at hand is in the dilution region. This is achieved by calculating P_c using any of the other methods, and comparing this to P_c after scaling either the primary, secondary or joint covariance. If P_c increases as the covariance increases, so $\frac{\partial P_c}{\partial \mathbf{P}} > 0$[1], this means that the object is in the robust region. If P_c decreases as the covariance increases, $\frac{\partial P_c}{\partial \mathbf{P}} < 0$, the probability becomes diluted. When $\frac{\partial P_c}{\partial \mathbf{P}}$ is equal to zero, an extreme has been found, equal to $P_{c_{max}}$. It must be noted that, if both objects are already in the robust region, $P_{c_{max}}$ is taken to be equal to the vanilla P_c calculated based on the current data available, which will be denoted as $P_{c_{initial}}$. This is done as generally, the covariance size will not increase significantly with new data updates [63]. If the objects are not in the robust region, $P_{c_{max}}$ is found using a span of scale factors. This span is refined until $P_{c_{max}}$ is reached [63].

The maximum probability of collision can then be used to test the following null hypothesis: "The actual miss distance is less than the hard-body radius". By rejecting or accepting this null hypothesis, the fundamental question: "Given the data and assumptions regarding possible values of the covariance, does the maximum Pc value justify dismissal of the event?" is answered. If the value is above the threshold, a maneuver can be performed. If it is below it, it can be dismissed at the current time. Since the P_c curve can change due to a changing miss distance per update, the null hypothesis should be tested at every new CDM update. The method has been tested, and it was shown that the number of collision avoidance maneuvers needed doubled compared to the number found when assessing the risk based on vanilla P_c, when analysing a conjunction two days before TCA [43].

Although $P_{c_{max}}$ is not a formulation of vanilla P_c, a table to summarize the relevant attributes of the metric is also presented, shown in Table 2.5. This way, all metrics implemented in NASA CARA's SDK can be compared.

[1] In SDK's documentation, $\frac{\partial P_c}{\partial \mathbf{P}} > 1$ was documented

Table 2.5: Relevant attributes for the 2D maximum P_c calculation.

Objective	Rating	Explanation
Accuracy		Left blank as the metric represents the pessimistic scenario, ensuring mitigation of the dilution effect
Computationally lean	+	The analysis is fast
Mitigates dilution effect	+	Dilution effect is mitigated
Works for low velocity encounters	-	Rectilinear motion is assumed, so does not work for low velocity
Actionable	-	Useful for disregarding some events
Effective	-	Needed twice the maneuvers when testing

Scaling P_c
Instead of creating a multitude of possible covariances based on historical data, as done for the P_c uncertainty metric, one could also define a maximum and minimum covariance based on experience, for both space objects separately. Then it is assumed that all possible covariances for an individual object will lie between the two extreme values defined for that object. Furthermore, a uniform spread of these possible covariances can be assumed over the established region. A grid can then be created using all the possible uncertainties for both objects, to find the associated scaled P_c values [42]. This is depicted in Figure 2.5.

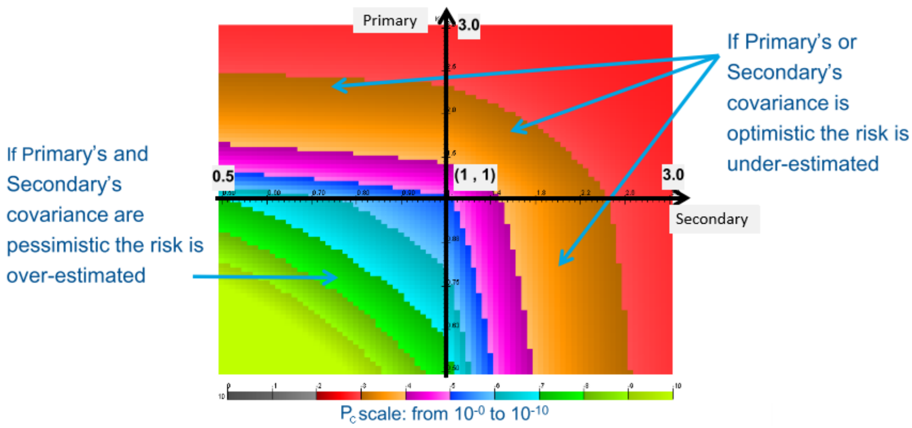

Figure 2.5: Grid of probabilities created for the scaled P_c metric, from Reference [42].

This metric is similar to the maximum P_c metric. This case however uses two different scale factors to adjust the individual covariance matrices, whilst the $P_{c_{max}}$ metric scales either the joint covariance, or only one of the two individual covariances. Furthermore, for this metric, experience is needed to establish the minimum and maximum covariance. The fundamental question for this metric reads: "Given the current data and covariance realism assumptions, do the Pc range of values justify a decision to mitigate?". The null hypothesis is given by: "The actual miss distance is greater than the hard-body radius" [42].

2.3.3. Possibility: Ellipse Overlap

Apart from the probability and plausibility, the possibility of a collision can also be tested. One approach to find the possibility is to use the covariance ellipsoids of both the primary and secondary objects at a given confidence level (e.g. 3σ). It is then checked whether the ellipsoids of the objects overlap, and whether this overlap is above a certain threshold, namely the chosen HBR [42]. The method was developed by Balch et al. [12]. This metric constitutes a conservative approach, whereas for the probability of collision, a larger uncertainty can lead to a reduction of P_c due to the dilution effect. In this case however, a larger uncertainty will result in a larger overlap of the ellipses. The null hypothesis for this method reads: "The covariance ellipses overlap to a non-discountable degree" [43]. The fundamental question answered is given by: "Do the data rule out the possibility of a collision?".

This method has also been tested, and it was found that the number of actions needed increased by a factor of 7.6 when analysing a conjunction two days before TCA [43].

2.3.4. Summary Null Hypotheses and Questions

As a summary, the different metrics and corresponding questions and null hypothesis are presented in Table 2.6.

Table 2.6: Summary of the fundamental questions and null hypothesis, from Reference [42].

Metric	Fundamental Question	Null Hypothesis
Vanilla P_c (Section 2.2)	"Do the presented data justify a decision to mitigate the conjunction" [42]	"The actual miss distance is greater than the hard-body radius" [42]
WSPRT (Section 2.3.1)	"Do the presented data and background risk analysis justify a decision to mitigate the conjunction?" [42]	"The actual miss distance is greater than the hard-body radius" [42]
P_c Uncertainty (Section 2.3.2)	"Given the current data and historical covariance realism information, does the Pc range of values justify a decision to mitigate?" [42]	"The actual miss distance is greater than the hard-body radius" [42]
Maximum P_c (Section 2.3.2)	"Given the data and assumptions regarding possible values of the covariance, does the maximum Pc value justify dismissal of the event?" [42]	"The actual miss distance is less than the hard-body radius" [42]
Scaled P_c (Section 2.3.2)	"Given the current data and covariance realism assumptions, do the Pc range of values justify a decision to mitigate?" [42]	"The actual miss distance is greater than the hard- body radius" [42]
Ellipse Overlap (Section 2.3.3)	"Do the data rule out the possibility of a collision?" [42]	"The covariance ellipses overlap to a non-discountable degree" [42]

3

Novel Metrics

This chapter consists of a description of the proposed novel risk metrics.

3.1. Outer Probability Measures

Probability theory is often used to describe the behavior of events, however it may not always be the most suitable method to do so. In conjunction analysis, employing conventional probabilistic methods to quantify the collision risk inherently frames the collision as a random event [21]. However, a collision event is in fact, not entirely random. That is, when studying a conjunction event, one has to deal with both random and systematic uncertainty. Random uncertainty occurs when the outcome of an event is inherently random, such as when rolling a die or tossing a coin. This randomness can be studied using a Monte Carlo algorithm. For instance, if a balanced die is rolled an infinite number of times, the results will show that each side has a one-in-six chance of being rolled. Thus, by studying the behavior of the die, a probability distribution can be generated. Although this provides some degree of predictability, each roll remains uncertain and independent of other roles. A systematic uncertainty is defined as the uncertainty due to the (missing) level of knowledge, or ignorance, one has of the event. The uncertainty can thus decrease with increasing knowledge [21]. An example of this is when one uses an incorrectly calibrated ruler to measure lengths. If the ruler is said to be 30 cm but in reality is only 28.98 cm, the resulting error will consistently occur each time the ruler is used, and thus the error is predictable. If one learns from this permanent imperfection, this limitation can be compensated for.

Whilst probability theory can be used for events with both systematic and random uncertainties, it assumes an underlying probability distribution for the systematic uncertainty, treating it as random in nature. For scenarios with missing, vague or inconsistent information, other statistical theories may provide a better representation of reality. Among the different alternative methods available are Dempster-Shafer theory, possibility theory and fuzzy logic [14]. Note, the statistical spectrum, as defined by Hejduk et al. (Subsection 2.3), ranges from probability to possibility. Although certain metrics were defined to represent the possibility or plausibility of a collision, they remain probabilistic in nature, due to the assumption of an underlying probability distribution. Therefore, the position of a metric on the spectrum of Hejduk et al. should not be confused with possibility theory mentioned here. Dempster-Shafer theory, possibility theory, and fuzzy logic all have their distinct ways of handling different types of uncertainty. For conjunction analysis, the different uncertainty types occur due to various reasons. For example, random uncertainty can be attributed to measurement noise from sensors used for tracking [21]. The noise is unpredictable and can vary over time. An example of systematic uncertainty is the uncertainty introduced by the choice of the initial orbit determination process used [21]. Specifically, the uncertainty of the state estimate depends on the accuracy of the chosen process. If the process relies on incomplete or incorrect data, for example, this will result in a larger uncertainty for the state estimate. This also implies that, if the accuracy of the process is improved, the state uncertainty will decrease. The uncertainty introduced by the appropriateness of the chosen initial orbit determination process is thus systematic in nature [21]. Furthermore, when perturbing forces are omitted from the dynamical model used to predict the state of an object in time for efficiency, the accuracy of the predicted state is reduced. The uncertainty introduced by this omission is also systematic in nature, as it can be reduced by increasing the model fidelity. A distinct treatment of these different types of uncertainty can be important, because as Cai et al. rightfully question: “how can it be that the probability of collision depends upon our ignorance and the more ignorant we are the less probable the collision might be?" [14].

Delande et al. have developed a holistic approach to treating random and systematic error sources separately, in the form of outer probability measures (OPMs) [21]. Using this framework, one can distinguish an event to be either uncertain or unlikely. This solves the known limitation of using the probability of collision, where a low probability can be a result of both uncertain and unlikely events, due to the dilution phenomenon [21]. Specifically, instead of assuming random behavior, the uncertainty can be used to find the worst-case scenario and the best-case scenario. These worst- and best-case scenarios represent upper and lower boundaries, respectively. With properly formulated information, the observer can be confident that the actual probability lies somewhere in between the two bounds. The range of possible values between the bounds reflects the uncertainty due to the observer's lack of knowledge, which can be defined as ignorance. The lower the ignorance, the closer these two bounds are together. This implies that as the observer gains information, any remaining uncertainty is adequately modeled as random and the possibility distribution converges to a probabilistic description of the event. Using a fully probabilistic description when ignorance is high masks the distinction between random and systematic uncertainty, which can require additional assumptions and impact the validity of conclusions.

The concept of OPMs can be explained using a random die. For a balanced die, the probability of rolling a one ($p(1)$) is equal to $\frac{1}{6}$. Now, consider the case where the side with the number six is substituted with a question mark, which could represent a repeat of the digits one to five, or the original value of six. In this case, what is the probability of rolling a one? The question mark introduces an uncertainty in the problem. For a probabilistic representation, an assumption needs to be made about the underlying distribution of digits represented by the question mark. When the uncertainty introduced by the question mark is assumed to be random (uniformly distributed), the probability of having any number between one and six on the question mark is assumed to be equal to $\frac{1}{6}$. The probability of rolling a one is then equal to $p(1) = \frac{1}{6} + \frac{1}{6} \cdot \frac{1}{6}$. Namely, the player has a one-in-six chance of rolling the side with one, a one-in-six chance of rolling the question mark, and then a one-in-six chance that the question mark represents a one. A more holistic approach to finding the probability of rolling a one is by foregoing any assumption on the nature of the side with the question mark and to compute an upper and lower bound of the probability. Specifically, it is completely certain that the digit one is on one of the sides of the die, so the lower probability of throwing a one is given by $p(1) \geq \frac{1}{6}$. The upper probability can be determined by realizing that the highest probability of rolling a one occurs when the question mark represents a one. In this case, two sides of the die have a one, and therefore $p(1) \leq \frac{2}{6}$. Alternatively, one could rely on the certainty that the digits two, three, four and five can be rolled. This establishes a lower bound for the probability of not rolling a one, given by $p(\neg 1) \geq \frac{4}{6}$. Outer probability measures then use this lower bound to find the upper boundary for the probability of rolling a one, given by $p(1) \leq 1 - p(\neg 1)$ as $p(1) + p(\neg 1) = 1$. Hence, the range in which the actual probability lies is given by:

$$\frac{1}{6} \leq p(1) \leq \frac{1}{3}. \tag{3.1}$$

Here the difference between the upper and lower boundary $\left(\frac{1}{6}\right)$ represents the ignorance introduced by the question mark, reflecting the observer's missing knowledge. The OPM framework uses concepts of Demspter-Shafer theory. In Dempster-Shafer theory, beliefs are used to express the degree of support for a certain outcome, based on an observer's evidence. Furthermore, plausibility is used to represent the degree to which an outcome is possible, considering the evidence that does not contradict it [70]. This plausibility can be calculated using the belief that the outcome will not occur, as done similarly for the upper probability of $p(1)$ in the die example. Together, the belief and plausibility provide an lower and upper boundary describing the uncertainty surrounding the actual outcome.

An OPM can describe the possible probability distribution, based on the knowledge that is available to an observer. The theory behind probability distributions and OPMs will be briefly introduced here, as was described before in the paper written by Delande et al. [21]. For a general case, when a system state is represented by a random variable $X \subseteq \mathbb{R}^d$ with a probability distribution function $P(R)$ with associated probability density function (pdf) $p(x)$, the probability that the state lies in subset R is given by [21]:

$$P(R) = \int_R p(x)dx, \; R \subseteq X. \tag{3.2}$$

The OPM $\bar{P}$ on X can give the bounds of the "subjective" pdf with an upper and lower boundary (subjective as it is "the probability distribution assumed to be that of the system according to the knowledge they possess") [21]:

$$1 - \bar{P}(X \backslash R) \leq P(R) \leq \bar{P}(R),\ R \subseteq X. \tag{3.3}$$

Since random behavior is no longer assumed for the variable X, it can now be described as uncertain, instead of random [21]. Then, $1 - \bar{P}(X \backslash R)$ represent the lower probability, whilst $\bar{P}(R)$ represents the upper probability, also defined as the credibility. Since both bounds represent a probability, the conditions $0 \leq \bar{P}(R) \leq 1$ and $0 \leq 1 - \bar{P}(X \backslash R) \leq 1$ must hold. These values represent the upper and lower probability that the system lies in R according to the observer [21]. Again, the interval between the two boundaries, represents the level of knowledge that the observer does not have, formally referred to as ignorance. Hence when the observer gains knowledge, the ignorance gets smaller [21]. When the system is completely random and there is no knowledge missing, the function becomes a probability function. Note, if the observer's knowledge is incorrect, the function is incorrect as well [21]. Using the upper and lower bounds of the probability, it can then be determined whether the information and data available to an operator are accurate enough to say something meaningful about the collision risk [21]. The risk can be qualified by:

Table 3.1: Conclusions that can be drawn from outer probability measures, from Reference [21].

Risk	Condition
Acceptable	Upper bound $\leq$ threshold
Undetermined	Lower bound $\leq$ threshold $\leq$ upper bound
Non-acceptable	Threshold $\leq$ lower bound

This way, if an operator would set the safety threshold equal to 10^{-4}, and both bounds are below this threshold, this indicates that the conjunction is safe, as one is sure that the highest probability possible is below the set safety threshold (in case that the knowledge available to the observer is correct). To the contrary, if both boundaries are above the threshold, one can be sure that even the lowest probability possible indicates a risky situation (again, in case of correct knowledge), and thus the situation is unacceptable. And last, if the threshold is in between the boundaries, the level of knowledge about the situation is insufficient.

For the application of conjunction analysis, the definition of the upper probability has been derived by Delande et al. This upper boundary can be calculated using possibility theory. The Gaussian possibility function is defined by [21]:

$$\bar{\mathcal{N}}(\vec{r}; \vec{r}_d, \mathbf{P}) = e^{-\frac{1}{2}(\vec{r}-\vec{r}_d)^T \mathbf{P}^{-1}(\vec{r}-\vec{r}_d)}. \tag{3.4}$$

To study the difference between this possibility function and the probability function, the Gaussian probability density function is given below [21]:

$$\mathcal{N}(\vec{r}; \vec{r}_d, \mathbf{P}) = \frac{1}{|\det 2\pi\mathbf{P}|^2} e^{-\frac{1}{2}(\vec{r}-\vec{r}_d)^T \mathbf{P}^{-1}(\vec{r}-\vec{r}_d)}. \tag{3.5}$$

Note the similarity to the Gaussian probability density function employed to compute P_c, as formulated in Equation 2.11. The difference between the behavior of probability distributions and possibility distributions is depicted in Figures 3.1a and 3.1b.

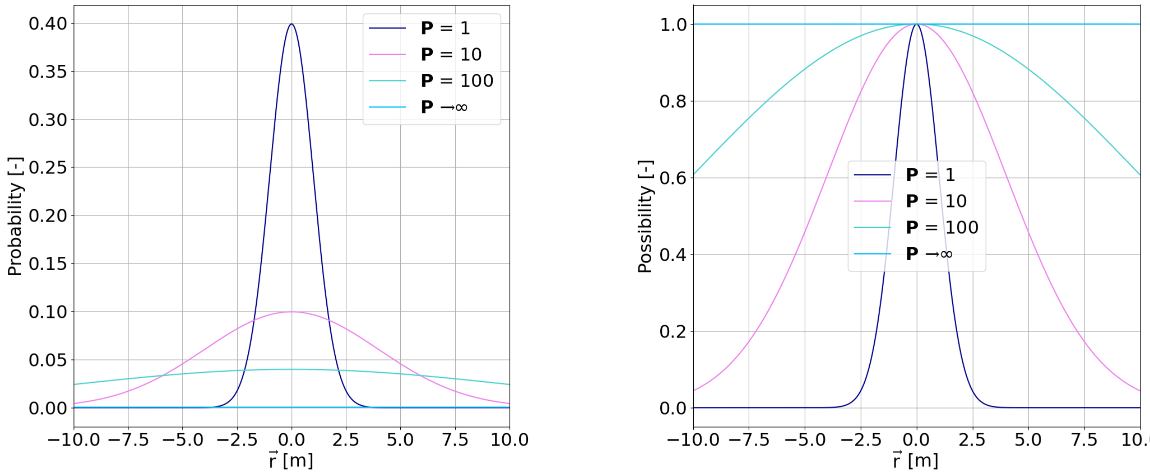

(a) Gaussian probability density function.

(b) Gaussian possibility function.

Figure 3.1: Probability distribution (left) and possibility distribution (right), regenerated from Reference [14].

As can be observed, for an uncertainty approaching infinity, the probability will approach zero and the possibility will approach one for all possible outcomes [14]. A fundamental difference between the distributions is that for probability distributions, all probabilities must add up to one, whereas this is not the case for the possibilities from the possibility distribution. For this reason, when working with a probability density function, one needs to take the integral over the entire relevant area (for CA the HBR, for example) to find the probability, whilst the possibility is determined by the maximum value of $\bar{\mathcal{N}}$ over the region (in this thesis found by sampling). The upper bound of the possibility, also referred to as credibility, can thus be calculated using:

$$U_c(t_f, t_0) = \sup_{\vec{r}\ \in \mathrm{HBR}(\vec{r_d})} \bar{\mathcal{N}}(\vec{r}; \vec{r_d}, \mathbf{P}). \tag{3.6}$$

So, the credibility (U_c) can be determined by sampling points over the HBR, and subsequently calculating the Gaussian possibility for each sample. The credibility is then equal to the maximum of all Gaussian possibilities found, according to Equation 3.6. The samples can be generated using a mesh grid of polar coordinates around the center of the HBR. The coordinates for this center are given by $x_c = ||\vec{r}_d||$, $y_c = 0$, when setting the HBR on the x-axis. Note that this is slightly different from the geometry introduced previously in Figure 2.3, where the HBR was set at the origin, and the covariance was set along the x-axis. Then, to find $\vec{r}$ in Formula 3.4 for each sample, the deviations Δx_{ij} and Δy_{ij} are added to x_c and y_c. These deviations are defined by:

$$\begin{aligned} \Delta x_{ij} &= r_i \cos\theta_j, \\ \Delta y_{ij} &= r_i \sin\theta_j. \end{aligned} \tag{3.7}$$

Here, r_i ranges from 0 m to the size of the HBR, and θ_j ranges from 0° to 360°. The vector $\vec{r_d}$ is set to $(0, 0)$, as for this calculation, the covariance is located at the origin. The geometry of the problem used for this calculation is shown in Figure 3.2, including a visualization of the samples $\vec{r}$ and the possibility contours.

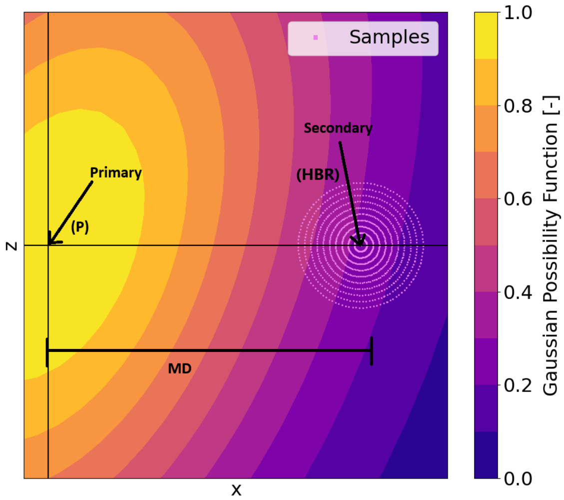

Figure 3.2: Geometry for the calculation of the credibility.

The OPM metric is a very conservative method of assessing the collision risk. The conservative nature indicates that false alarms are favored over false negatives and emphasizes the importance of a nuanced interpretation, in line with Table 3.2 which will be later introduced. The lower boundary of the probability has not been derived yet, however the upper boundary could already be used to mitigate the dilution effect. Namely, if this boundary is below the safety threshold, one can say with certainty that the situation is safe. If the boundary is above the threshold, and vanilla P_c is below the threshold, the situation is undetermined (as the lower boundary of the probability will be below vanilla P_c). When the credibility is above the threshold and vanilla P_c is as well, the situation is risky, as vanilla P_c also indicates this.

Although the maximum P_c construct also provides a method of mitigating the dilution effect, this method does not make the distinction between random and systematic uncertainties. Moreover, the construct scales the covariance to find a more conservative, maximum probability of collision. In contrast, the OPM metric computes a true upper boundary (for properly defined information) by identifying the maximum value of the possibility function over the HBR, representing the worst-case scenario. In literature it has been found that NASA CARA is currently also studying the credibility for use as risk assessment metric and tracking sensor priority metric [39].

3.2. Relative Orbital Parameters

The relative motion between satellites is often used for rendezvous, close proximity or formation flying missions. Using the Clohessy Wiltshire (CW) equations, the relative motion between two satellites can be described if the distance between the two satellites remains small ($r_d \ll 1$) and if both orbits are near circular [81]. Apart from the former mentioned applications, the relative motion between two objects might also be used for conjunction analysis. Specifically, the relative geometry between two orbits can provide information on the direction of the miss distance. From the surveys carried out by Kerr et al., it is apparent that satellite operators would be interested in the geometry of close approaches [48]. Furthermore, the geometry of a conjunction is often already assessed during conjunction analysis by studying in which direction the miss distance is aligned. This alignment could be studied and predicted forward using relative orbital parameters. An advantage of using relative orbital parameters is that the prediction over time will be more stable when using orbital elements, rather than using a Cartesian representation. Namely, for the latter, small changes in the position or velocity can lead to significant variations in the spatial coordinates x, y and z. To the contrary, orbital elements describe the shape and orientation of the orbit, making them less sensitive to small changes in the position and velocity. Due to the stable description that orbital elements provide, their use will lead to more stable solutions for long-term predictions, potentially extending the time horizon of conjunction analysis. The relation between the alignment of the miss distance and relative orbital elements has already been established. D'Amico et al. have derived equations for the relative separation of two objects in the radial, tangential and normal (RTN) frame as a function of their relative eccentricity and inclination vectors. These equations are currently used for the control of formations [19]. Specifically, the vectors are used to ensure that the spacecraft involved do not collide. This concept will be further explained in this section.

Figure 3.3 shows a representation of the RTN directions. The primary is defined at the origin of the reference frame, such that the state of the secondary can be described with respect to the primary.

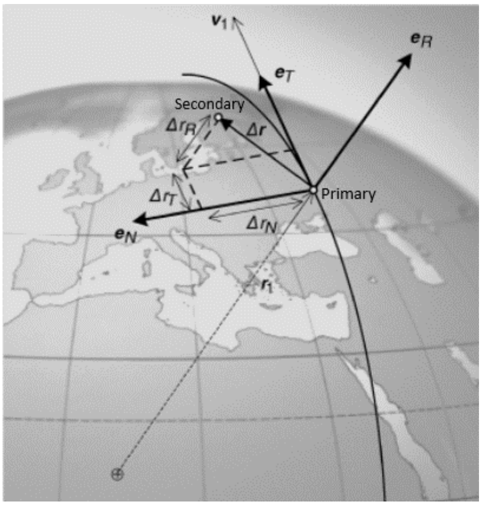

Figure 3.3: Geometry of right, along-track and cross-track directions, adapted from Reference [19].

As can be seen in Figure 3.3 the tangential, or along-track, direction ($\vec{e}_T$) is aligned with the velocity direction of the spacecraft. Due to this alignment, the along-track direction uncertainty increases the most when propagating the state and covariance of a spacecraft. Namely, the initial velocity uncertainty translates into a growing along-track error over time. Furthermore, the velocity direction is influenced by atmospheric drag, which has a large impact on the state of an object. Moreover, maneuver errors have a large influence on the velocity [57]. Due to the fact that the along-track uncertainty is larger than the radial and cross-track uncertainties, a concept has been derived that ensures a separation in either the radial or cross-track direction at all times, as these separations can be established with more certainty. This can be done using relative eccentricity and inclination vectors. It was shown that when the two vectors are parallel to each other, this will yield a maximum radial separation when the cross-track separation is zero and vise versa [19]. This separation will disappear for orthogonal vectors.

The vectors $\Delta\vec{e}$ and $\Delta\vec{i}$ have been derived (Appendix F) and are given by [19]:

$$\Delta\vec{i} = \sin\delta i \begin{bmatrix} \cos\theta \\ \sin\theta \end{bmatrix}, \ \Delta\vec{e} = \delta e \begin{bmatrix} \cos(\varphi) \\ \sin(\varphi) \end{bmatrix}. \tag{3.8}$$

Where δi, δe, θ and φ are defined as shown in Figures 3.4a and 3.4b.

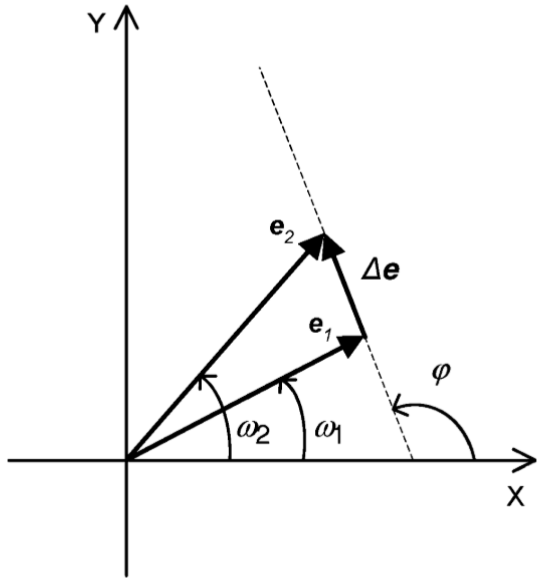

(a) Relative eccentricity vector, from Reference [19].

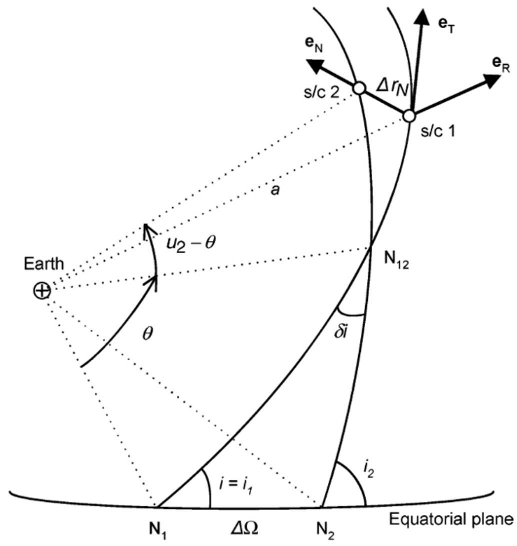

(b) Relative inclination vector, from Reference [19].

Figure 3.4: Visualizations of the relative eccentricity and inclinations vectors, from Reference [19].

Alternatively, the relative eccentricity vector can be visualized as shown in Figure 3.5.

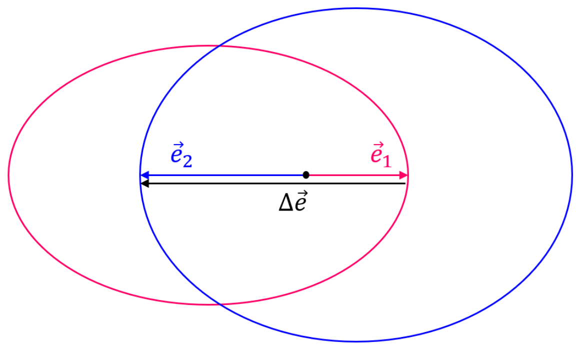

Figure 3.5: Alternative presentation of the relative eccentricity vector.

The vectors are calculated using the mean orbital elements [46]. The alignment of the two vectors can be studied based on the angle between them. The angle deviation $\Delta\gamma$ is given by:

$$\cos \Delta\gamma = \frac{\Delta\vec{i} \cdot \Delta\vec{e}}{||\Delta\vec{i}||||\Delta\vec{e}||} = \cos(\varphi - \theta). \tag{3.9}$$

When $\varphi = \theta$, the resulting angle deviation is equal to zero, and the vectors are thus parallel. When the drift due to Δa and Δu is ignored, the different separations can be given by (see Appendix F for derivation) [19]:

$$\begin{aligned}\Delta r_R &= -a\delta e \cos(u - \varphi),\\ \Delta r_T &= 2a\delta e \sin(u - \varphi),\\ \Delta r_N &= a\delta i \sin(u - \theta).\end{aligned} \tag{3.10}$$

For formation flying satellites, the drift can be ignored as often Δa should be kept very close to zero as a nonzero Δa can induce a drift in Δu [11]. To use these equations for CA, the space objects involved should thus also be bounded. This means that the metric can only be applied to conjunctions involving formation-flying satellites. The relation of these equations to the CW equations has also been derived, as again shown in Appendix F.

Based on these separations, the secondary moves around the primary in an ellipse. This geometry is depicted in Figure 3.6.

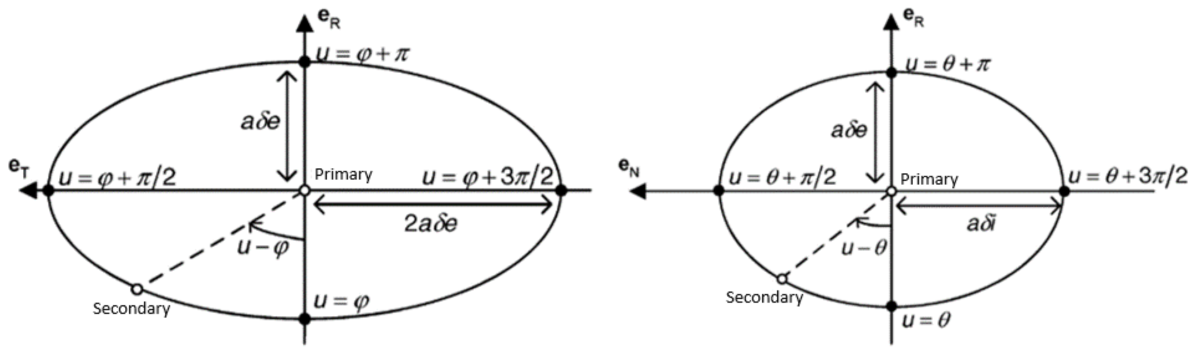

Figure 3.6: Relative motion of the secondary drawn around the primary, adapted from Reference [19].

As can be seen in the figures, there is a maximum radial separation at $u \in \{\varphi,\ \varphi + \pi\}$ and a minimum radial separation at $u \in \{\varphi + \frac{1}{2}\pi,\ \varphi + \frac{3}{2}\pi\}$. For the cross-track separation, the maximum occurs at $u \in \{\theta + \frac{1}{2}\pi,\ \theta + \frac{3}{2}\pi\}$ and the minimum, equal to zero, occurs at $u \in \{\theta,\ \theta + \pi\}$. From this it can be concluded that if $\varphi - \theta = k\pi$, with $k \in \mathbb{Z}$, there is a maximum radial separation equal to $a\delta e$ when the cross-track separation is equal to zero, and there is a maximum cross-track separation equal to $a\delta i$ when the radial separation is zero [19]. The minimal separation in the plane perpendicular to the along-track direction is always greater than the minimum of $a\delta i$ and $a\delta e$ [11]. The lower threshold for the separation can be given by [57]:

$$\sqrt{\Delta r_R^2 + \Delta r_N^2} \geq \frac{a}{2}\sqrt{(\delta e^2 + \delta i^2) - \sqrt{(\delta e^2 + \delta i^2) - 4(\Delta \vec{e}^T \cdot \Delta \vec{i})^2}}. \tag{3.11}$$

When the phasing angle $\varphi - \theta$ equals $k\pi + \frac{1}{2}\pi$, the radial and cross-track separations can be equal to zero at the same time. And as mentioned, due to the uncertainty in the along track direction, the separation in these two directions should never vanish together. According to Equation 3.9, a phasing angle of $\varphi - \theta = k\pi$ means that the relative eccentricity and inclination vectors are parallel to each other, whereas a phasing angle of $\varphi - \theta = k\pi + \frac{1}{2}\pi$ implies that the relative vectors are orthogonal to each other. The geometry of orbits with parallel or orthogonally oriented relative eccentricity and inclination vectors is shown in Figure 3.7 and as can be seen, the orthogonal alignment can lead to a joint vanishing of the R and N separations [19].

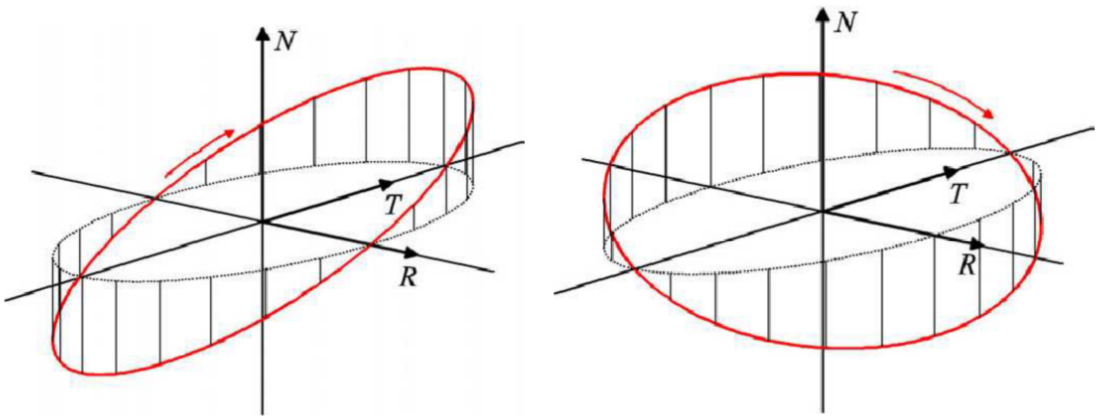

Figure 3.7: Geometry of parallel (left) and orthogonally (right) aligned orbits, from Reference [56].

It can be observed that, for the parallel case, at points in the orbit where R goes to zero, N is maximal and vise versa. Conversely, for the perpendicular case, both R and N go to zero at the same point in the orbit. As mentioned, considering that the concept is used to ensure a safe formation, the concept might also be useful for conjunction analysis. As new data becomes available, the geometry of the two vectors can be evaluated, such that when the vectors move to a more orthogonal geometry, the event can be flagged as risky. Previous research demonstrated the stability of the relative orbital elements in the case of the TerraSAR-X (TSX) and TandemX (TDX) formation, in which a simulated scenario took 25.5 days to transition from a safe to an unsafe condition as a result of orbit perturbations, primarily the second-order zonal coefficient J_2 [19]. Adapting the metric for use in conjunction assessment could therefore potentially extend the time horizon available for decision making. However, it should be noted that if the miss distance is smaller than the HBR, the situation is risky even with a parallel configuration of the relative vectors. This complicates the interpretation of the metric, which will be further discussed in the relevant results section.

3.3. Null Hypotheses and Questions for the Novel Metrics

For these novel risk metrics, questions and null hypotheses can be formulated as Hejduk et al. did for the other statistical representations, as shown in Table 2.6. For the OPM metric, this is more clear than for the relative orbital parameters metric. For the latter, it was namely found that the angle between $\Delta\vec{i}$ and $\Delta\vec{e}$ can not be used as sole criteria to dismiss an event, and no clear safety threshold has been set yet. So, the question and null hypothesis proposed for this metric are recommended to be thoroughly reviewed if the metric is deemed useful for conjunction analysis. The null hypotheses and questions are presented in Table 3.2.

Table 3.2: Extensions of possible fundamental questions and null hypothesis for novel risk metrics.

Metric	Fundamental Question	Null Hypothesis
Outer probability Measures	Given the data do the upper and lower boundary justify a dismissal of the event?	The actual miss distance is less than the hard-body radius.
Relative orbital geometry	Given the data does the angle deviation justify a dismissal of the event?	There is a joint vanishing of the radial and cross-track separations.

4 Methodology

This chapter consists of the methodology. With the different theories used for conjunction analysis introduced, they can be tested. To test the methods, conjunctions need to be simulated. This chapter will first introduce how the simulations are performed. Furthermore, the conjunction scenarios chosen are explained, and the selection of metrics to be tested is made.

4.1. Conjunction Simulation

To study current practice in conjunction analysis and possible extensions thereof, conjunctions need to be simulated. For this, data of the states and covariances of two potentially colliding objects at some time t before TCA are needed. This time t will be set to be somewhere between the range of one day to seven days, as a screening period of seven days is often used in current practices and this period is deemed sufficient. The time t will be considered the starting point for analysing the conjunction, thus it is denoted as t_0 onward. To get the states of two potentially colliding objects, a conjunction can be modelled by initializing two objects with a similar position, and back propagating both states. Another option is to use data from the previously described CDMs. The latter option has the advantage of representing realistic conjunction cases, with reasonable values for the probability of collision and miss distance. Thus, CDMs are used as a basis for the conjunction simulation. The needed data in the CDMs are given at TCA and thus also require backward propagation. In the remainder of this section, the steps used to find the states and covariances at t_0 are described (Step 1 - Step 3). Furthermore, the steps taken to test the metrics are explained (Step 4 - Step 7).

Step 1: Back propagation of states at t_{TCA} to $t_{TCA} - \Delta t_{back}$ (t_0)

The CDMs available on Privateer Wayfinder give a wide range of information on the conjunction at hand, as mentioned before in Section 1.1.1. This information includes the start time of the screening period, and the states and covariances of the objects at TCA. The states as given in the CDM can be backpropagated from t_{TCA} to an artificial start of the screening period t_0, such that these back propagated states can be used for analysis of the new risk metrics. The settings for the back propagation have been studied in order to ensure that the conjunction parameters in the CDM can be regenerated at sufficient accuracy. The description of this study can be found in Appendix B. For the physical characteristics of the objects present in the CDM, ESA's DISCOS database is used. As a short summary of the results, Table 4.1 shows the propagation settings.

Table 4.1: Settings for backward propagation.

	Settings
Dynamical Models	Earth spherical harmonics 20D 20O, Atmospheric Drag ($C_d = 2.2$, model = US76), Sun radiation pressure ($C_r = 1.3$), Sun point mass gravity, Moon point mass gravity
Integrator	Fixed RKDP7 $\Delta t = 4$ s
Propagator	Cowell

The time Δt_{back} for which the states are backpropagated is set to vary between one and seven days, as mentioned before. As discussed in Section 1.1.1, when a conjunction is identified in reality, the conjunction is studied up until the point of TCA. The corresponding CDM is updated every day during this process. Furthermore, as TCA approaches, the uncertainty on the conjunction decreases [78]. This effect can be studied by performing the simulation for $\Delta t_{back} = 7, 6, \ldots, 1$ days. When the states and covariances are then found at t_0 and are propagated forward to t_{TCA} (discussed in Step 5), the uncertainty on the conjunction will vary due to the varying propagation time as given by Δt_{back}. Thus, the time horizon of the risk assessment can be studied by assessing how the different metrics behave as the time approaches TCA.

Step 2: Covariance estimation at t_0

The back propagation of the covariance requires further attention. A covariance matrix will grow when forward or backward propagating it from a time t. This can be explained by thinking about the problem in Monte Carlo samples. In a Monte Carlo analysis, multiple samples are initiated with a deviated position and velocity. When propagating all the samples forward from t to $t + \Delta t$, the samples will all follow a different trajectory leading to a growth of the uncertainty. If one were to propagate backward from t to $t - \Delta t$, the samples will go into the opposite velocity direction, thus also leading to a growth of the uncertainty. When propagating backward from $t + \Delta t$ to t, or propagating forward from $t - \Delta t$ to t, the samples will go back to their initial deviated states at t (with some numerical errors). In this case, the covariance matrix will thus shrink. If the covariance matrix as given in the CDM would be generated with forward propagation and if one were to have the exact same model that was used for this covariance propagation, one might be able to retrieve the initial, shrunken covariance at t_0. However, in the CDMs it is often stated that the covariance is generated by calculation and the models used to do so are not publicly available. After backward propagation of the covariance using the settings in Table 4.1, a growing trend was observed, as can be seen in Figure 4.1. The figure shows the volume of the covariance over time, computed as the product of the eigenvalues of the covariance matrix. The top figure shows the covariance volume as a result of back propagating the covariance from t_{TCA} (0 days) to t_0 (-7 days). So, the top plot needs to be read from right to left. The covariance found at t_0 as a result of back propagation was then used as initial covariance for forward propagation from t_0 (0 days) back to t_{TCA} (7 days). In the second plot, the covariance was thus forward propagated from $t = 0$ days to $t = 7$ days.

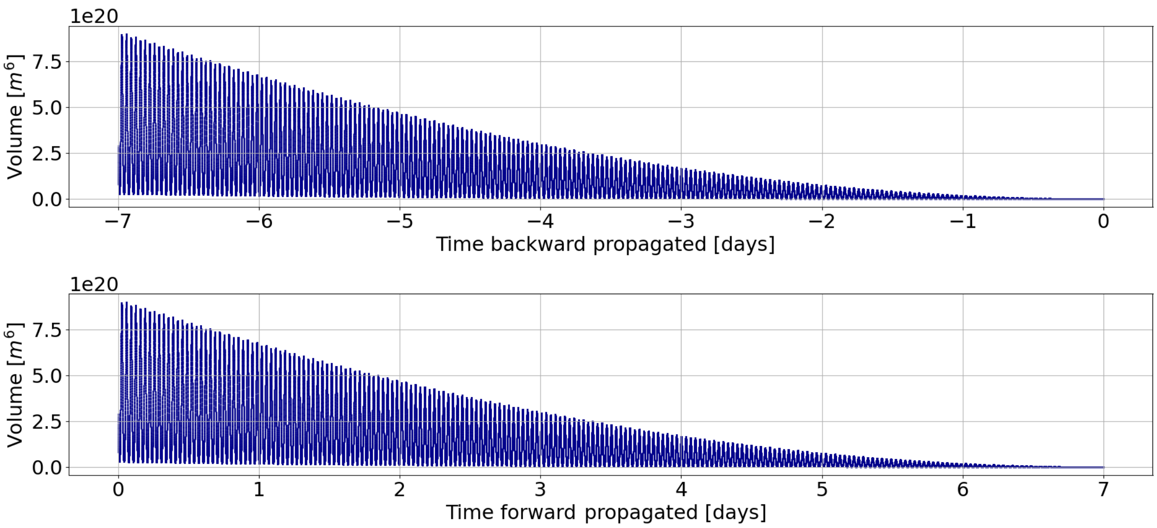

Figure 4.1: Volume of the covariance after backward and forward propagation.

From the figure it can be observed that the backward propagation leads to a larger covariance at t_0 than at t_{TCA}. In reality, the opposite is expected due to the prediction conducted from t_0. Thus, the conclusion was made that the covariance matrices from the CDM cannot be simply propagated backward, and a batch estimation algorithm needs to be used for the generation of the covariance matrices at t_0. This algorithm is described in Appendix C. In short, radar measurements are simulated and used for a batch estimation of the covariance. The algorithm will ensure that a covariance is estimated with realistic cross correlations between the different state components. This will ensure that the covariance evolves realistically when propagating it forward in time.

A last note needs to be made before moving on to the next step. Namely, a pattern can be observed in Figure 4.1. This pattern can be attributed to the fact that the covariance does not grow smoothly, but rather shrinks and grows within every orbit. The overall growing trend is still dominant. The pattern indicates that the uncertainty on the states depends on the position in the orbit. In Figure 4.2, the covariance volume over time is again shown, but now with a log scale on the y-axis. This figure clearly illustrates the difference between the initial and final covariances.

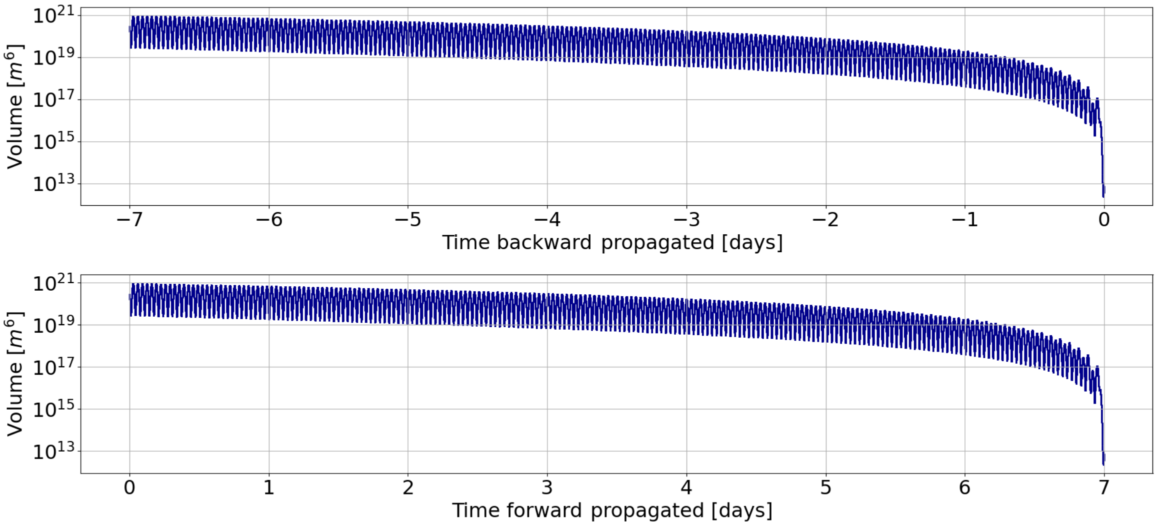

Figure 4.2: Volume of the covariance after backward and forward propagation visualized with a log scale.

Step 3: Scaling the covariance
The research is focused on analysing conjunctions including both satellites and debris fragments. The states of debris fragments are often much less certain than the states of satellites. The reason for this is that debris fragments are often much smaller and thus harder to track. Furthermore, the physical characteristics of debris pieces generally need to be measured from the Earth [48]. Moreover, space debris fragments are always non-cooperative [35]. The distinction between the two types of space objects can thus be made by scaling the covariance matrices of the objects, reflecting the differences in the uncertainty of their states. The covariance matrix of a satellite is scaled to have a positional uncertainty in the range of 1 meter, whilst the debris positional uncertainty is set to be in the range of 1000 meters. The entire covariance matrix is scaled according to the smallest positional standard deviation present in the covariance matrix as given in ECI. When a conjunction is tested for multiple Δt_{back} days of back propagation, the scaling factor is kept constant for every Δt_{back}. This is done to ensure that the effect of the propagation length is studied with a consistent initial covariance size.

Step 4: Finding time of closest approach
With the simulated data of two potentially colliding objects available at time t_0, TCA can be found. There is little documentation available on how TCA is determined during the CDM generation of Privateer. This quantity can be determined using multiple different calculations. For this research, the algorithm as found by Denenberg [22] has been used. This is a relatively fast and accurate method. The derivation of this algorithm is given in Section 2.1. The dynamical model and propagation settings used during the operation of this algorithm are the same as those used in Step 5, where the settings are explained in more detail.

Step 5: Finding states, covariances and miss distance at t_{TCA}
When the time of closest approach is retrieved, the states and covariances at TCA can be found by propagating the states and covariances at t_0 to t_{TCA}. The analysis of the settings for the forward propagation can again be found in Appendix B, where the method used for the covariance propagation is also studied in more detail. The settings for the forward propagation have been studied in addition to the settings for the backward propagation, as the objectives of the forward and backward propagations are different. For the backward propagation, the states need to be relatively close to truth for the realization of a realistic conjunction scenario. In addition, backward propagation must be performed only once for each time Δt_{back}. The propagation settings for forward propagation were

designed to be more flexible for adjustments, as forward propagation will be performed more frequently. This includes cases with mismodelled dynamical models to assess their impact on conjunction analysis, as explained later in this chapter. Thus, it was important to find a balance between computational efficiency, and model accuracy for the forward propagation. The final propagation settings have been defined as shown in Table 4.2. The covariance has been propagated linearly.

Table 4.2: Settings for forward propagation.

	Settings
Dynamical Models	Earth spherical harmonics 20D 20O, Atmospheric Drag ($C_d = 2.2$, model = US76), Sun radiation pressure ($C_r = 1.3$), Sun point mass gravity, Moon point mass gravity
Integrator	Variable RKDP87, tolerance $= 10^{-13}$
Propagator	Cowell

Step 6: Covariance remediation
Due to numerical issues, it can occur that the propagated covariance matrices are not positive definite. The covariance matrices need to be positive definite for the calculation of the probability of collision [38]. In the NASA CARA Software Development Kit an algorithm developed by Hall et al. [40], called the Eigenvalue Clipping Method, has been implemented to remediate the covariance if needed. The method uses eigenvalue decomposition, and uses a threshold to determine whether the eigenvalues of the matrix are sufficiently large. If this is not the case, the covariance matrix is remediated accordingly [40]. During the conjunction simulation, this algorithm is employed to remediate the covariance as found at t_{TCA}, if needed. The formulas used are given below [38]. The covariance matrices of the primary and secondary object are summed in ECI and rotated to the RTN frame resulting in $\mathbf{P}_{RTN}$. Then, with $\boldsymbol{\lambda}_{init}$ a diagonal matrix with the initial eigenvalues of $\mathbf{P}_{RTN}$ and $\mathbf{V}$ a column matrix with the eigenvectors of $\mathbf{P}_{RTN}$, the matrix can be written as:

$$\mathbf{P}_{RTN} = \mathbf{V}\boldsymbol{\lambda}_{init}\mathbf{V}^T. \tag{4.1}$$

If any of the individual eigenvalues are less than a certain threshold λ_{clip}, the value is replaced by this threshold:

$$\lambda_{init_i} = \begin{cases} \lambda_{init_i} & \text{if } \lambda_{init_i} > \lambda_{clip}, \\ \lambda_{clip} & \text{if } \lambda_{init_i} < \lambda_{clip}. \end{cases} \tag{4.2}$$

The threshold has been recommended to be set equal to 10^{-4}HBR [38]. With the clipped eigenvalue matrix $\boldsymbol{\lambda}_{clipped}$, the remediated covariance can be established:

$$\mathbf{P}_{rem} = \mathbf{V}\boldsymbol{\lambda}_{clipped}\mathbf{V}^T. \tag{4.3}$$

Step 7: Assess the collision risk at t_{TCA}
For the calculation of P_c it is stated on Privateer Wayfinder that NASA CARA's SDK is used [66]. There are multiple different methods implemented in the SDK, as introduced in Section 2.2. To summarize, the 3D formulation as found by Hall [37], the 2D formulation as derived by Elrod [24], the 2D formulation as found by Foster and Estes [32], the maximum P_c calculation and a Monte Carlo analysis are implemented. In every CDM it is stated which formulation was used for the calculation of P_c. These formulations can thus be tested on the simulated conjunction. Apart from the vanilla P_c calculations, other risk metrics can be tested and assessed as well.

Remarks
It must be noted that as the states found in the CDM are back propagated and the covariances are synthesized, the states and covariances found at t_0 will have an offset compared to the data that was initially used for the generation of the CDM. The states have been backward and forward propagated with a numerical error of 10^{-1} m (shown in Appendix B). Furthermore, there will also be an offset due to the dynamical model used for the generation of the CDM and the dynamical model used in this research (discussed in Appendix B). Moreover, the generation of the

covariance matrices will also cause a deviation from the original data used by Privateer Wayfinder. Nevertheless, the CDM is merely used for the production of a realistic conjunction scenario. The deviations of the states and covariances will thus not be of great concern given that the test cases can be generated at known and repeatable high precision.

4.2. Test Cases

Since CDMs are used, relevant conjunction test cases can be selected. All the different test cases selected are flying in LEO, as the density of space objects is largest in LEO [30]. Chosen conjunctions should either occur frequently, challenge current conjunction analysis practices or show potential for the use of new risk assessment metrics. The conjunction data or dynamical model settings of a test case can be altered for further testing of the methods. Possible data changes are:

- One of the limitations described in Section 1.1.3 is that there are many error sources present in current conjunction analysis practices. In general, the dynamical model used for the propagation of the state and covariance will not be a perfect representation of reality. The model fidelity can be limited, due to the omission of perturbing forces for example. Furthermore, inaccuracies in the estimation of dynamical parameters such as the drag coefficient or radiation pressure coefficient, can further reduce accuracy. It is important to note the effect of mismodelling, and thus test cases can be run with different dynamical models or different settings for the environmental parameters, such as C_d. When running a simulation with a deviated C_d for only one of the two objects, a misestimation of the ballistic coefficient is simulated. By tweaking C_d for both objects, a mismodelled atmospheric density is simulated. The latter option is chosen, only Step 5 (forward propagation) is run with a mismodelled drag coefficient for both objects.
- To test how the effect of mismodelling can be mitigated, process noise can be introduced to the propagation of the covariance. Process noise can account for uncertainties in the dynamical model, by increasing the uncertainty in the states. The noise factor thus depends on the uncertainties introduced by the mismodelled accelerations. For a covariance matrix defined in the ECI frame, the process noise factor is given by $\mathbf{R}^{(ECI/RTN)}\mathbf{\Gamma}\mathbf{Q}\mathbf{\Gamma}^T\mathbf{R}^{(ECI/RTN)^T}$, with $\mathbf{R}^{(ECI/RTN)}$ the rotation matrix to rotate the process noise from RTN to ECI, and $\mathbf{Q}$ and $\mathbf{\Gamma}$ defined as [33]:

$$\mathbf{Q} = \begin{bmatrix} \sigma_{\ddot{R}}^2 & 0 & 0 \\ 0 & \sigma_{\ddot{T}}^2 & 0 \\ 0 & 0 & \sigma_{\ddot{N}}^2 \end{bmatrix}, \ \mathbf{\Gamma} = \begin{bmatrix} \frac{\Delta t^2}{2} & 0 & 0 \\ 0 & \frac{\Delta t^2}{2} & 0 \\ 0 & 0 & \frac{\Delta t^2}{2} \\ \Delta t & 0 & 0 \\ 0 & \Delta t & 0 \\ 0 & 0 & \Delta t \end{bmatrix} \tag{4.4}$$

  The derivation for the rotation matrix $\mathbf{R}^{(ECI/RTN)}$ can be found in Appendix D. The standard deviations $\sigma_{\ddot{R}}$, $\sigma_{\ddot{T}}$ and $\sigma_{\ddot{N}}$ are the uncertainties in the acceleration due to the dynamical model. How these values are determined, will be discussed in the relevant section of the results in Chapter 5.
- Another limitation found was that the covariances used are not a good representation of reality and that the P_c calculation suffers from the dilution effect. This effect is studied both by scaling the covariance matrices to represent either satellites or debris fragments (Step 3), and by propagating them for different lengths of time Δt_{back} (Step 1).
- As the CDM is merely used for the simulation of a realistic conjunction scenario, the values in the CDM are flexible for adjustments as well. The miss distance can be changed to simulate a collision, near miss or large miss.

The selected CDMs consist of a frequently occurring Starlink on Starlink conjunction, and a conjunction involving the formation-flying satellites TerraSAR-X and TanDEM-X.

Case 1: Starlink on Starlink conjunction

The first test case consists of a Starlink on Starlink conjunction. Starlink is a satellite constellation of SpaceX. The satellites are used to provide internet [55]. There are many Starlink satellites currently in orbit and SpaceX is planning to launch a satellite mega-constellation consisting of approximately 12,000 satellites operating in LEO in the near future [55]. The velocities of the satellites are relatively high, so when a possible conjunction between these satellites occurs it will obey the high-relative velocity assumption. In general, most conjunctions have a high-relative velocity [18], and thus this test case lends itself well to study the performance of current conjunction analysis practices. It can be noted that the satellites are maintained by the same O/O, and thus in reality it is very unlikely that a Starlink on Starlink collision will occur. Namely, often operators have state estimates with a smaller uncertainty and are thus more certain of the probability to collide. Furthermore, in case a collision is likely to occur, no communication on who should maneuver is needed, which avoids complications in the mitigation process. Although it is unlikely that the satellites collide, the test case will still be valuable due to aforementioned reasons. Furthermore, an anomaly or control error can occur, potentially resulting in the satellites becoming debris objects. Moreover, Starlink on Starlink conjunctions are highly prevalent on Privateer Wayfinder.

The conjunction at hand was found on Privateer Wayfinder on August 14, 2024 [66]. The conjunction involves Starlink-3254 and Starlink-4000 and the conjunction is depicted in Figure 4.3. The test case will be adjusted to test the effect of changing the miss distance, mismodelling the dynamical model, and studying the effect of scaling the covariance. All different simulations conducted using this conjunction can be seen in Table I.1 in Appendix I.

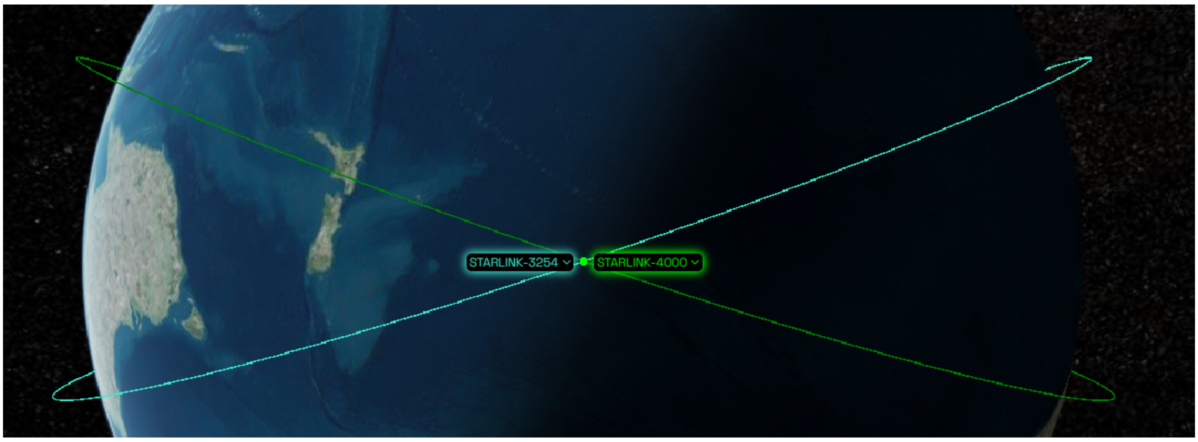

Figure 4.3: Starlink-3245 on Starlink-4000 conjunction, retrieved from Reference [66].

Case 2: Terra Sar X & Tandem X

Another interesting test case is a conjunction between TerraSAR-X and TanDEM-X. TerraSAR-X and TanDEM-X are two controlled formation-flying satellites operating as a radar interferometer [19]. As the satellites are flying in formation, they will often be in close proximity with each other. These objects have been used in former research to evaluate the performance of the use of the geometric relationship between the relative eccentricity and inclination vectors for formation control, as described in Chapter 3. As the metric is suitable for this application, it may also serve to analyse conjunctions in low-relative velocity scenarios. Furthermore, the stability of the metric shown in the study conducted by D'Amico et al., in which the formation was passively safe for 20 days [19], indicates it may prove useful to extend the time horizon for conjunction analysis. Using conjunctions between TSX and TDX can help establish whether this is the case. As the satellites are flying with a low-relative velocity, the test case is also more challenging for current practice in conjunction analysis, as it violates Assumption 2 (Subsection 1.1.2) for the 2D P_c calculation.

Sixteen CDMs were found on September 10, 2024. All conjunctions occur within a time span of ten hours. As can be seen in Figure 4.4, the satellites are continuously passing around each other.

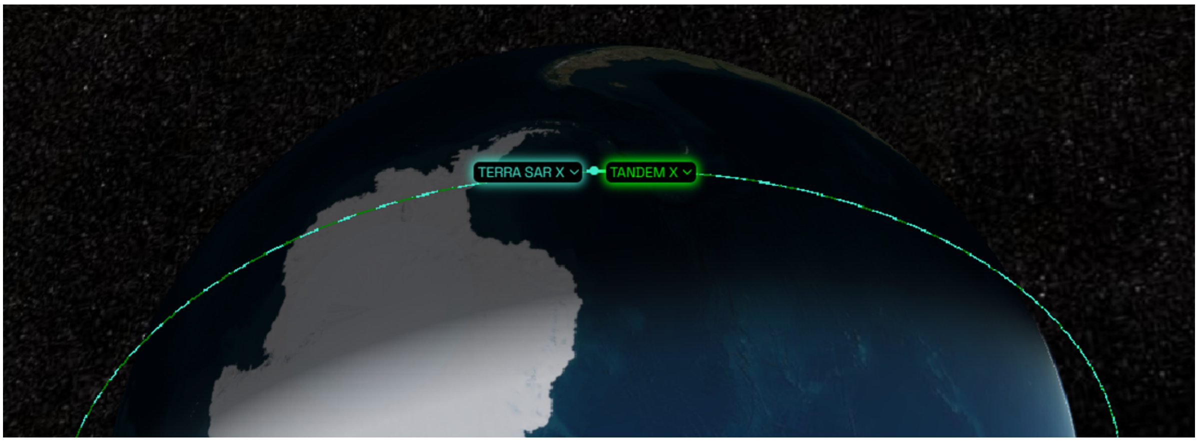

Figure 4.4: TerraSAR-X on TanDEM-X conjunctions, retrieved from Reference [66].

4.3. Exploration of Potential Improvements

Various methods and metrics could be evaluated to potentially improve conjunction analysis. Examples of enhancements that could be made to improve conjunction analysis are taking into account attitude information, providing alternatives metrics for risk quantification, or providing a more timely, stable, or reliable solution for conjunction analysis. Every improvement comes with its own advantages and disadvantages. In this section, multiple metrics are introduced and the ones that will actually be implemented are chosen. The possible extensions are:

- Alternative statistical representations of the collision risk, such as the possibility and plausibility could be used. Within these representations, there are multiple different metrics available to quantify the risk. A detailed description of these methods can be found in Chapter 2.3.
- Different distance metrics including the uncertainty or representing the distance using other coordinate frames could lead to a more reliable miss distance.
- Relative orbital parameters could provide a more stable representation of the encounter over time. Often a CDM is updated 3 times a day. When Cartesian coordinates are used for the representation of the encounter, the solution will be highly variable. This is due to the fact that a change in any of the RTN directions will yield a change in x, y, z simultaneously. Using relative orbital parameters such as the relative e/i vector separation (explained in Chapter 2.3) could lead to a more stable solution when updating the conjunction data every day until TCA.
- Taking into account attitude information when determining the probability of collision may result in a more reliable analysis. One disadvantage of the current probability of collision is that it is often calculated with assumed spherical shapes. Using rotational dynamics to describe the attitude of the objects would be a good improvement. Attitude information could also be used to get a better estimate of the HBR [54].
- Extending the time horizon available for decision making could enhance conjunction analysis. It would be better to determine whether a collision avoidance maneuver needs to be made further in advance of TCA. It has been tested before if machine learning can be used to predict the probability of collision ahead of time. If this could be done reliably, this could improve conjunction analysis [78].

In addition to these possible extensions, there are also extensions available to improve the observational data [47] [20] or to improve the filters [68] used for conjunction analysis. Such solutions are out of the scope of this research, as they are not part of the analysing step of CA.

Table 4.3 gives a summary of the expected benefits, expected drawbacks and current status for the different metrics and methods. It must be noted that, most drawbacks are related to the nature of the specific metric/method, however for the HBR/attitude and machine learning methods, (additional) thesis related drawbacks are given, indicated by a star $(^*)$.

Table 4.3: Possible methods/metrics that could be used to expand conjunction analysis.

Metric/ method	Expected benefit	Expected drawback	Status
Maximum P_c [42]	Account for unrealistic covariance, mitigate dilution effect	Increase false alarms	Operational and implemented by NASA CARA [63]
WSRT [42]	Mitigate dilution effect	Historical data needed	Operational experience [42]
Scaled P_c [42]	Account for unrealistic covariance, mitigate dilution effect	Increase false alarms, experience needed	Operational experience [48]
Outer probability Measures [21]	Distinguish between random from systematic uncertainty, mitigate dilution effect	Increase false alarms	Very recent research [21]
Distance metrics [80]	Provide alternative MD and include uncertainty	Metric specific for CA not yet derived	Use for spaceflight proposed [80]
Relative orbital parameters [19]	Provide more stable solutions over time	Challenge in interpretation	Used for formation control[19]
P_c uncertainty [42]	Account for unrealistic covariance, mitigate dilution effect	Increase false alarms, historical data needed	Research and testing phase [42]
Overlapping ellipses [42]	Mitigate dilution effect	Increase false alarms	Tested on historical conjunctions [42]
HBR/attitude [54]	Improve HBR or add attitude information	Attitude data needed, Missing knowledge spacecraft dynamics*	Active area of research [54]
Machine learning [78]	Improve timeliness of CDM information	Missing knowledge ML algorithms*	Tested during ESA challenge [78]

For the selection of methods or risk metrics to implement, the aspects given in Table 4.3 are all taken into account. First of all, the three top metrics, are already operational. The advantage of this is that these metrics can thus already be used without needing much time to implement them. The Wald Sequential Ratio Test is a part of the probability representations. The limitation of the metric is that a multitude of historical data is needed, which is often hard to obtain [42]. So this metric cannot be used easily. The scaled P_c metric and the maximum P_c are alike, but the representation of both is different. The scaled P_c metric uses two scale factors and experience is needed to determine the minimum and maximum covariance, whilst the maximum P_c value provides the maximum probability of collision based on one scale factor, found by iteration. The latter is implemented by NASA CARA. So this metric is easy and quick to use. The metric will thus be used to assess some test cases and to study the effect of the covariance size. The lower four risk assessment metrics shown in the table all have their drawbacks. The P_c uncertainty metric, which is a part of the plausibility representations [42], again needs historical data. Furthermore, the metric is, although not the same, alike the maximum P_c metric and the scaled P_c metric. To study the attitude information, in depth knowledge of rotational dynamics and spacecraft attitude is needed, which would be challenging to gain in the time available for the research. The same holds for the use of machine learning to predict P_c ahead of time. Also, the overlapping ellipses metric, which is part of the possibility representation [42], will lead to a high amount of false positives.

The outer probability measures metric, distance metric, and relative orbital parameters metric all show great potential to contribute to current conjunction analysis. The relative orbital parameters metric can provide more stable solutions which may lead to an extended time horizon for decision making. As this is one of the research goals, this metric will be implemented. Furthermore, the OPM metric provides potential to reliably mitigate the dilution effect and to not only determine whether a conjunction is safe or not, but also determine whether additional tracking data is needed. This metric will thus also be implemented. While not discussed thoroughly in Chapter 3, distance metrics based on orbital elements used to correlate measurement tracklets [80] may be adaptable to conjunction assessment. Details of the method are provided in Appendix G for completeness, but the method is not pursued further due to expected complications and time considerations.

4.4. Survey on Data Usage for Conjunction Analysis

As new risk metrics are introduced, the question arises as to how the results of the different metrics can be presented to satellite operators. To this extent, the third research question was posed, as defined in Section 1.2 and repeated here:

"How can the new methods be synthesized to produce useful output for operators?".

Satellite operators can be considered the end-users of the information generated during conjunction analysis. Operators namely have the responsibility of determining whether a collision avoidance maneuver should be performed to avoid potential collision risks. As described in Section 1.1, the standardized CDM data format is often used to inform operators of critical conjunctions. Operators can then use the information provided in the CDMs to determine whether a certain mitigation action needs to be taken. These actions range from performing a collision avoidance maneuver to gathering or requesting additional tracking data. As discussed before, the CDM includes information such as the probability of collision and state information. To understand whether it would be useful to expand CDMs with other risk assessment metrics and if so, how this should be done, it is important to understand their current usage. Specifically, it is essential to understand whether and how operators use the current CDMs for their decision to mitigate a risk, or for conjunction analysis in general. Furthermore, the limitations of CDMs can be investigated, together with the identification of any additional information that might be of interest to operators. Although the inclusion of P_c in CDMs is not obligatory according to the CDM standard of the Consultative Committee for Space Data Systems (CCSDS), often P_c is included in CDMs. In the CDMs published by Privateer, the P_c metric as derived by both Hall [37] and Elrod [24] is presented. Both formulations provide the probability of collision, and thus both $P_{c_{Elrod}}$ and $P_{c_{Hall}}$ answer the same question as posed by Hejduk et al. (Table 2.6) [42]. However, when introducing other risk metrics, such as OPMs, for conjunction analysis, a different question is answered (Table 3.2). When this is not apparent to operators, this could lead to potential problems when they need to interpret the data presented to them. Furthermore, every metric has its own level of conservatism. Depending on the operator, one might be more inclined to use a certain metric than the other. The conservative nature of a certain metric is inherent to the metric, thus operators should either be aware of this when interpreting the data, or this should be indicated to them.

A survey has been created to explore operators' perspectives on the current application of CDMs and their possible future extensions. The survey aims to obtain information on the following aspects:

- Do operators currently use CDMs, and if so, what aspects presented in the CDMs do they consider leading in a decision to mitigate a risk?
- Would operators be open to the use of additional risk assessment metrics and how would they want these metrics to be presented to them?
- In general, when using multiple risk metrics, how should the data be structured?

The results of the survey provide insights into the challenges and opportunities of using new risk metrics for conjunction analysis and the incorporation thereof in CDMs. This part of the research aims to bridge the gap between the theoretical analysis of novel metrics and their associated operational applicability, to hopefully best serve the actual need of satellite operators.

Kerr et al. have also conducted a survey that focuses on current and best practice in conjunction analysis, methods, and communication [48]. The survey had three different respondent groups, including satellite operators, SSA tool developers, and SSA providers. As the final research questions of this thesis is focused on the end-users of conjunction data, the main goal is to reach satellite operators to answer the research question. Valuable insights can already be taken from the survey conducted by Kerr et al. The most important ones are:

- The probability of collision as formulated by Alfriend and Akella is often used as risk assessment metric. Furthermore, the maximum P_c construct and the scaled P_c method are also used in practice.
- If the probability of collision is not utilized for the decision to mitigate a collision risk, it is due to the often unrealistic covariance. Instead, operators then choose to use the miss distance as measure.
- Among the different possible extensions that could be made to enhance conjunction analysis, geometry was mentioned. Other extensions named were the generation of metrics that can be used for low-velocity conjunctions and machine learning algorithms.
- Operators wish to perform their own collision avoidance maneuver analysis.

- In general, operators are content with the standard format of data; they only have suggestions for a different distribution of the data.
- The general aspects of conjunction analysis that could be improved are data quality and timeliness.

In addition to these insights, which can be directly utilized to address the research question, the survey is used as a reference to identify the general information needed from participants to be able to interpret the results correctly. That is, information such as the regime the participants are operating in, for example. As mentioned above, the survey conducted for this research targets satellite operators as the response group. The aim is to find participants from a range of organizations operating on various numbers of satellites. The survey has been conducted online using Survalyzer [72]. The responses to the survey remain completely anonymous. The participants of the survey have been drawn from the academic network. The entire survey can be found in Appendix H.

5 Results

This chapter consists of the results. The current practices used in conjunction analysis have been tested on the original CDMs found on Privateer Wayfinder. Furthermore, the conjunctions have been simulated to test the different risk assessments. Last, the results of the survey are shown.

5.1. Verification of Denenberg's Algorithm

The Denenberg algorithm has been utilized to determine TCA, as outlined in Step 4 in Section 4.1. In this section, its performance is evaluated. The algorithm was tested using the CDM from the Starlink on Starlink conjunction and one of the CDMs from the TSX on TDX conjunction (CDM identifiers can be found in Appendix J). For the former case, the states provided in the CDM have been backpropagated from t_{TCA} to $t_0 = t_{TCA} - 7$ days, as outlined in Step 1 in the methodology. Using the states at t_0, TCA was found using the Denenberg algorithm [22] as described in Chapter 2.1. The interval within which the algorithm had to find TCA was set to range from t_0 to the end of the screening period, as documented in the CDM. The results of the regenerated TCA and its associated MD can be compared to TCA and MD as provided in the CDM. The results are presented in Table 5.1.

Table 5.1: TCA and MD as found using the Denenberg algorithm for the Starlink on Starlink conjunction.

	TCA	MD
Original CDM	2024-08-16 02:58:54	98.81 m
Regenerated CDM	2024-08-16 02:58:54	98.81 m
Difference	56 µs	0.34 mm

The results are in line with the expectation. For the TSX/TDX case, sixteen CDMs have been found on Privateer in one day. All CDMs share the same screening periods. The first CDM was taken, and the states have been backpropagated for one day. The Denenberg algorithm was again used to identify the various close approaches. For the Starlink on Starlink conjunction, the algorithm was set to report the global minimum only. In this case however, all local minima had to be identified, as at least sixteen close approaches were documented during the screening period. There may be additional close approaches within this period that were not published on Privateer Wayfinder. Figure 5.1 shows the miss distance over the course of propagation. In green, the TCAs as provided in the CDMs are displayed. Furthermore, the dashed red lines represent the local extremes found by the algorithm.

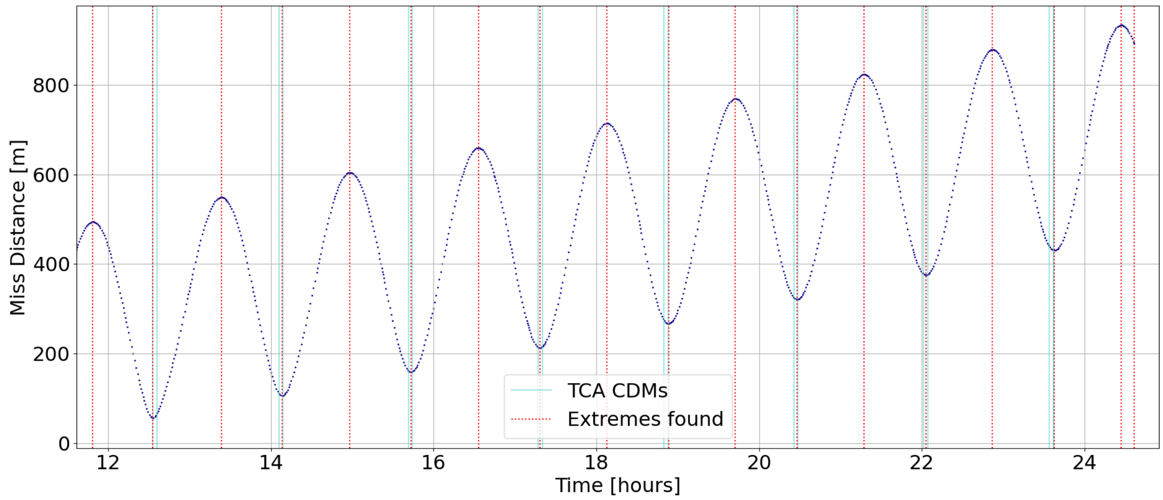

Figure 5.1: Miss distance over time for the TSX/TDX conjunction.

Figure 5.1 shows that the algorithm has correctly identified all local extreme points. Note, the maximum miss distances have also been located. This is because the algorithm finds all extremes under a specified critical distance of 1000 meters, unless the search is specifically limited to find only the global minimum. Furthermore, it can be noted that for every local minimum, two CDMs appear to be published. The local minimum found by the algorithm seems to either match one of the TCAs from the two CDMs or occur between the two TCAs. The reason for this has not been established. More information is not available on how Privateer generates its CDMs. However, it can be concluded that the algorithm developed by Denenberg is sufficient to find either one close approach or multiple close approaches.

5.2. Comparison of P_c Formulations

The current risk assessments present in NASA CARA's SDK have been tested using the original CDMs. This has been done for both the Starlink conjunction as well as the TSX/TDX conjunction. The former conjunction has a high-relative velocity and is thus expected to receive similar results for the different metrics. The latter conjunction has a low-relative velocity and is thus expected to receive varying results. For the TSX/TDX case, the first CDM has been used. The results are shown in Table 5.2.

Table 5.2: P_c from the CDMs and calculated using SDK for the Starlink and the TSX/TDX conjunction.

Metric	Starlink CDM	Starlink SDK	TSX/TDX CDM	TSX/TDX SDK
$P_{c_{Foster}}$		$1.21 \cdot 10^{-2}$		$2.77 \cdot 10^{-3}$
$P_{c_{Elrod}}$	$3.61 \cdot 10^{-3}$	$1.21 \cdot 10^{-2}$	$1.36 \cdot 10^{-3}$	$2.77 \cdot 10^{-3}$
$P_{c_{Hall}}$	$3.61 \cdot 10^{-3}$	$1.21 \cdot 10^{-2}$	$3.34 \cdot 10^{-3}$	$6.77 \cdot 10^{-3}$
$P_{c_{max}}$		$2.03 \cdot 10^{-2}$		$5.47 \cdot 10^{-3}$
$P_{c_{MC}}$		$1.16 \cdot 10^{-2}$		$6.33 \cdot 10^{-3}$

The first thing that can be noticed is that the probabilities found by SDK are not equal to the probabilities as reported in the CDMs for both conjunctions. This may be caused by the HBR that has been used for the calculation. The HBR used in this research has been found by summing the average cross sections of the objects as reported in the DISCOS database. Although this is not the most conservative method for determining the HBR (using the maximal cross section would be), this method was chosen to ensure that the HBR is not unnecessarily large. Since many of the metrics tested are conservative in nature, the average was deemed sufficient. The HBR used by Privateer is unknown. Again, this is not a worrisome fact, as the CDMs used for this research are merely there to simulate realistic conjunction cases. Thus, as long as the HBR settings are consistent and repeatable, this deviation is accepted. The second thing that can be noticed is that $P_{c_{Foster}}$, $P_{c_{Elrod}}$, $P_{c_{Hall}}$ and $P_{c_{MC}}$ are all similar for the Starlink case. This is as expected, due to the fact that the conjunction adheres to the high-relative velocity requirement. The maximum P_c is larger, due to the conservative nature of the metric. For the TSX/TDX conjunction, $P_{c_{Foster}}$ and $P_{c_{Elrod}}$ are similar, which is also expected due to the similarity of the formulations. All metrics are in the same order, however $P_{c_{Foster}}$ and $P_{c_{Elrod}}$ are not completely the same as $P_{c_{MC}}$ and $P_{c_{Hall}}$. The Monte Carlo metric can be considered to be most accurate, as this metric requires the least amount of assumptions. It will thus be closest to reality. The maximum P_c is again larger than $P_{c_{Elrod}}$ and $P_{c_{Foster}}$, but lower than $P_{c_{MC}}$ and $P_{c_{Hall}}$, which can be explained by the fact that the underlying model used for $P_{c_{max}}$ is the 2D approach of calculating P_c. For low-relative velocity encounters, $P_{c_{Hall}}$ (or actually N_c, but denoted as $P_{c_{Hall}}$ onward) represents an upper boundary for the probability of collision. As can be seen, $P_{c_{Hall}}$ was found to be a bit higher than $P_{c_{MC}}$, as is thus expected. From this it can be concluded that for a low-relative velocity approach, the 2D risk assessments will not provide accurate results as the approach violates Assumption 2. For a typical close approach with a high-relative velocity, such as the Starlink conjunction, the 2D risk assessments can be used.

5.3. Analysis of Existing Risk Metrics

In this section, simulated conjunctions are used to evaluate the performance and behavior of different risk assessment metrics. Specifically, the 2D risk assessments have been tested on the simulated Starlink on Starlink conjunction. The 2D approach of calculating P_c is chosen, as this is often used in practice. The formulation of P_c as derived by Elrod has been used, as this one is also used by Privateer [66]. It can be noted that the results for $P_{c_{Elrod}}$ will closely resemble the results of $P_{c_{Foster}}$ as was shown in Subsection 5.2. In addition to $P_{c_{Elrod}}$, $P_{c_{max}}$ was chosen to evaluate to test its effectiveness in mitigating the dilution effect for diluted probabilities. The CDM data and dynamical model have been tweaked as shown in Table I.1 to create 18 test cases. In summary, the different test cases consist of a simulated collision, a simulated near miss, and a simulated large miss, with covariances scaled to represent satellites and debris fragments, as explained in the methodology. Furthermore, every test case has also been simulated with a mismodelled dynamical model. Specifically, the drag coefficient has been tweaked for both objects, to simulate a mismodelled atmospheric density. For each of these test cases, the metrics were evaluated, and the results are presented in the figures shown later in this section. The x-axis in the figures represents the time for which the states have been backpropagated. Then, on the y-axis, the probability of collision is shown, which was calculated using the states and covariances obtained after backward and forward propagation of Δt_{back} days. It must be noted that the figures have been limited to show no P_c values below 10^{-8}, such that the critical decision region $P_c \in [10^{-5}, 10^{-3}]$ can be studied in more detail.

During the analysis presented in this section, the term risky and unacceptable will be used. In this analysis, a conjunction is identified as risky or unacceptable if $P_c \geq 10^{-4}$. This is in line with the safety threshold that is often used in operation [29]. Consequently, the risk is called safe or acceptable when $P_c < 10^{-4}$. This qualification of the risk is then evaluated by analysing the number of false positives and false negatives that occur. To do this, it is necessary to define the conditions under which each type of error occurs. For a satellite on satellite conjunction, the state estimates are determined with a relatively high degree of certainty. Thus, an operator is set to mitigate the collision risk when the miss distance is less than the HBR, and thus a collision is assumed to occur. For a debris fragment, the certainty on the states is much worse. The question arises as to what extent an operator is willing to allow a debris fragment of considerable size to fly by their satellite. For a conjunction including a debris fragment, an operator is set to take a mitigation action if the miss distance is lower than 50 m (assuming HBR < 50 m). If the various risk metrics indicate that a conjunction is safe, but according to the conditions above an operator should take action, a false negative is flagged. Conversely, if a metric indicates an unacceptable risk when the true conditions require no mitigation, this is labeled a false positive. A summary of these conditions is presented in Table 5.3. Here τ defines the safety threshold, equal to the HBR for conjunctions with satellites only, and 50 m for conjunctions involving a debris fragment.

Table 5.3: Conditions for the occurrence of the different possible outcomes.

	$P_c \geq 10^{-4}$	$P_c < 10^{-4}$
MD $\leq \tau$	True positive	False negative
MD $> \tau$	False positive	True negative

5.3.1. Collision: Satellite x Satellite

Figure 5.2 shows the results for a simulated satellite on satellite collision.

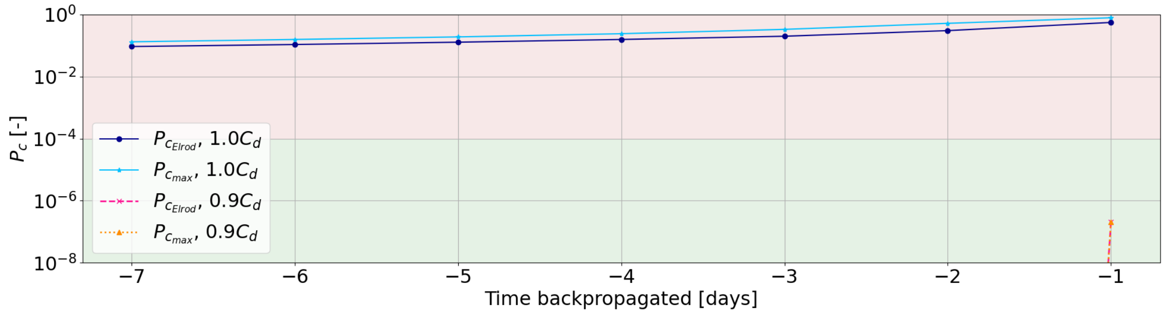

Figure 5.2: P_c for a satellite on satellite collision as a function Δt_{back}, without process noise.

Multiple observations can be made from this figure.

- The simulation without mismodelling results in large probabilities using the Elrod P_c metric for all Δt_{back}. The probability is above the safety threshold of 10^{-4} for every instance of backward and forward propagation. As the conjunction was defined to result in a collision and all instances result in the identification of a risky situation, there are zero false positives or false negatives. All correctly modelled results are true positives.
- The maximum P_c metric shows very similar results, which is expected, as the covariances of satellites are set to be small. Thus, these will not lead to a diluted probability. Again, all results are true positives.
- Mismodelling of C_d for both objects, and thus mismodelling of the atmospheric density, leads to a very low probability for both $P_{c_{max}}$ and $P_{c_{Elrod}}$ for all Δt_{back}. Due to the limits set on the figure, the probabilities for $\Delta t_{back} \leq -2$ are not visible. It has been established however that the probabilities for these cases are following a decreasing trend as Δt_{back} gets smaller (note, the absolute propagation time $||\Delta t_{back}||$ thus gets bigger). This is as expected. Namely the Starlink satellites are operating in LEO. Atmospheric drag thus has a large effect on the trajectories of both satellites. When performing the backward propagation with the initially chosen C_d, but forward propagating with a mismodelled one (equal to $0.9C_d$), the satellites will drift from their formerly backpropagated trajectories. The time of closest approach was set to match the time found for the correctly modelled case. This simplification has been deemed acceptable, as the objective is to examine the general impact of mismodelling, specifically in terms of obtaining a different miss distance at TCA compared to reality. Due to the drift of the objects, the miss distance found at TCA will be larger than the miss distance defined at the start of the simulation, leading to a low probability of collision. The longer the states are propagated for, the further away the satellites will drift. Thus, when backward propagation is only conducted for one day, the satellites have drifted less far from their original trajectories, leading to a higher P_c ($\approx 10^{-5}$). However, all values are still below the risk threshold, leading to seven false negatives. Hypothetically, if the mismodelled drag parameter would have been closer to the initial selected coefficient, the states would have drifted less far away from the correct trajectories. At some backpropagated time Δt_{back}, close to t_{TCA}, the probability would have been above the critical threshold. In this case, the time horizon in which it would have become apparent that a collision is going to occur, would be very short. So the accuracy of the dynamical model will also have an influence on the time horizon available for operators to take action.
- The maximum P_c metric does not raise the low P_c values to the risky region in the mismodelled case, as the issue lies not with the covariance but with the drifted states. The covariance size is small, so the dilution effect is not observed. The maximum P_c calculation also leads to seven false negatives for the mismodelled atmospheric density.

For the simulated satellite on satellite collision, it has been observed that a mismodelled drag coefficient leads to an underestimation of the collision risk. Introducing process noise to the covariance propagation could solve this problem. To incorporate this noise, the matrix $\mathbf{Q}$ (Equation 4.4) must be defined. This is achieved by quantifying the difference in acceleration caused by drag for a single satellite. This difference is presented in the ECI frame in Figures 5.3a and 5.3b.

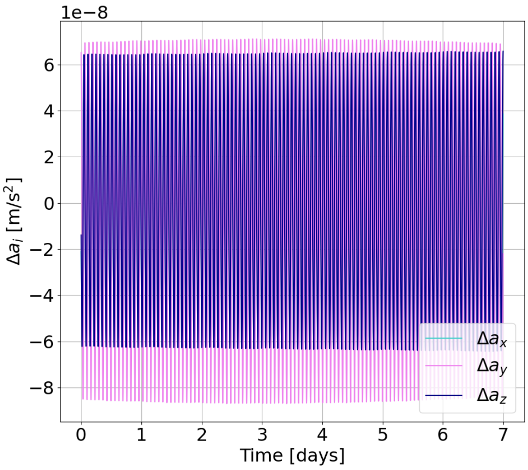

(a) Deviation in acceleration due to drag.

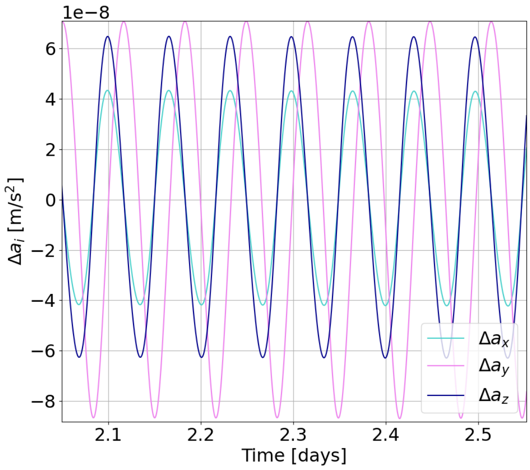

(b) Deviation in acceleration due to drag, zoomed in.

Figure 5.3: Deviation in acceleration due to drag as a function of time in the ECI frame.

As can be seen, the variation is significant in all three directions. However, for drag acceleration, the greatest effect is expected to occur in the along-track direction, since drag by definition acts in the anti-velocity direction. The uncertainties in the RTN frame will be more stable. The accelerations are thus rotated from ECI to RTN, for which the result can be observed in Figure 5.4.

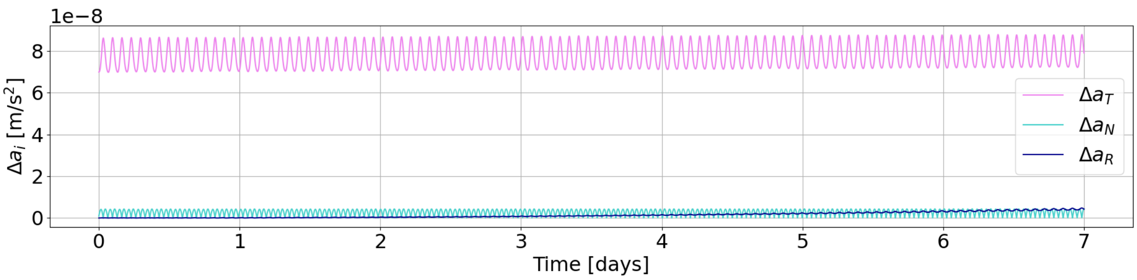

Figure 5.4: Deviation in acceleration due to drag as a function of time in the RTN frame.

Indeed, the uncertainties introduced by a mismodelled drag coefficient are more stable in the RTN frame. So, this frame is used to define $\mathbf{Q}$. The individual standard deviations have been found by identifying the maximum acceleration error in each direction, leading to $\mathbf{Q}$:

$$\mathbf{Q} = \begin{bmatrix} 4.8 \cdot 10^{-9}\ \mathrm{ms}^{-2} & 0\ \mathrm{ms}^{-2} & 0\ \mathrm{ms}^{-2} \\ 0\ \mathrm{ms}^{-2} & 7.0 \cdot 10^{-8}\ \mathrm{ms}^{-2} & 0\ \mathrm{ms}^{-2} \\ 0\ \mathrm{ms}^{-2} & 0\ \mathrm{ms}^{-2} & 4.4 \cdot 10^{-9}\ \mathrm{ms}^{-2} \end{bmatrix}. \tag{5.1}$$

The noise term is added iteratively during the covariance propagation, such that the effect of noise can accumulate over time. This is necessary as the effect of mismodelling also grows over time. The iterative steps taken are set to 60 seconds. To assess whether the noise correctly accounts for the mismodelled acceleration, the 3σ bounds of the uncertainty are assessed together with the deviations in position due to drag for a single satellite, to determine whether the covariance correctly encompasses the errors. The result is shown in Figure 5.5. It was found that the matrix $\mathbf{Q}$ needs to be multiplied with a factor equal to 10^4 to ensure that the noise fully compensates for the mismodelling. The fact that $\mathbf{Q}$ needs to be larger than expected could be explained by the fact that the acceleration due to drag also has an influence on the other accelerations. Drag will namely decrease the altitude of a satellite, and thus an accumulation of acceleration differences will occur. The matrix $\mathbf{Q}$ could be established based on the total acceleration, however in this case the choice was made to take $\mathbf{Q}$ still relatively small. Furthermore, in reality, two satellites are affected by the change in C_d, and thus the total drift in MD is larger, however the covariances of both satellites are also summed, so this drift should then be compensated for. The exact reason as to why $\mathbf{Q}$ needs to be larger than expected has not been thoroughly explored, this should be investigated in more detail in future research. To establish how well the process noise compensates for the mismodelling with $10^2\mathbf{Q}$, the 3σ bounds for this are also included in the figure.

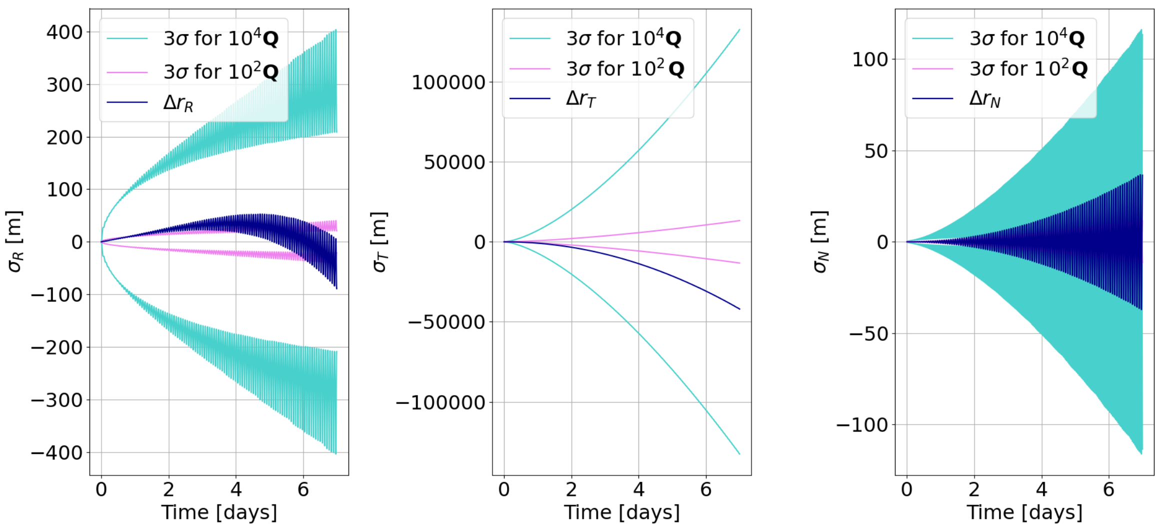

Figure 5.5: Positional error due to drag and 3σ bounds for $10^2\mathbf{Q}$ and $10^4\mathbf{Q}$.

As can be seen, $10^4\mathbf{Q}$ completely compensates for the mismodelling, while $10^2\mathbf{Q}$ only does so in the radial direction. Note, the $3\sigma_N$ bounds are underneath Δr_N, and do not fully encompass the error.

First, the results are shown for the simulated satellite on satellite collision including process noise with $10^2\mathbf{Q}$ in Figure 5.6.

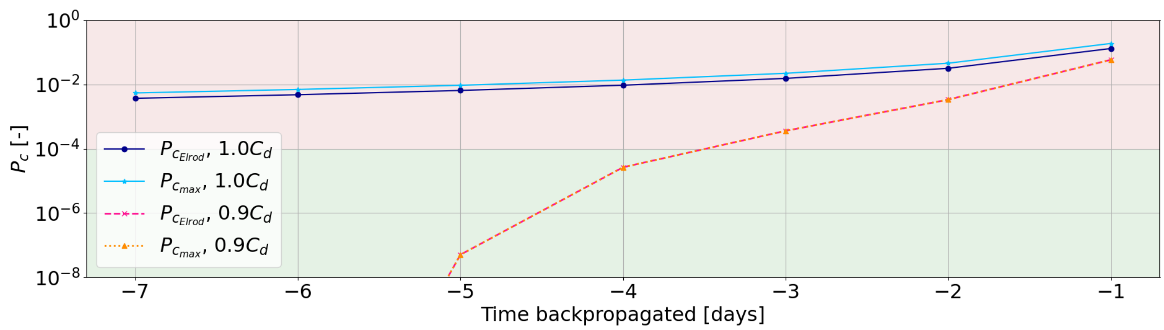

Figure 5.6: P_c for a satellite on satellite collision as a function of Δt_{back}, with process noise ($10^2\mathbf{Q}$).

A couple of observations can be made.

- The noise does not compromise the correctly modelled collision. For this case, the probability of collision still leads to the identification of a risky conjunction.
- For the mismodelled case, $P_{c_{Elrod}}$ and $P_{c_{max}}$ lie directly on top of each other. As can be seen, the closer to TCA, the higher the probability of collision. The mismodelled case can now also be correctly identified

as risky three days before TCA. Furthermore, the covariance growth has not led to the dilution effect. This is positive, as otherwise the covariance for the non-mismodelled case would also have been diluted. The time horizon available for reliable decision making is however still very short, as a collision avoidance maneuver should be planned two to one day(s) before TCA.

As observed in Figure 5.5, $\mathbf{Q}$ needs to be multiplied by 10^4 to completely compensate for the mismodelling. For the simulated satellite on satellite collision including process noise with $10^4\mathbf{Q}$ the results can be seen in Figure 5.7.

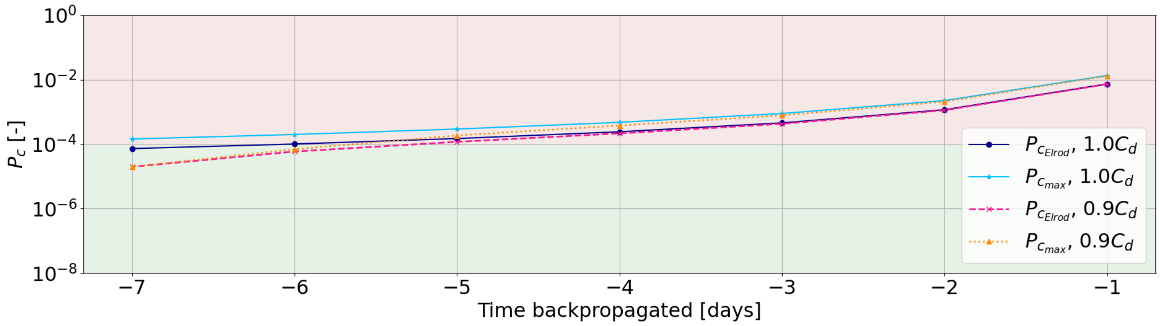

Figure 5.7: P_c for a satellite on satellite collision as a function of Δt_{back}, with process noise ($10^4\mathbf{Q}$).

As can be seen in the figure, the noise now also compensates for the mismodelling at $\Delta t_{back} = -7$ days. The probability would still not lead to a decision to mitigate, but it is significantly higher. The covariance growth due to process noise compensates for the effect of mismodelling for $\Delta t_{back} \geq -5$. However, the larger uncertainty now also leads to a lower probability for the correctly modelled case, because the probability becomes more diluted. The magnitude of $\mathbf{Q}$ is thus very important to establish correctly. In reality, the effect of a mismodelled acceleration might not be known. When the dynamical model is deliberately defined to be of low fidelity for efficiency, the matrix $\mathbf{Q}$ might be determined based on the effect of the omission of perturbing forces. However, when the accuracy of the dynamical model is affected due to inaccuracies in the estimation of parameters, the size of the process noise will be harder to establish.

5.3.2. Collision: Satellite x Debris

For the satellite on debris case, the results are shown in Figure 5.8. Note, no process noise was added to the covariance propagation. This was only done for the satellite on satellite collision, so for the following cases, no process noise is used.

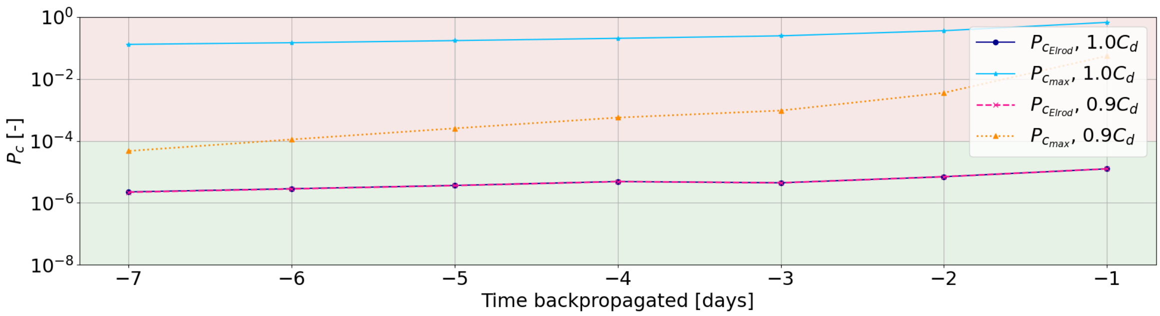

Figure 5.8: P_c for a satellite on debris collision as a function of Δt_{back}, without process noise.

Another number of observations can be made from this figure.

- For the case with the initially selected drag coefficient, $P_{c_{Elrod}}$ identifies the conjunction as safe for all Δt_{back}. This is probably due to the dilution effect as the debris covariance is large. This statement is supported by the fact that $P_{c_{max}}$ is above the safety threshold for all Δt_{back}. This implies that the dilution effect was properly mitigated. The Elrod formulation has thus led to seven false negatives, whilst the maximum P_c metric has led to seven true positives.

- For the mismodelled case, $P_{c_{Elrod}}$ is very similar to that of the correctly modelled case, for all instances of Δt_{back}. To check whether the atmospheric density has been mismodelled correctly, the miss distances found have been evaluated. The miss distance found for the correctly modelled case was approximately equal to 0.1 meters for all Δt_{back}. For the mismodelled case, the miss distances ranged from 23034 m for $\Delta t_{back} = -7$ days to 204 m for $\Delta t_{back} = -1$ day. The low probabilities are therefore probably due to the dilution effect. So, the large covariances lead to low probabilities, which are similar for both cases, independent of the miss distance at hand. The Elrod metric falsely identifies the situation as safe for all instances of the simulation.
- The maximum P_c metric for the mismodelled case does give different results from the correctly modelled case, which can also be expected. As was explained before, the changed drag coefficient will lead to a larger miss distance, and this effect grows with the propagated time Δt_{back}, as indicated by the miss distance range provided above. So, for a backward propagation time of seven to six days, the miss distance has increased to the point of identifying the collision as safe, even with the maximum P_c metric. However, the miss distance for $\Delta t_{back} \geq -6$ days has not grown as much and thus the maximum probability will still indicate a risky situation. This metric thus yields one false negative and six true positives. From this test case it can be concluded that it is better to have a wrong miss distance with a large uncertainty, than a wrong miss distance with a small uncertainty, which was the case for the satellite on satellite collision (Figure 5.2). Thus, one should never be too reliant on a predicted miss distance alone, or underestimate the uncertainty on a state. As can be observed from the false negative and true positives, the time horizon in which a satellite operator would need to determine whether to maneuver, is relatively short. A clear risk only becomes apparent from $t_{TCA} - 6$ days, and at this time, the probability still lies very close to the set threshold.

5.3.3. Collision: Debris x Debris

For a debris on debris conjunction it can be noted that even if the event is identified as risky, neither one of the objects can maneuver in order to mitigate the risk. However, the conjunction is still tested to evaluate the effectiveness of the metrics. Then, the following observations can be made for the debris on debris collision, for which the results are shown in Figure 5.9.

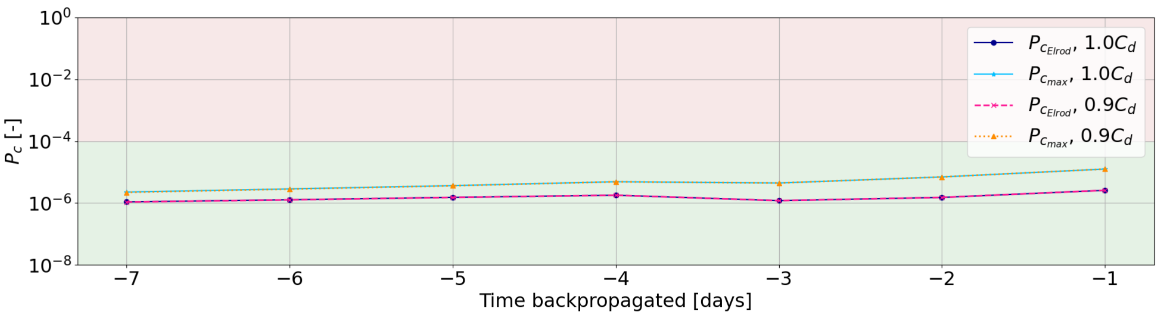

Figure 5.9: P_c for a debris on debris collision as a function of Δt_{back}, without process noise.

From Figure 5.9 it can immediately be observed that all results are false negatives.

- The debris on debris case has the largest joint covariance. So again, the Elrod results are affected by the dilution phenomenon for both the original and mismodelled dynamical models.
- The maximum P_c metric does not mitigate the dilution effect well enough to have the risk be quantified as unacceptable. As shown in Figure 2.4b, $P_{c_{max}}$ is found by scaling the joint covariance with the expectation that for some scale factor, a maximum occurs. This maximum will likely be close to the boundary of the robust and dilution region. It can however occur, that the range of scale factors used is not sufficient to ensure a crossing from the dilution region into the robust region. In that case, the extreme is not found. The

finite list of scale factors that are tested is a shortcoming of $P_{c_{max}}$, as it cannot be guaranteed that $P_{c_{max}}$ will be found unless one would scale the covariance until convergence. According to the NASA CARA SKD documentation, the metric is implemented such that the code does search for $P_{c_{max}}$ until convergence is reached [63]. So the reason for the low maximum probability has not been established with certainty.

- The results for $P_{c_{max}}$ and $P_{c_{Elrod}}$ are similar for the mismodelled and correctly modelled case. This leads to the belief that the scaled covariances used to find $P_{c_{max}}$ are again still too large and thus again lead to a diluted probability for the mismodelled case.

5.3.4. Near Miss: All Cases

A near miss has been simulated by setting the miss distance equal to 3HBR, which is approximately equal to 80 m for the Starlink on Starlink conjunction. For all cases, an operator should thus choose to not mitigate the collision risk. The miss distance is divided equally over the RTN directions. Again, these cases are simulated without the inclusion of process noise. The results for the near miss are shown in Figures 5.10 and 5.11. The figure for the satellite on satellite case has been left out of the report. The results can be briefly summarized as: all instances correctly identify the probability to be below 10^{-8}. This is expected, as the covariances for the satellite on satellite case are small, and the metrics will thus correctly identify a miss. Figure 5.10 shows the satellite on debris near miss.

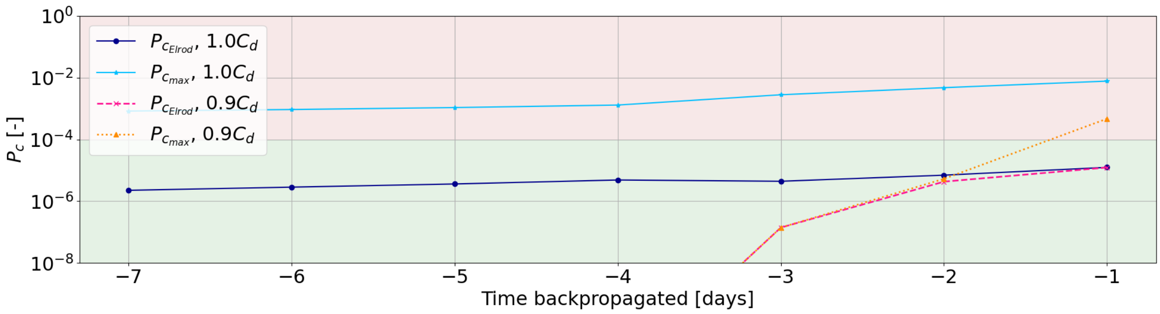

Figure 5.10: P_c for a satellite on debris near miss as a function of Δt_{back}, without process noise.

The following observations can be made based on the figure.

- The Elrod metric either correctly identifies the case as non-risky, or is affected by the dilution effect, as the debris covariance is large. Since the maximum P_c metric has raised the probabilities above the 10^{-4} threshold for all Δt_{back}, the latter is more likely. These elevated probabilities lead to the occurrence of seven false positives. These false positives occur due to the fact that $P_{c_{max}}$ is a conservative method of quantifying the collision risk. This means that by the nature of the metric, it will flag more false positives compared to $P_{c_{Elrod}}$.
- The miss distances for the mismodelled case have again grown from the original set miss distance. Thus, the Elrod results either represent the correct risk again, or they are affected by the dilution effect. The maximum P_c values have not grown as much, due to the increased miss distance. It can be seen that $P_{c_{max}}$ does increase at $\Delta t_{back} = -1$ day, as the miss distance after this propagated time is closer to the initially defined near miss. This results in another false positive.

Figure 5.11 shows the debris on debris near miss.

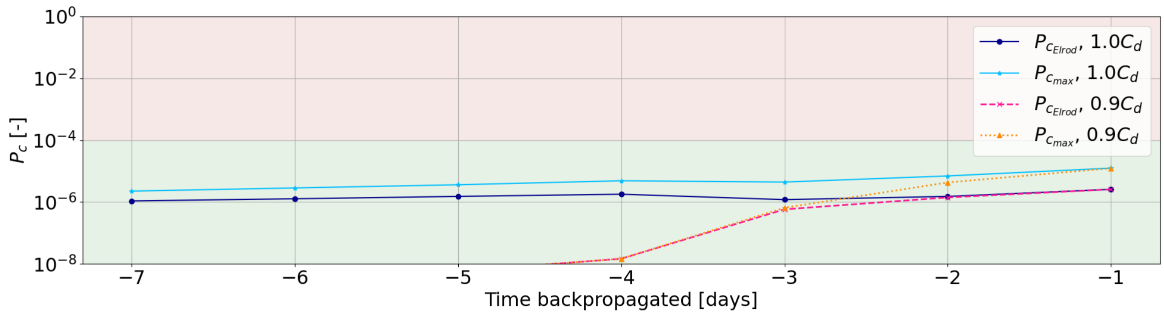

Figure 5.11: P_c for a debris on debris near miss as a function of Δt_{back}, without process noise.

As can be seen in the figure, the conjunction is identified as safe in all cases for all Δt_{back}, either because of the dilution effect or due to the large MD. Similarly to the debris on debris case for the collision, $P_{c_{max}}$ does not seem to mitigate the dilution effect completely. It can be noted however that the mismodelled and correctly modelled results are less in line with each other than was the case for the collision.

5.3.5. Large Miss: All Cases

The large miss is simulated by setting the miss distance equal to 100HBR in every direction. Figure 5.12 shows the results for a simulated large miss. For the satellite on satellite case, all instances were correctly identified as safe again. The results for the satellite on debris and debris on debris case were almost identical, hence only the figure of the debris on debris case is shown in Figure 5.12.

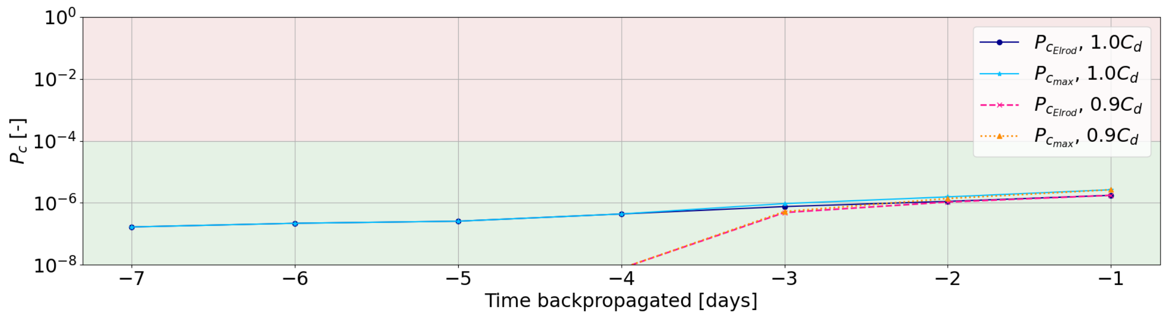

Figure 5.12: P_c for a debris on debris large miss as a function of Δt_{back}, without process noise.

- It is noteworthy that the probability is not very close to zero for all instances, even though the miss distance is very large. The probability is very low for the mismodelled case, but for the original drag settings the probability is in the order of 10^{-7}. Although this is well below the safety threshold of 10^{-4}, it is not as low as was the case for the satellite on satellite large miss, for which the probabilities were well below 10^{-8}. As the miss distances of both cases are equal, it can be concluded that this is an effect of the large uncertainties.

5.3.6. Key Takeaways from Analysis of the Current Practice

The conclusion that can be made from the results of running the first test cases, is that NASA CARA's SDK can be used for assessing the collision risk. However, it must be noted that the dilution effect is not always mitigated completely by $P_{c_{max}}$ when one deals with a large joint covariance. Furthermore, mismodelling of the dynamical model does have a significant effect on the conjunction risk assessment, and it was found that it is especially detrimental to underestimate the uncertainty on the states. Moreover, the magnitude of the process noise can be difficult to determine, especially if the inaccuracies are due to the misestimation of parameters. For the deliberate omission of perturbing forces in the dynamical model, $\mathbf{Q}$ may be defined more easily. Increasing the noise can however have an effect on the problem of having a large covariance. As known, large covariances will lead to a diluted probability, and the growth of the covariance during propagation will limit the time horizon in which operators can make a reliable decision. Although noise can be incorporated in the propagation to account for errors in the dynamical model, this will further increase the covariance size. Lastly, the maximum P_c metric proved to be more conservative than vanilla P_c as expected.

5.4. OPM implementation

From literature it has become clear that the growing number of space debris will lead to a growing number of conjunctions [69]. This could thus lead to the conclusion that it is important to decrease the amount of false alarms, as this number might become unmanageable otherwise. However, the previous analysis actually showed a higher amount of false negatives that one could be worried about. Furthermore, as was seen in the previous section, $P_{c_{max}}$ did not always completely mitigate the dilution effect, such as for the simulated debris on debris collision. The OPM metric uses a conservative method of assessing the collision risk, and thus this metric could be used to decrease the number of false negatives. The performance of the metric has been evaluated on the test cases used for the Starlink on Starlink conjunction.

5.4.1. Verification OPM Metric

Before the risk assessment is applied to the various test cases, the implementation has been verified using results found in the work of Delande et al. [21]. In the paper, the first test case from Alfano [9] was used. The initial states as given in the paper have been propagated to TCA by Delande et al. [21]. However, as the dynamical model used for the propagation is different, the states at TCA as found in the NASA CARA SDK documentation have been used instead [63]. The states at TCA are given in Table 5.4.

Table 5.4: States at TCA from Alfano's first test case, from Reference [9].

	Deputy	Chief
x [m]	153446.7645602800	153447.2642029000
y [m]	41874155.8695660000	41874156.3699030000
z [m]	0.0	4.9999660258
v_x [ms^{-1}]	3066.8747609105	3066.8647607073
v_y [ms^{-1}]	-11.3736149565	-11.3636148179
v_z [ms^{-1}]	0.0	-0.0000013581

The covariances, which can also be found in Reference [9], have been scaled, and the probability ($P_{c_{Foster}}$) and credibility (U_c) have been calculated for each scaled joint covariance. The miss distance resulting from the states defined in Table 5.4 is equal to 5.05 m. When setting the HBR equal to 15 m, a collision thus occurs. When setting the HBR to be smaller than the miss distance, a miss is simulated. The behavior of U_c and $P_{c_{Foster}}$ as a function of the covariance size for HBR = 15 m is shown in Figure 5.13a. Figure 5.13b shows the behavior of U_c and $P_{c_{Foster}}$ for HBR = 2 m.

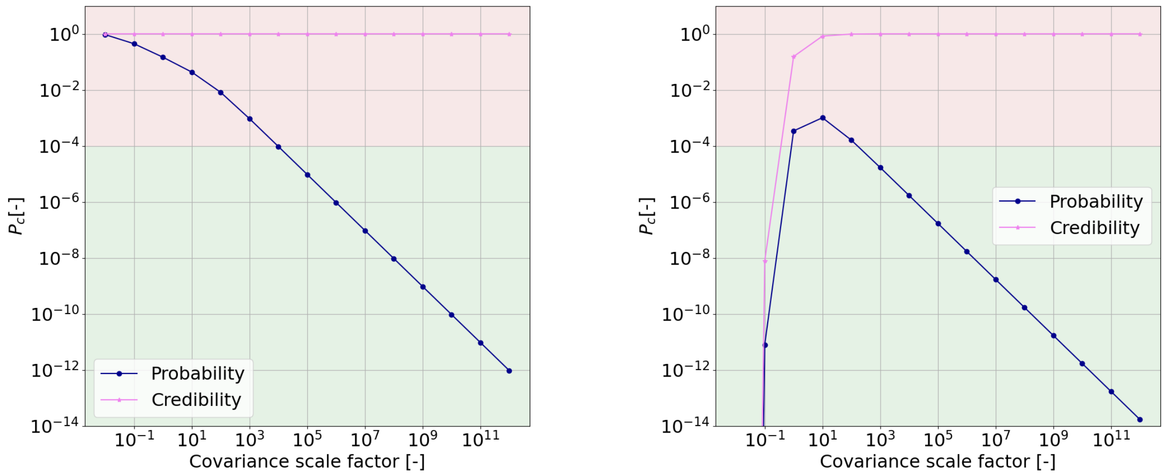

(a) Collision.

(b) Near miss.

Figure 5.13: P_c and U_c as a function of the covariance scale factor.

As can be seen in Figure 5.13a, the probability of collision indicates that the collision can be identified as risky for a covariance scaled with a factor lower than 10^4. However, as the covariance increases, the probability of collision decreases due to the dilution effect. To the contrary, the credibility stays equal to one, independent of the covariance size. This can be explained by the fact that U_c is computed as supremum, rather than the integral. So in the limit that the uncertainty goes to infinity, the credibility becomes one. For the near-miss case in Figure 5.13b, the probability of collision behaves as expected. It starts low for a small covariance, indicating that the probability is robust. The probability grows to a maximum for a scale factor of 10^1. Then, the probability of collision becomes diluted and decreases again. The credibility also starts low, as the covariance is small and the objects will not collide. Then, as the covariance grows, the credibility grows as well, indicating the increased ignorance. It can be noted that the credibility is larger than $P_{c_{max}}$. This indicates that the OPM metric is more conservative than the maximum probability metric. The results found match the results presented in the paper written by Delande et al., and thus the correct implementation of the metric has been verified. The two figures highlight the issue that P_c cannot always distinguish situations with a large covariance to be unlikely (left side of Figure 5.13b) or uncertain (right side of Figures 5.13a and 5.13b) [21]. OPMs can be used to make this distinction. The use of OPMs leads to a conservative assessment of the collision risk. It should be pointed out that the credibility is low on the left side of Figure 5.13b. The credibility can thus correctly determine whether the conjunction scenario represents a low-risk situation as well. So, although the metric is conservative, it can reliably screen for safe conjunctions in the robust region. Based on the results obtained, it is expected that the OPM metric will offer more reliability in mitigating the dilution effect compared to the maximum probability of collision. Specifically, the credibility at an unscaled covariance (10^0) is larger than $P_{c_{max}}$ found at 10^1. The difference in computation lies in the fact that $P_{c_{max}}$ is computed probabilistically through covariance scaling, whilst OPMs are calculated in a possibilistic manner.

It is interesting to note that the difference between the credibility and vanilla probability might also be utilized to determine whether additional tracking data would be needed. When the threshold set by an operator lies in between the upper and lower boundary of the probability, it is known that the available data is not sufficient enough to say something meaningful about the conjunction at hand, as mentioned before. The difference between U_c and L_c is referred to as ignorance [21]. The difference between P_c and U_c could also be studied however. When investigating these difference in Figures 5.13a and 5.13b, it can be noted that for the collision in Figure 5.13a, the difference between these two quantities is very low for a low uncertainty. As the uncertainty increases, the difference between the risk metrics also increases. The same can be noted for the miss visualized in Figure 5.13b. The difference $U_c - P_c$ might thus be used as an indication of the extent to which a conjunction needs additional tracking data. This might be useful especially when the number of conjunctions increases even further due to the growing space debris environment, and data collection for conjunctions might need to be prioritized.

The use of OPMs has been tested on the Starlink on Starlink simulations. The same threshold has been used as before for a risky or acceptable conjunction, namely 10^{-4}.

5.4.2. Collision: Correctly Modelled Cases

First, the results are discussed for the simulated collision with a correctly modelled dynamical model. In Figures 5.2 and 5.8 it was shown that the 2D risk assessments correctly identified the conjunctions for a satellite on satellite collision and a satellite on debris collision as risky for all instances of backward and forward propagation. However, for the debris on debris collision, the risk was identified as acceptable, even by $P_{c_{max}}$, as shown in Figure 5.9. The OPM metric has also been applied to all three collision cases to find the upper probability. For the satellite on satellite collision, and the satellite on debris collision, the results are discussed without the inclusion of figures, as the vanilla P_c calculations or $P_{c_{max}}$ calculations had already identified the conjunctions as risky. For these two cases, the credibility was found to be equal to one for every backpropagated time Δt_{back}. This is as expected, due to the fact that the metric is more conservative compared to the vanilla P_c and $P_{c_{max}}$ metrics. A more interesting case to study in more detail is the debris on debris collision, as this case was falsely identified as safe. Figure 5.14 shows the results for $P_{c_{Foster}}$, $P_{c_{max}}$ and U_c. The formulation derived by Foster and Estes has been chosen to demonstrate that the results for this formulation are almost identical to the results found with Elrod's formulation of the probability of collision.

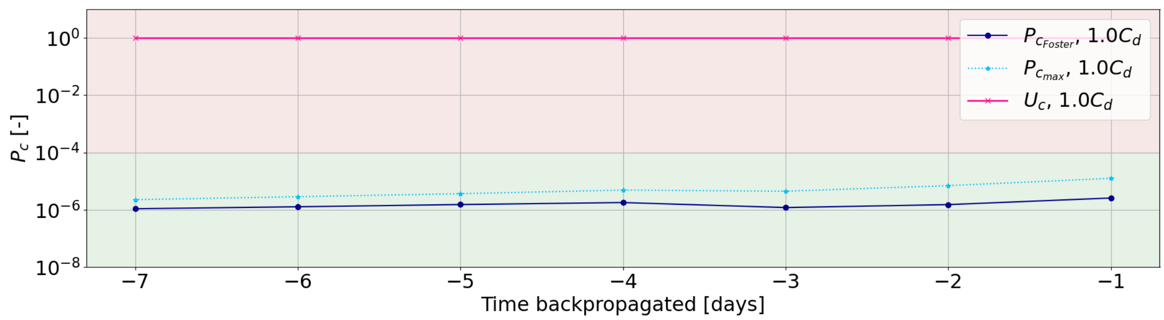

Figure 5.14: P_c and U_c for a debris on debris collision as a function of Δt_{back}, without process noise.

As can be seen, the upper bound of the probability is again equal to one, whilst the other two metrics showed results below 10^{-4} due to the dilution effect. As vanilla P_c is below the safety threshold, it is certain that the lower boundary of the probability lies below this threshold as well. So, even though the formulation of the lower boundary has not been derived yet, it is certain that it will be below the safety threshold. Hence, it can be concluded that, based on the OPM metric, the collision risk is qualified as undetermined. Therefore, the data available for the conjunction is insufficient, and additional data is required. As the collision risk is undetermined, it remains undetermined whether a true positive, true negative, false positive or false negative has occurred. However, it is at least certain that the risk is not safe, which could be qualified as true positive. Furthermore, the dilution effect is correctly mitigated.

5.4.3. Collision: Mismodelled Cases

For the mismodelled cases, the satellite on satellite collision can also provide useful information on the performance of the OPM metric. For a mismodelled ($0.9C_d$) satellite on satellite collision without process noise, it was shown that the previously tested metrics almost always provided a false sense of security. Therefore, it becomes of interest to investigate whether the OPM metric could address this issue. For this case, the results are shown in Figure 5.15.

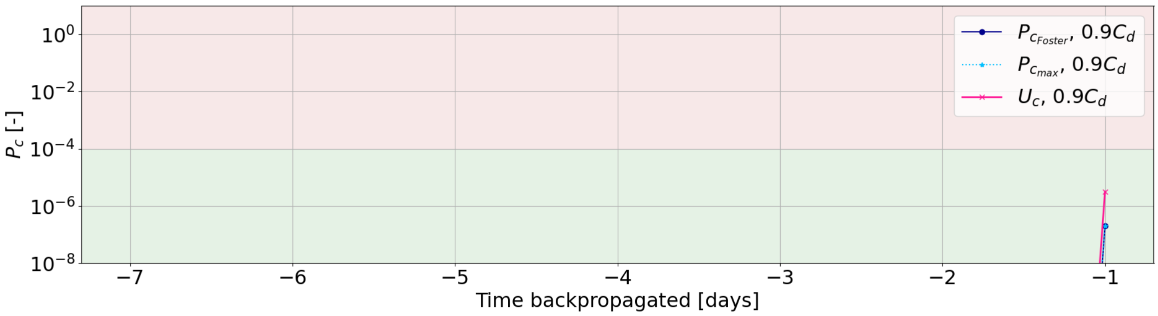

Figure 5.15: P_c and U_c for a satellite on satellite collision as a function of Δt_{back}, without process noise.

As can be seen, the OPM metric does not mitigate the problem of mismodelling for a satellite on satellite collision. This can be explained by the fact that the uncertainty for this case is low, so the upper boundary and theoretical lower boundary will be closely bound around the actual probability of collision. As the drag parameter causes a drift from the actual miss distance, this will result in a low probability of collision, and thus a low credibility as well. This proves the statement in the paper of Delande et al., where it is stated that if the knowledge of the observer is incorrect, the upper probability will also be incorrect. Seven false negatives have occurred.

For the mismodelled ($0.9C_d$) simulated satellite on satellite collision with process noise ($10^2\mathbf{Q}$) the results are shown in 5.16.

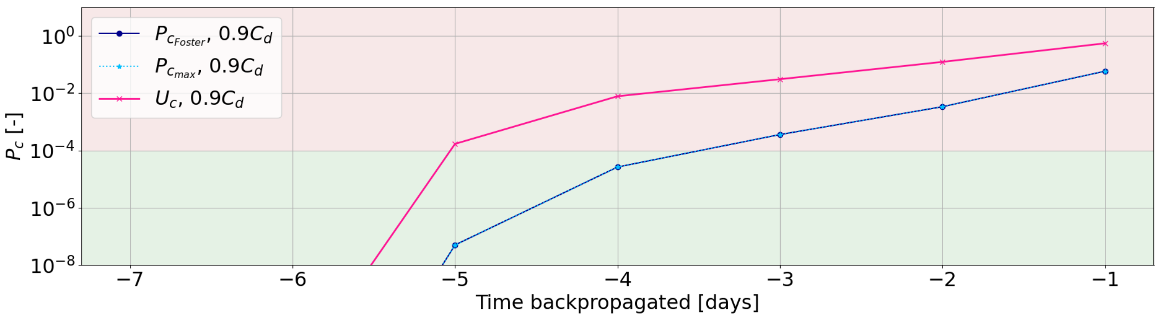

Figure 5.16: P_c and U_c for a satellite on satellite collision as a function of Δt_{back}, with process noise ($10^2\mathbf{Q}$).

As can be seen, the credibility is above 10^{-4} for $\Delta t_{back} \geq -5$ days. Again, for $\Delta t_{back} = -5$ days and $\Delta t_{back} = -4$ days it is certain that the lower boundary is below the safety threshold, as it will be below P_c. At these times, the risk will thus be undetermined, and additional data is required. For $\Delta t_{back} \geq -3$ days, the risk is quantified as unacceptable, as vanilla P_c is also above the threshold. Hence five true positives and two false negatives have occurred. Based on $P_{c_{Elrod}}$ and $P_{c_{max}}$, the conjunction would not have been flagged as risky before $\Delta t_{back} = -3$ days, introducing four false negatives. OPMs thus provide a more reliable mitigation of the dilution effect compared to $P_{c_{max}}$ for an increased uncertainty. Therefore, it is more robust for mismodelled cases. For the simulation for which the noise was further increased ($10^4\mathbf{Q}$), the credibility was well above the safety threshold for both the correctly modelled and mismodelled case for all Δt_{back}. Thus, the OPM metric provides a reliable assessment of the collision risk due to its conservative nature. And again, the need to have $\mathbf{Q}$ correctly estimated is stressed.

For the mismodelled satellite on debris collision without process noise, $P_{c_{max}}$ led to the identification of a risky conjunction six days before TCA (Figure 5.8). The results for the OPM metric can be seen in Figure 5.17.

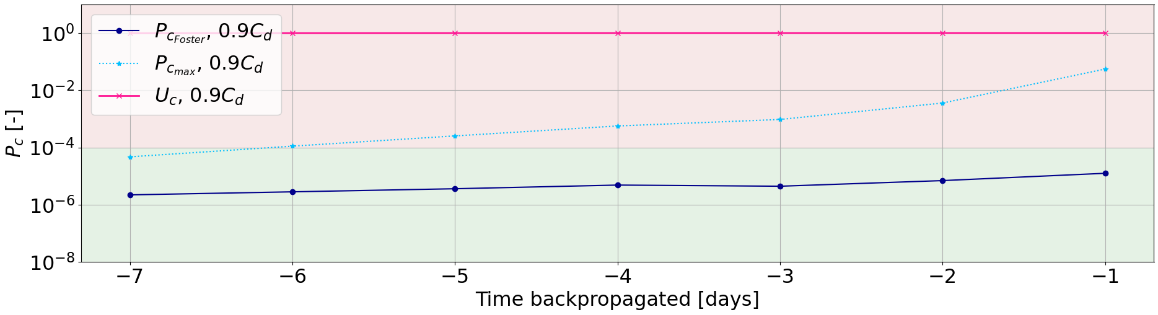

Figure 5.17: P_c and U_c for a satellite on debris collision as a function of Δt_{back}, without process noise.

As can be seen in the figure, the OPM metric again correctly identifies the collision as undetermined (lower bound will be below $P_{c_{Foster}}$) well before TCA, and earlier than $P_{c_{max}}$ identifies the conjunction as risky. So, in addition to effectively mitigating the dilution effect, the metric allows for an earlier identification of the risk compared to vanilla P_c or max P_c, as also seen in Figure 5.16. Although operators might not decide to mitigate a conjunction solely based on this metric due to its conservative nature, it allows them to become aware of the risk earlier and request additional tracking data, thereby extending the time horizon for potential action.

For the debris on debris case, the dilution effect was not mitigated entirely by $P_{c_{max}}$. The OPM metric was also tested on this case, and again, due to the uncertainties introduced by the presence of debris, the credibility was found to be equal to one, independent of the backpropagated time. Thus, for a mismodelled conjunction including at least one debris object, the OPM metric complements the metrics tested before.

5.4.4. Near Miss: Correctly Modelled Cases

For the near miss and large miss simulations, only the results for the correctly modelled simulations are discussed, all run without process noise. In Figure 5.18, the results for a simulated satellite on satellite near miss can be observed.

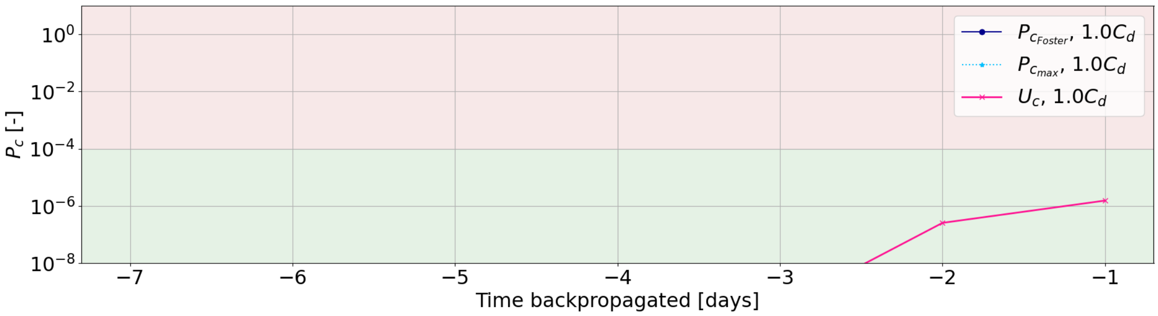

Figure 5.18: P_c and U_c for a satellite on satellite near miss as a function of Δt_{back}, without process noise.

The former two risk metrics studied, $P_{c_{Elrod}}$ and $P_{c_{max}}$, both led to the identification of a safe conjunction, as discussed before. The credibility assessment also leads to a safe interpretation of the conjunction (seven true negatives). This demonstrates that the metric will correctly identify a conjunction as safe when it is, given the defined uncertainty magnitudes for satellites and a near miss of approximately 3HBR. In such cases, an operator should not need to take a risk mitigation action. However, one thing to note is that the credibility grows as the time for which the states are backward and forward propagated decreases. This is contrary to what one might expect, as the shorter the propagation time, the smaller the covariance. Furthermore, the smaller the covariance, the closer the upper and theoretical lower bound on the probability of collision are together. Thus, the expectation would be that U_c is larger for a larger backpropagated time Δt_{back}. To demonstrate that the joint covariance at $\Delta t_{back} = -1$ day is indeed smaller than the joint covariance at $\Delta t_{back} = -7$ days, Table 5.6 has been created.

Table 5.5: Uncertainty in the different directions for different backpropagated times.

Δt_{back} [days]	σ_R [m]	σ_T [m]	σ_N [m]
1	4.57	36.64	7.58
7	1.64	244.09	4.38

As can be observed, the covariances have grown as expected. The sample size used to calculate U_c has also been increased to determine whether this changes the outcome, but no difference was found. This behavior should thus be further investigated.

For the near-miss satellite on debris conjunction, the credibility was again well above the set threshold. The maximum P_c had also identified the conjunction as risky before (Figure 5.10). So, the high credibility is as expected. The near miss for the debris on debris case was identified as safe by both $P_{c_{Elrod}}$ and $P_{c_{max}}$, as was seen in Figure 5.11. Due to the high uncertainties however, the credibility is again equal to one, as can be seen in Figure 5.19.

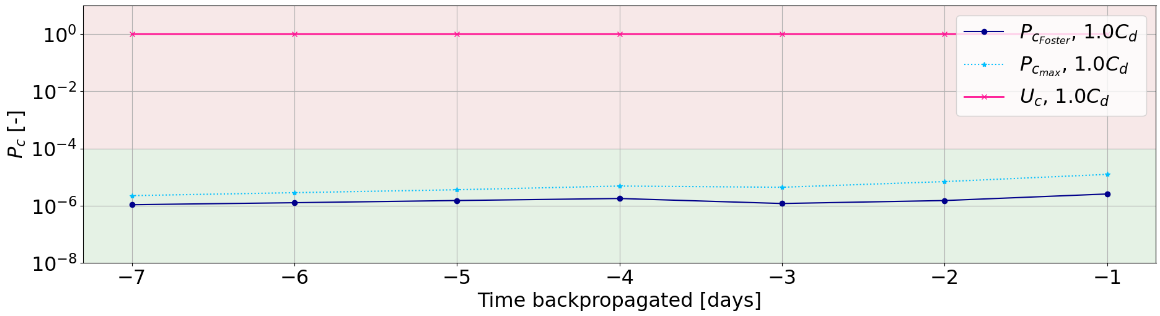

Figure 5.19: P_c and U_c for a debris on debris near miss as a function of Δt_{back}, without process noise.

As vanilla P_c is below the safety threshold for both the satellite on debris near miss and the debris on debris near miss, again, it can be concluded that the risk is undetermined. As the conjunction is simulated to be safe and the risk is not identified as such, seven false positives are flagged.

5.4.5. Large Miss: Correctly Modelled Cases

The simulated large miss for a satellite on satellite conjunction had led to $P_{c_{Elrod}}$ and $P_{c_{max}}$ being below 10^{-8}. The upper probability has also been identified to be below 10^{-8}, and therefore, since the figure for this case is empty, it is left out of the report. The case again proves however, that although the OPM metric is conservative, it will identify a safe situation for a low covariance and a large miss. This is important because of the large number of false positives and/or indeterminate results that the metric will nonetheless introduce. For the satellite on debris and debris on debris large miss, the results are again very similar. Hence, again, only the results for the debris on debris case are shown in Figure 5.20.

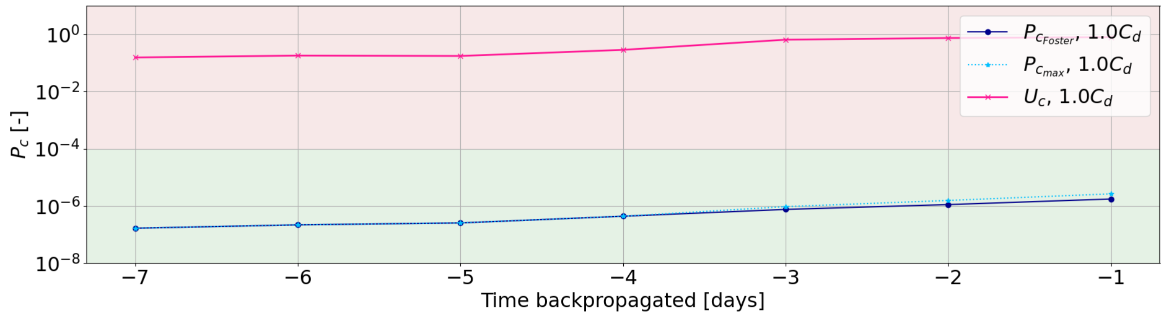

Figure 5.20: P_c and U_c for a debris on debris large miss as a function of Δt_{back}, without process noise.

It can be seen in Figure 5.20 that although $P_{c_{Foster}}$ and $P_{c_{max}}$ had led to the identification of a safe situation, the same cannot be concluded for the credibility. The large miss including at least one debris object, is a scenario for which the occurrence of a collision is both unlikely and uncertain. Again, although the equation for the lower boundary has not been derived yet, it can be concluded that the lower boundary lies below the safety threshold, as vanilla P_c lies below the threshold as well. Hence, the upper and lower boundary encompass the safety threshold, and the collision risk is undetermined. Therefore, seven false positives are flagged, as the risk cannot be discarded based on the metric. Note, again U_c seems to be larger for a shorter propagation time, as was the case for the near miss. This behavior should be further examined.

5.4.6. Key Takeaways Outer Probability Measure Metric

To conclude, the outer probability measures metric complements the different introduced collision risk assessments. The metric shows to be more reliable in mitigating the dilution effect compared to $P_{c_{max}}$. Even though the lower probability has not been derived yet, sometimes, the credibility can be used in combination with vanilla P_c to determine whether a conjunction is safe or undetermined. The metric is very conservative, and thus the number of false alarms will significantly increase when using the metric. Although the metric is very conservative, it still correctly identifies safe cases when the uncertainty is small. Thus, using the metric, a safe conjunction can be dismissed with greater reliability. As stated by Delande et al., the metric can be used to distinguish unlikely cases from uncertain ones [21].

5.5. Results Relative Orbital Parameters Metric

The relative orbital parameters metric has been used to test whether the time horizon available for decision making can be improved, using the conjunctions between Terra Sar X and Tandem X. The correct implementation of the metric is first evaluated.

5.5.1. Verification Relative Orbital Parameter Metric

The concept of using $\Delta\vec{e}$ and $\Delta\vec{i}$ to control a formation has been tested on TSX and TDX in former research [19]. TSX and TDX are flying in a controlled formation such that the configuration of the satellites stays the same. TSX will perform station-keeping maneuvers to stay within a tube of radius 250 m around a predefined reference trajectory [45] and will drift due to perturbations, whilst TDX will perform maneuvers to compensate for these changes in the orbit of TSX. The relative eccentricity and inclination vectors can be used to control the formation by studying when the angle between them becomes near orthogonal, and thus when a correcting maneuver needs to be made. A deviation of 30° from a parallel or antiparallel alignment is allowed before performing a maneuver [57].

The results found in Reference [19] can be used to verify the correct implementation of the method. The initial states defined for the satellites have been derived based on the states used by D'Amico et al. The differences in Keplerian elements are given by:

$$\Delta a = 0\,\mathrm{m},\ \Delta\vec{e} = \begin{bmatrix} 0 \\ \frac{300\ \mathrm{m}}{a} \end{bmatrix},\ \Delta\vec{i} = \begin{bmatrix} 0 \\ \frac{-1000\ \mathrm{m}}{a} \end{bmatrix},\ \Delta u = 0. \tag{5.2}$$

The chosen separations comply with the requirement of a small orbital difference ($\Delta\vec{x}_K \ll 1$). As can be seen, the relative eccentricity and inclination vectors were both chosen to only have a nonzero value in the y direction. Furthermore, the directions of the vectors were chosen to be opposite to each other. This ensures an antiparallel alignment of the two vectors. In the research carried out by D'Amico et al., the relative elements as defined in Equation 5.2 were added to the initial state of TSX as found on May 2006 [19]. For this research, the initial state of TSX at t_0 has been found by trial and error. It was defined as follows:

$$a_{TSX} = 6892945 \text{ m},\ e_{TSX} = 10^{-8},\ i_{TSX} = 97°,\ \omega_{TSX} = 270°,\ \Omega_{TSX} = 0°,\ M_{TSX} = 90°. \tag{5.3}$$

The final elemental differences added to the state of TSX to find the initial state of TDX at t_0 were then defined as:

$$\Delta a = 0,\ \Delta e = \frac{300 \text{ m}}{a},\ \Delta i = 0,\ \Delta\omega = -180°,\ \Delta\Omega = \frac{-1000 \text{ m}}{a \sin i_{TSX}}°,\ \Delta M = +180°. \tag{5.4}$$

The differences in $a,\ e,\ i,\ \Omega$ and u have been kept the same as defined in Equation 5.2. The difference in ω has been chosen such that $\vec{e}_{TSX}$ and $\vec{e}_{TDX}$ are pointing up and down respectively, to ensure that $\Delta\vec{e}$ is also in the y direction and is thus antiparallel with respect to $\Delta\vec{i}$. The mean anomaly M has been chosen such that with $u = \omega + M$, the set up still yields $\Delta u = 0$.

Using Equation 3.8, the relative eccentricity and inclination vectors have been found at t_0. To observe the behavior of the vectors and the angle separation between them over time, the states have been propagated for 30 days. The propagation has been performed with the propagation settings as defined in Table 4.2 in Step 5 of the methodology. The timestep has been set to 20 seconds, so that it is in line with the timestep used in the paper. The relative inclination and eccentricity vectors were then computed at every intermediate epoch. It must be noted that the results will not be entirely similar compared to the results found in Reference [19]. The reason for this is that there are no orbit-keeping maneuvers applied in this simulation, whilst they are in the simulation performed by D'Amico et al. To compensate for this, the physical characteristics of the satellites have been set to be the same. This ensures that the perturbing forces have the same effect on both trajectories, and thus the satellites will not drift apart. Figures 5.21a and 5.21b show the behavior of $\Delta\vec{e}$ and $\Delta\vec{i}$ over time. The vectors all originate from the origin $(0, 0)$, however the vectors are represented in scatter points here, such that the evolution over time can be clearly seen. Nevertheless, the initial vectors at t_0 have been visualized, together with the vectors at the time when they are closest to orthogonal. The time at which the vectors have a near-orthogonal geometry is equal to $t = 25.5$ days. At this moment in time, the radial and cross-track separations can vanish jointly, indicating a dangerous situation in the presence of a large along-track uncertainty. The figures show the results when calculating the vectors as defined in Equation 3.8 using mean orbital elements. The conversion of osculating elements to mean elements has been conducted using the Brouwer-Lyddane transformation [44]. Mean orbital elements are also used in practice [46].

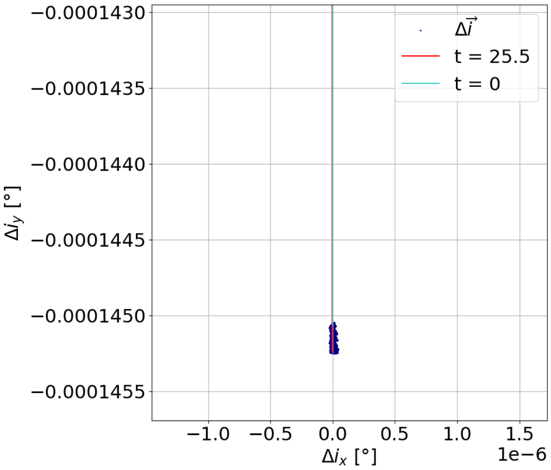

(a) The relative inclination vector over time.

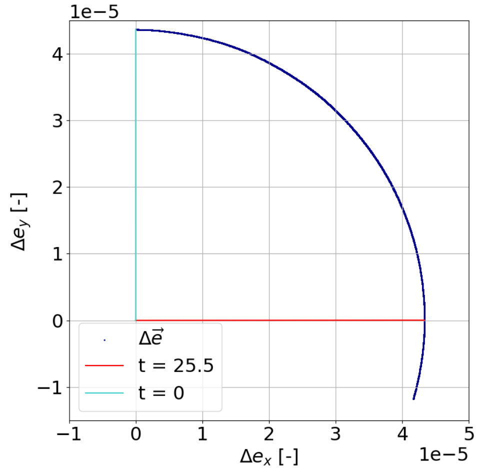

(b) The relative eccentricity vector over the course of propagation.

Figure 5.21: The relative inclination and eccentricity vectors over time.

As can be seen in Figure 5.21a, the relative inclination vector remains very stable over the course of propagation. This is in line with the results found by D'Amico et al. The vector remains stable due to the fact that the relative inclination Δi has been set to zero (not to be confused with the relative inclination vector $\Delta\vec{i}$, which is not equal to zero). Namely, when $\Delta i = 0$, this ensures that the ascending nodes of the orbits rotate at the same rate, and thus the relative vector stays stable [57]. Figure 5.21b shows the behavior of the relative eccentricity vector. The vector seems to drift more compared to the relative inclination vector. This drift can mainly be explained by the perturbing force due to the oblateness of the Earth [11]. The drift will cause the vectors to become orthogonal after some time, leading to the need for regular maneuvers to control the formation of TSX and TDX [11]. As can be seen, the vectors at t_0 are parallel, and the vectors at $t = 25.5$ days are nearly orthogonal. The radial and cross-track separations can also be plotted against each other. Figure 5.22 shows the separations for one orbital period every five days. As can be observed for the orbit at $t = 0$, when the cross-track separation is equal to zero, the radial separation is maximal and vise versa. To the contrary, for the most risky situation at $t = 25.5$ days, both separations can vanish jointly. The results are in line with the results found in Reference [19].

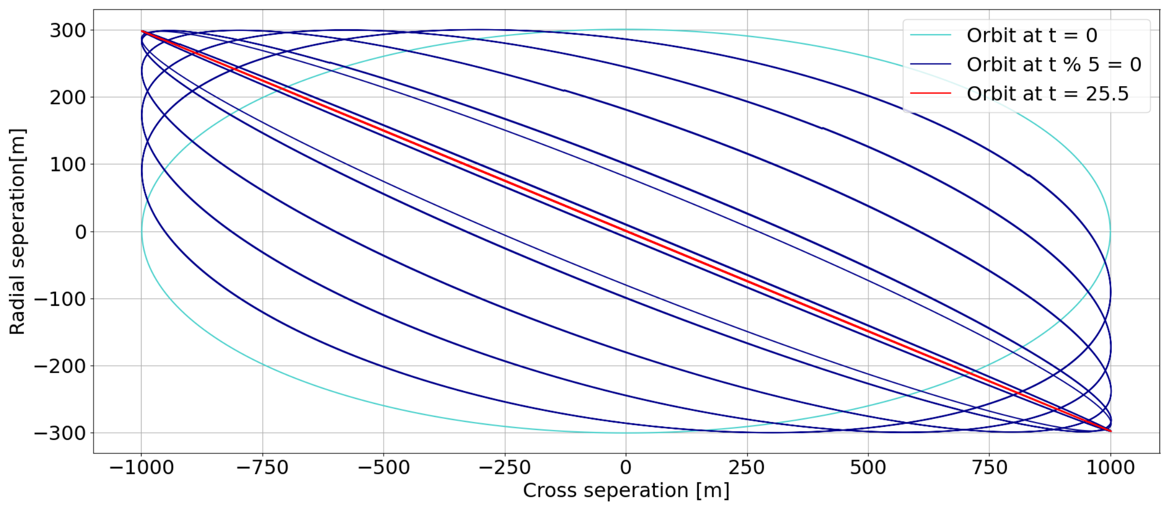

Figure 5.22: Ellipses drawn by TDX around TSX.

Figure 5.23 shows the angle separation $\Delta\gamma$ over time.

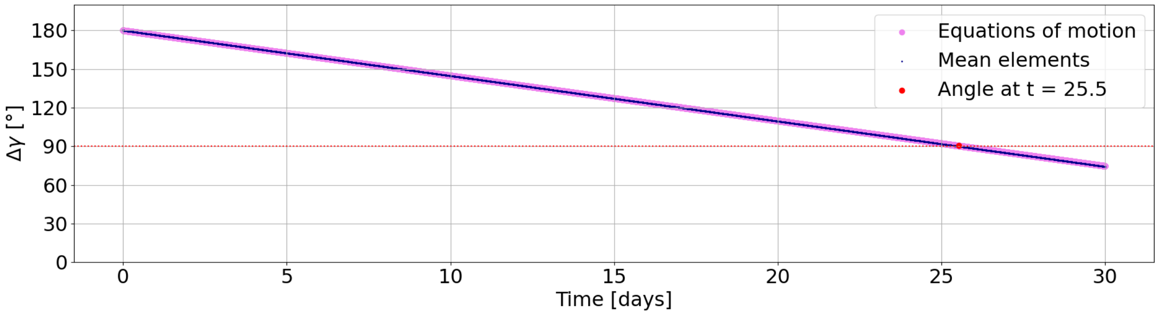

Figure 5.23: Angle separation over the course of propagation.

The results show that it takes 30 days to go from an angle separation of $180°$ to a separation of $60°$. In former research, it has been found that it would take approximately 17 days to move from an angle separation of $210°$ to a separation of $270°$, which means that one would have 17 days to respond and ensure an orthogonal alignment is not reached [51]. The relative eccentricity and inclination metric is thus very useful for controlling the TSX/TDX formation, as the metric provides a stable solution with timely notice if the geometry is moving towards a more risky situation.

Although the metric will provide a stable solution over time, it is important to note that the angle deviation cannot be used as risk assessment for conjunction analysis in solitary. Although either the radial or cross-track separation is maximal at a parallel geometry between the $\Delta\vec{e}$ and $\Delta\vec{i}$ vectors, this separation could still be lower than the HBR depending on the magnitudes of δi and δe, as can be seen in Equation 3.11. It is thus important to combine the miss distance with the angle deviation when assessing the collision risk. Furthermore, the expressions for the separations as introduced in Equation 3.10 are based on the fact that the orbits are bounded. So, zero drift in Δa and Δu is assumed. To test the use of the metric when this drift is nonzero, the states of TSX and TDX have been propagated again, but now with the mass of TDX set to 1.1 times the mass of TSX. This will namely cause the orbits to drift apart due to the difference in accelerations acting on the objects. This will lead to a drift in the ellipses drawn by TDX around TSX, as shown in Figure 5.24.

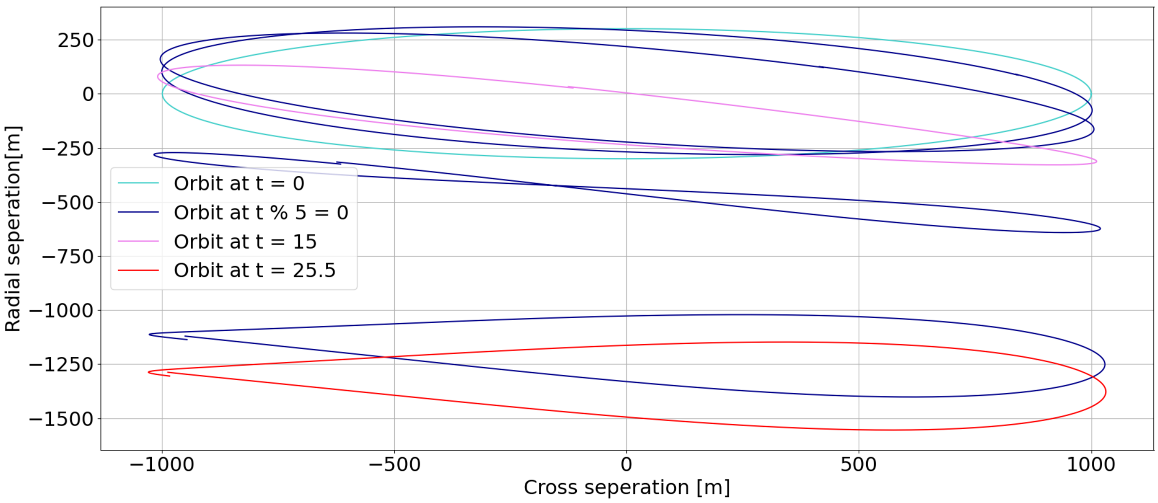

Figure 5.24: Ellipses drawn by TDX around TSX for a nonzero Δa.

As can be seen, due to the drift introduced by Δa, the orbit associated with the time for which $\Delta\gamma \approx 90°$ does not lead to a joint vanishing of Δr_R and Δr_N anymore. The drift now introduces a risky situation at $t = 15$ days, at which the ellipse crosses the origin. However, the angle at $t = 15$ days is approximately equal to $128°$, so the vectors are not aligned orthogonally yet. This can complicate the use and interpretation of the metric.

5.5.2. CDM data

The sixteen CDMs found for TSX and TDX have been used to analyse the usage of $\Delta\vec{e}$ and Δi for conjunction analysis. The conjunction geometry at t_{TCA} has been found and studied based on the information provided in the CDMs. Furthermore, the states provided in the CDM have an associated covariance which was used to determine the uncertainty on the angle deviation $\Delta\gamma$, as defined in Equation 3.9.

The uncertainty on the angle deviation was found using a Monte Carlo algorithm. The states of TSX and TDX have been sampled using a normal multivariate distribution. Both states were sampled individually, as both states have their own covariances. Then one can choose to either cross-combine the different samples or to pair the samples based on their place in the sample set. The latter methodology was chosen as cross-combining the samples can lead to over and under represented regions, whilst by pairing the samples, every sample is only used once. The sample size used (4 million) has been verified, as shown in Appendix E. The sampled states $\vec{x}_{TSX_i}$ and $\vec{x}_{TDX_i}$ yield sampled relative inclination and eccentricity vectors. The vectors have been found using the mean orbital element calculation (Equation 5.2), as this method is also used in reality [51]. The sampled vectors are shown in Figures 5.25a and 5.25b.

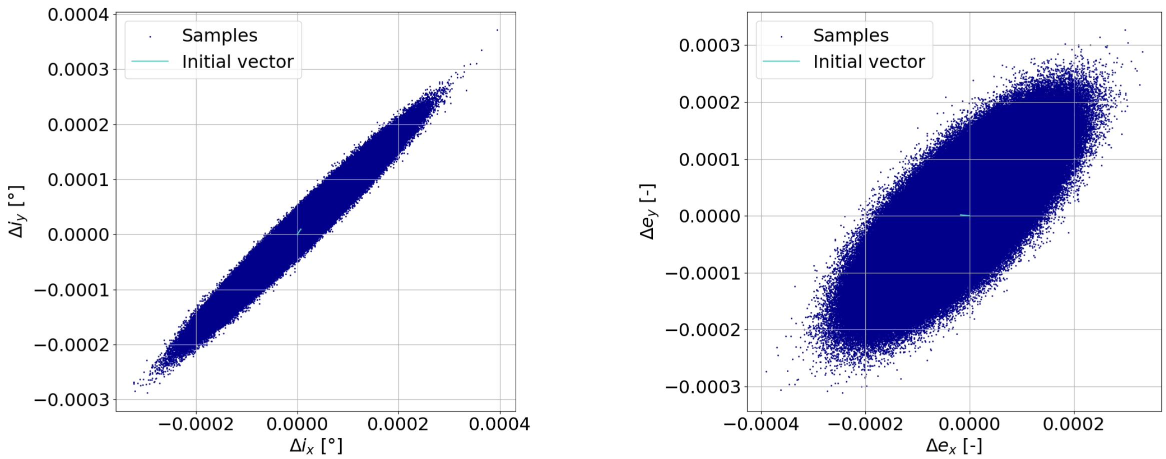

(a) The sampled relative inclination vectors for the CDM covariance.

(b) The sampled relative eccentricity vectors for the CDM covariance.

Figure 5.25: Sampled relative vectors as a result of the CDM covariance.

As can be seen, the effect of the uncertainty present in the CDM is large. The magnitudes of the individual standard deviations in the RTN frame, as provided in the CDM, are in the order of 10^2 m. The deviations found for $\Delta\vec{i}$ and $\Delta\vec{e}$ are larger than the deviations of the initial vectors as a result of propagating the states for 30 days, as shown in Figures 5.21a, **??** and 5.21b. Moreover, the distributions of $\Delta\vec{i}$ and $\Delta\vec{e}$ fully encompass the origin. This means that any angle between the two vectors is possible. Furthermore, a positive correlation can be observed between Δi_x and Δi_y, and similarly between Δe_x and Δe_y. This implies that either parallel or anti-parallel vectors will occur more often. The angle separation can be found for every sampled $\Delta\vec{e}_i$ and $\Delta\vec{i}_i$ pair, which leads to the distribution of $\Delta\gamma$ as shown in Figure 5.26.

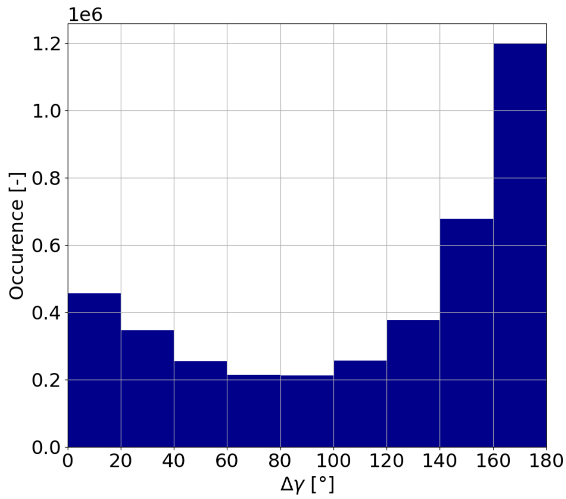

Figure 5.26: Distribution of the angle separation as a result of the CDM covariance.

The standard deviation of the distribution was found to be equal to $\sigma_{\Delta\gamma} \approx 60°$. Such an uncertainty on the angle deviation is too high, as the angle can only lie in between $0°$ and $180°$ when calculating the angle as defined in Equation 3.9. This interval is also shown in Figure 5.26. Thus, the uncertainty found in the CDM seems too high to use the geometry between $\Delta\vec{i}$ and $\Delta\vec{e}$ as a risk metric for conjunction analysis in a meaningful way. The fact that the uncertainty in the initial Cartesian states translates to such a large angular uncertainty is something that should be investigated further. Furthermore, the question arises as to how certain one needs to be of the initial states to be able to say something meaningful about the level of risk. For this research, the positional uncertainties have been defined to be in the order of 1 meter for satellites. The uncertainty on the angle deviation has also been determined for covariances scaled to have standard deviations in this magnitude. To evaluate this, the initial covariances found in the CDM have been scaled. Figures 5.27a, 5.27b and 5.28 show the results.

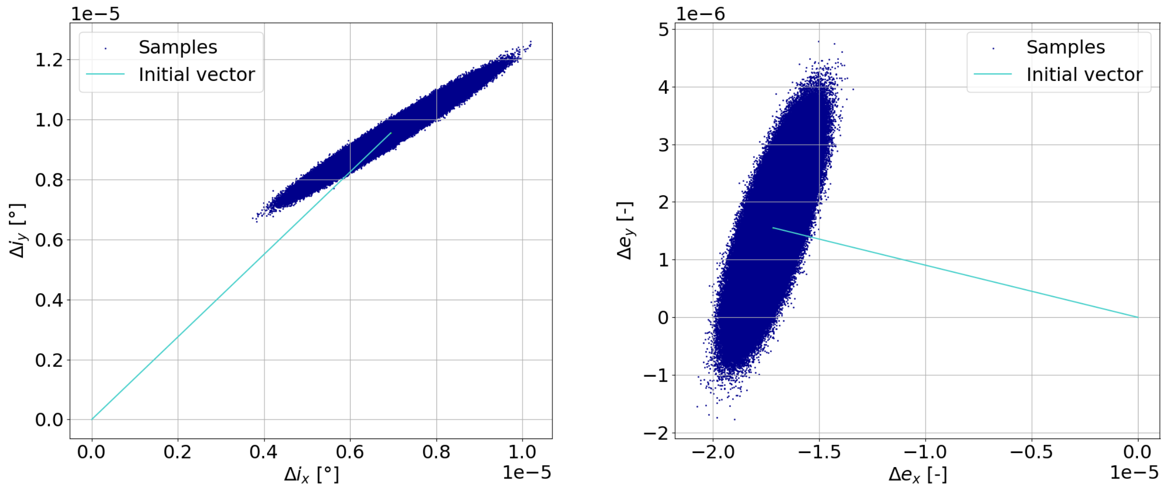

(a) The sampled relative inclination vectors for the scaled CDM covariance. **(b)** The sampled relative eccentricity vectors for the scaled CDM covariance.

Figure 5.27: Sampled relative vectors as a result of the scaled CDM covariance.

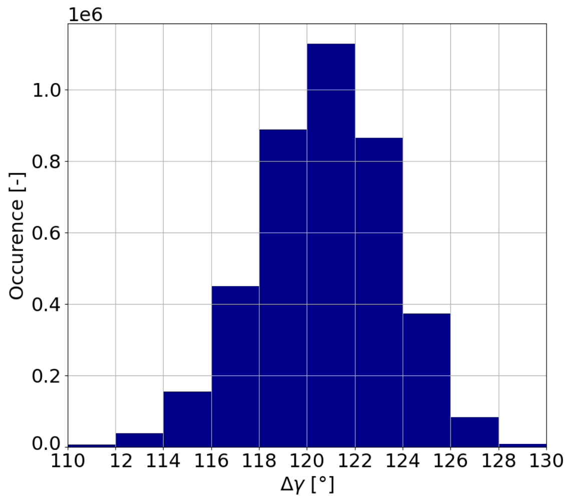

Figure 5.28: Distribution of the angle deviation as a result of the scaled CDM covariance.

As can be seen, the distributions of $\Delta\vec{i}$ and $\Delta\vec{e}$ do not encompass the origin, thus the uncertainty will lead to a smaller number of possible angles. Furthermore, the variations in the sampled vectors are now much lower, as expected due to the lower covariances. The standard deviation is now in the order of $1°$. So with a lower covariance, the metric shows more potential to be used for a qualification of the collision risk. To determine at which covariance magnitude the uncertainty on $\Delta\gamma$ will make the metric unusable, a plot has been made of the uncertainty on $\Delta\gamma$ as a function of the magnitudes of the covariances. The result is shown in Figure 5.29. The figure also includes the behavior of the uncertainty on the miss distance as a function of the covariance size. This way, the difference between the uncertainty behaviors can be studied in more detail. As a point of reference, the initial magnitudes of the standard deviations, as provided in the CDM, were previously documented to be in the order of 10^2 m.

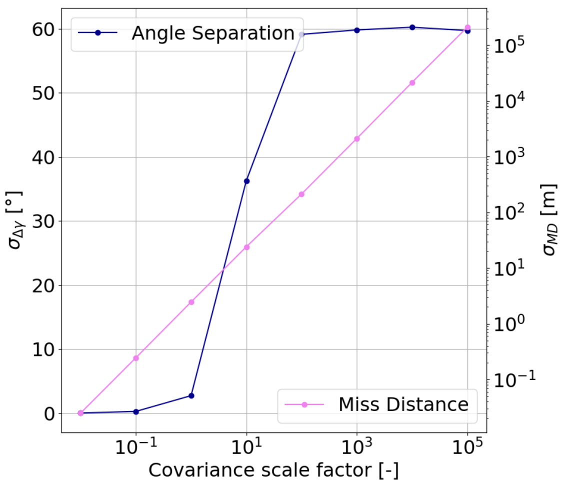

Figure 5.29: Uncertainty as a function of the covariance scale factor.

As can be seen in Figure 5.29 the uncertainty on the miss distance grows exponentially with exponentially growing covariances, as expected. The uncertainty of the angle separation however, blows up to $60°$ when the uncertainty on the position is higher than 1 meter. It must be noted that, the size of the uncertainty for which the angular uncertainty will blow up depends on the magnitudes of the vectors $\Delta\vec{i}$ and $\Delta\vec{e}$. Depending on these magnitudes, the origin will or will not be fully encompassed by the sampled vectors for a certain uncertainty. However, to be able to use this relative orbital parameters metric, $\Delta\vec{x}_K \ll 1$ must hold. Therefore, the hypothesis is that the uncertainty can not be too large for all cases, as the magnitudes of the vectors will always be relatively small. This should be further investigated and tested on various test cases.

From the figure, it can also be noted that when the covariance is scaled with a factor higher than 10^2, the standard deviation does not grow further as the possible values for $\Delta\gamma$ only range from 0 ° to 180°. Although σ_{MD} is also relatively large compared to an average HBR at for example a covariance factor of 10^2, this uncertainty is taken into account when calculating the probability of collision. A correct method of taking into account the uncertainty on the angle separation should thus be investigated to use the metric in a meaningful way. One could for example choose to study the angle closest to a risky situation within $\Delta\gamma \pm \sigma_{\Delta\gamma}$. Former research has shown that the achievable control accuracy for the TSX/TDX formation is approximately in the order of 10-20 m for the along-track direction, and 1-2 m for the radial and cross-track directions [57]. This can be achieved due to accuracy of the data available to the operators. However, such certain data is currently not available from the ground-based tracking data presented in the CDMs, and ideally one would have even smaller errors to ensure a precise quantification of the separation angle, as shown in Figure 5.29.

Although the states documented in the CDM are too uncertain to say something useful about the approach geometry, the angle deviations resulting from the states at t_{TCA} are shown in Figure 5.30 to see whether a pattern can be observed in the behavior of the angle. The figure includes the uncertainty on the angle deviation and the miss distance by means of error bars.

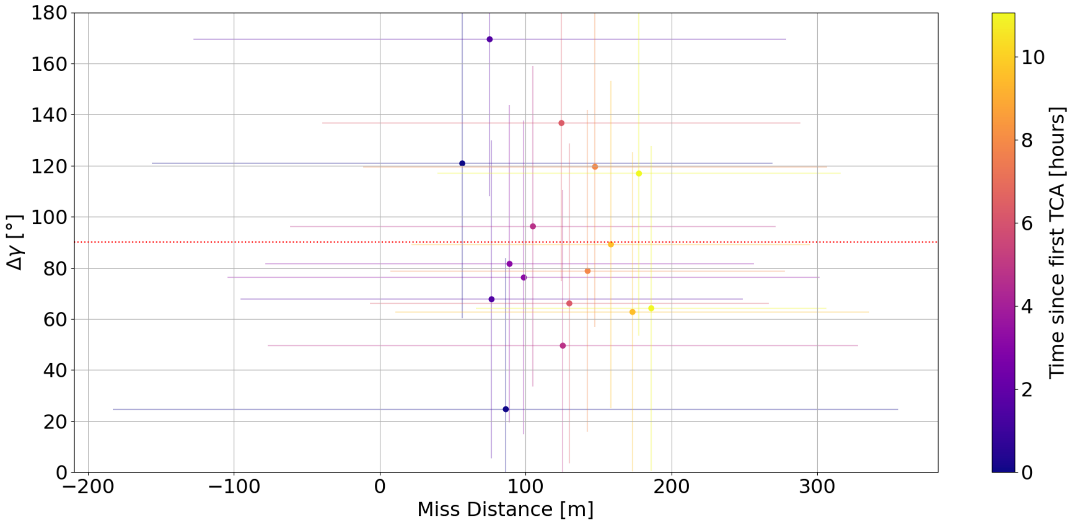

Figure 5.30: Angle separation at TCA with the uncertainty, for the sixteen TSX/TDX CDMs.

As expected, no clear pattern can be seen, due to the uncertainty on the angles. To conclude, it has been found that data in the CDMs is currently too uncertain to use the relative orbital parameters metric as risk assessment metric. To test how the metric could be utilized if the uncertainties were smaller, an ideal test case has been created.

5.5.3. Ideal Test Case

For the ideal test case, the states defined in Equations 5.3 and 5.4 have been used as a basis. The separations between the two orbits as introduced in the latter equation have been changed to ensure a close approach between the two spacecraft. The changed parameters have been defined as:

$$\Delta\vec{e} = \begin{bmatrix} 0 \\ \frac{30\text{ m}}{a} \end{bmatrix}, \; \Delta\vec{i} = \begin{bmatrix} 0 \\ \frac{-40\text{ m}}{a} \end{bmatrix}, \; \Delta\Omega = \frac{-40\text{ m}}{a\sin i_{TSX}}^{\circ}. \tag{5.5}$$

Again, the states have been propagated forward for 30 days, as described in Section 5.5.1, to study the behavior of the relative motion between the two spacecrafts. The ellipses drawn by TDX around TSX were again visualized. For this test case, the results are shown in Figure 5.31.

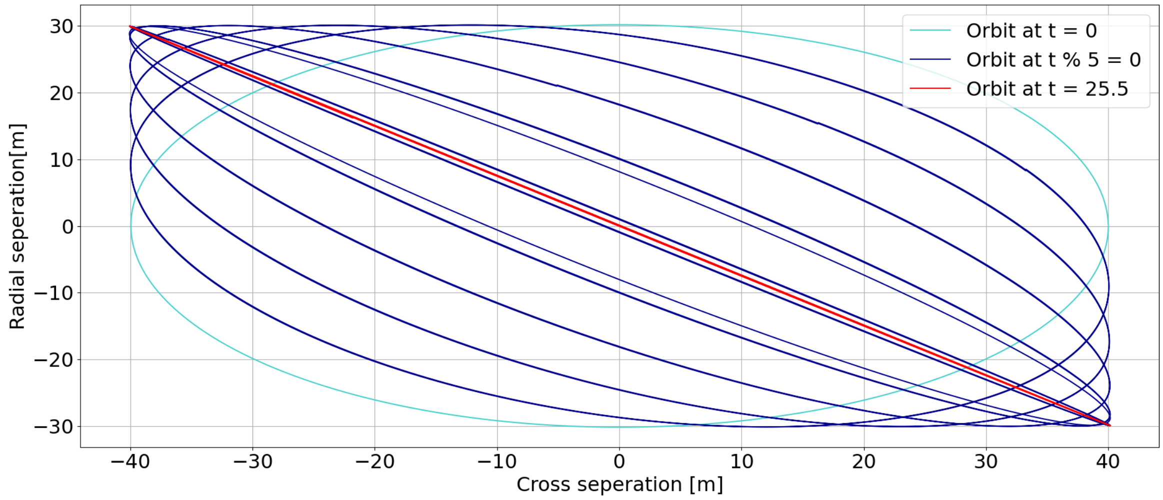

Figure 5.31: Ellipses drawn by TDX around TSX for the ideal test case.

As can be observed from Figure 5.31, the orbits start parallel and therefore trace an elliptical path in the R-N plane. This is as expected, as this is how the states of the spacecrafts were defined. Over the course of propagation, the orbits become orthogonal. The time at which the orbits are close to orthogonal was again found to be equal to $t = 25.5$ days. Now, to perform an analysis of the use of the metric, a risky conjunction needs to be found. Although the alignment between the relative vectors can represent a risky situation due to the presence of a large along-track uncertainty, it is also crucial to take note of the miss distance at a time for which the geometry between the two orbits indicates a safe situation, as mentioned before. Denenberg's algorithm was used to find the time of closest approach. Multiple different close approaches could be found, as can be observed from Figure 5.32. To study the metric, two close approaches were studied, one near the time the relative e/i vectors are anti-parallel, and one near the time they are perpendicular. In both cases, the total miss distance will be small (on the order of 50 meters or less) allowing to assess the ability of the metric to screen for high and low risk conjunctions on the basis of geometry. The setup and evaluation follow a similar procedure as described in Chapter 4, to evaluate the risk metric over a period of several days before TCA. However, in this case the initial state does not need to be backpropagated from TCA since it is determined by the initial conditions of the ideal case. The first close approach studied occurs within the first days of propagation. As can be observed from the figure, the minimal miss distance remains relatively small at this time. Furthermore, the alignment between the vectors will still be close to parallel, so it is of interest to study P_c and $\Delta\gamma$. TCA is chosen approximately six days away from t_0, to ensure that the behavior of the angle separation can be studied for the often used screening length. The close approach will be referred to as TCA$_1$ from now on. The second close approach studied is one of the close approaches near the time of closest orthogonal alignment. This approach will be referred to as TCA$_2$.

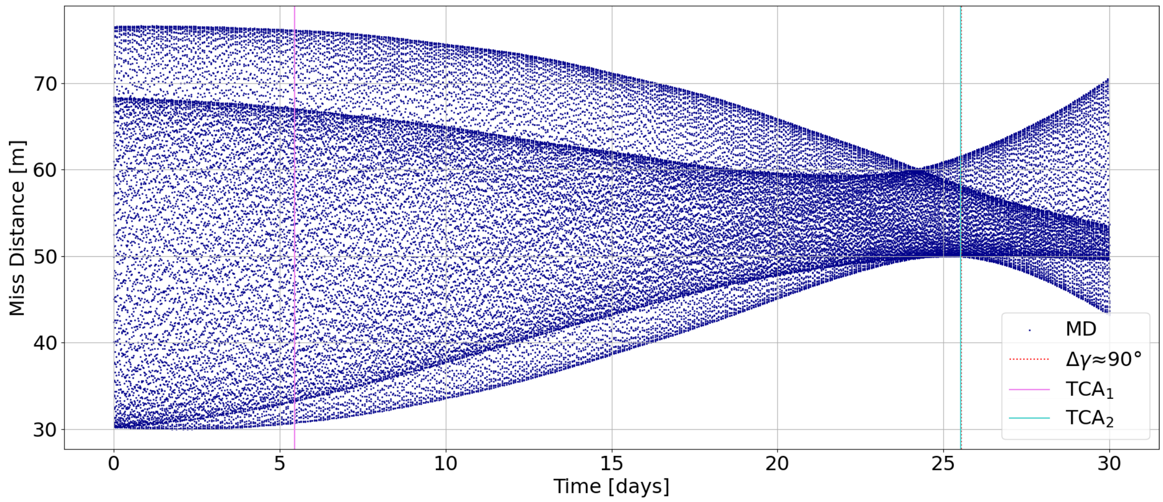

Figure 5.32: Miss distance over the course of propagation for the ideal test case.

The artificial start of the screening period (t_{0_1}) for TCA$_1$ at $t_{TCA_1} = 5.2$ days has been taken equal to 0 days, and t_{0_2} for TCA$_2$ at $t_{TCA_2} = 26$ days has been taken equal to 20 days, to ensure an entire screening period of approximately seven days. For both cases the covariances are estimated at t_{0_1} and t_{0_2} respectively. These covariances have been scaled to represent satellites. This way a scenario in which the available data is sufficiently certain is simulated. From t_0, the states and covariances are then forward propagated to t_{TCA} to observe the behavior of the angle deviation over time. The uncertainty on the angle separation has been determined at every full day and at TCA using a Monte Carlo algorithm. For TCA$_1$, the result is shown in Figure 5.33.

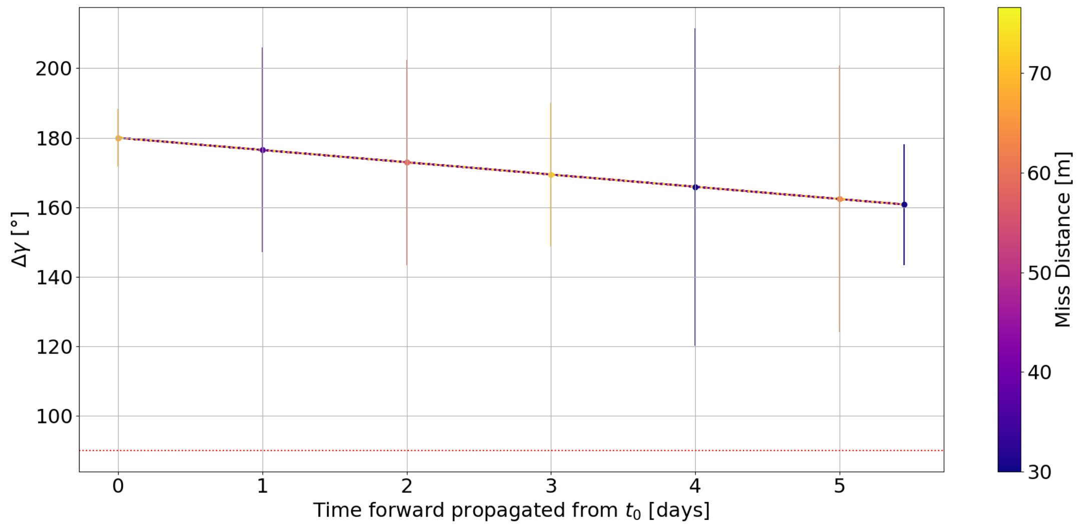

Figure 5.33: Angle separation over time for TCA$_1$, including the uncertainty on the angle on every full day.

As can be seen in the figure, the uncertainty seems to grow and shrink over time, this could be due to the growth pattern that was observed when propagating the covariance as shown in Figure 4.1. Figure 5.33 directly illustrates the difficulty of the interpretation of the metric. Although the angle separation found implies that there is still enough time before the alignment between the relative eccentricity and inclination vectors becomes parallel, the miss distance is equal to 30 m, which is close to the HBR of 21 m. Since the associated joint covariance is small, the probability of collision will be low, as no collision will take place. The relative geometry of the two orbits indicates that there is either a separation in the radial or cross-track direction, and thus, although the along-track direction uncertainty is high, one can say with certainty that part of the separation is in the other two directions. Figure 5.34a shows the magnitude of the joint standard deviations over the course of propagation, whilst Figure 5.34b shows the separations in the different directions. As can be seen, the highest separation is present in the cross-track direction, whilst the uncertainty in this direction is small enough to be sure that this separation is actually there. However, the miss distance in the along-track direction is much less than the uncertainty in that direction, so one must be certain that the secondary object is safely missed in some combination of the radial and cross-track direction.

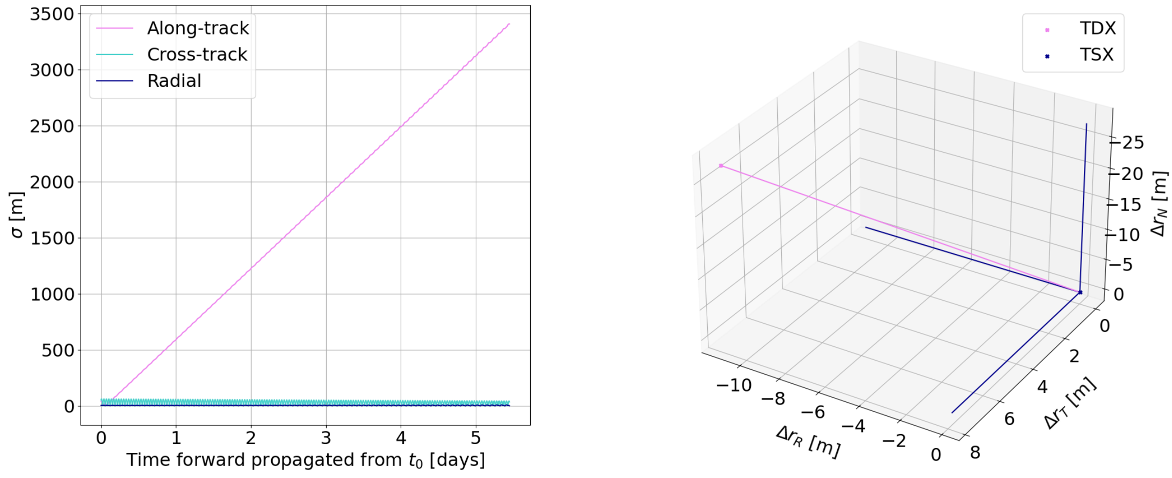

(a) Radial, along-track and cross-track uncertainties over time.

(b) Radial, along-track and cross-track separations.

Figure 5.34: Uncertainty and separations in the RTN frame for TCA_1.

For TCA_2, the same analysis has been done. First, the angle separation over time is studied as shown in Figure 5.35.

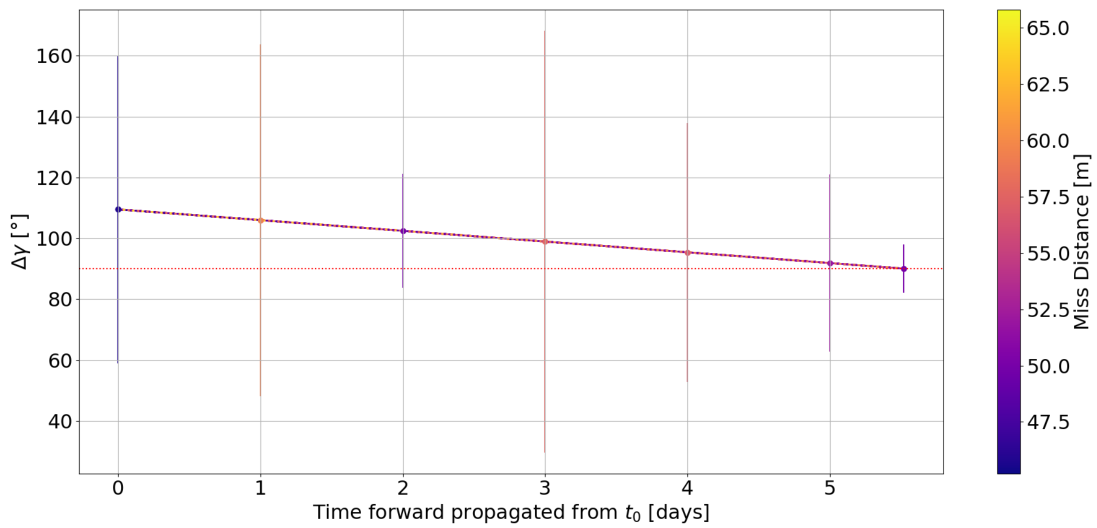

Figure 5.35: Angle separation over time for TCA_2, including the uncertainty on the angle on every full day.

As can be observed from both Figure 5.33 and 5.35, the evolution of the angle separation is stable over time, which is the primary reason for studying this metric. However, it can be noted that the angular uncertainty for TCA_2 at t_{0_2} is initially much larger compared to the initial angular uncertainty for TCA_1. This can be a consequence of how the covariances are scaled. The covariances are scaled such that all individual standard deviations (in ECI), are all at least in the order of 1 m. So the entire covariance is scaled based on the smallest positional standard deviation, as described in Chapter 4. It has been checked whether scaling the covariance based on the uncertainty in the radial direction will lead to different results, but this was not the case. For completeness, the standard deviations after scaling are given in Table 5.6 for both cases.

Table 5.6: Standard deviations of the covariance of TSX after scaling for the two close approaches.

	TCA_1	TCA_2
σ_x	2.79	17.54
σ_R	2.79	8.85
σ_y	24.58	7.74
σ_T	21.61	12.00
σ_z	24.56	2.94
σ_N	27.21	12.40

Again, the magnitudes of the uncertainties in the different RTN directions have been analysed for TCA_2, together with the alignment of the miss distance at TCA_2. The results can be seen in Figures 5.36a and 5.36b.

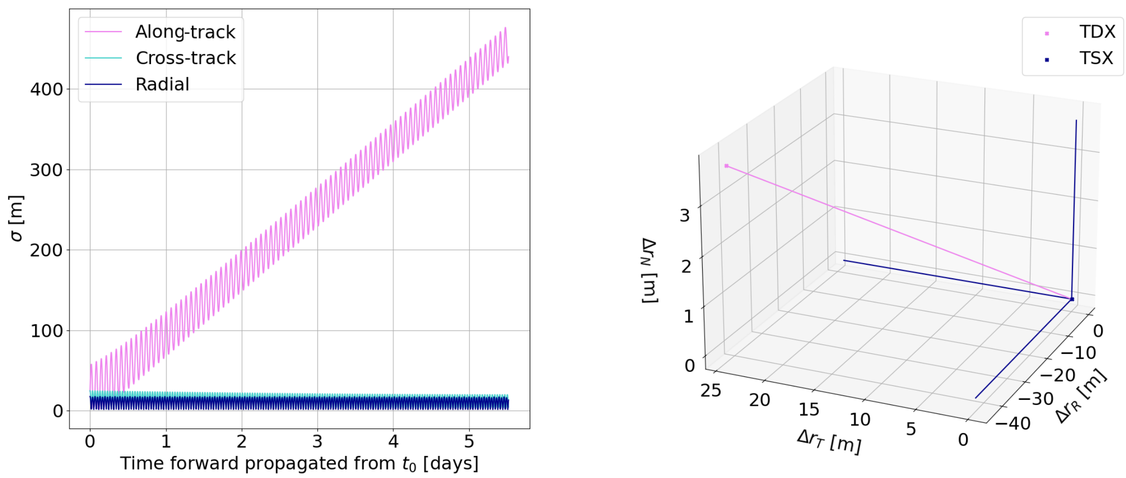

(a) Radial, along-track and cross-track uncertainties over time.

(b) Radial, along-track and cross-track separations.

Figure 5.36: Uncertainty and separations in the RTN frame for TCA_2.

As can be seen in Figure 5.36a, the uncertainty growth is different from the uncertainty growth observed for TCA_1. Although the growth in the along-track direction is still dominant, the increase in size is much lower. This can be explained by the difference in the initial covariance, as indicated in Table 5.6. When assessing the alignment of the miss distances as shown in Figure 5.36b, it can be seen that a large amount of the total miss distance is present in the radial and cross-track directions, this can be explained by the fact that the vector alignment is not exactly orthogonal. The time chosen represents a close approach close to this time. The angle separation does however indicate that a risky situation could occur in which a joint vanishing of Δr_R and Δr_N is reached. In case the entire miss distance, equal to approximately 60 meters, would have been aligned with Δr_T, one could not be certain of a miss as $\sigma_T \approx 400$ m. Although the difference in uncertainties might lead to a misleading analysis of P_c, the probability of collision is calculated using the Hall and Elrod formulations, as also provided on Privateer. The encounter is of low-relative velocity, so the formulation derived by Hall will be considered leading here. The results are shown in Table 5.7.

Table 5.7: Probability of collision for close approaches studied for the ideal testcase.

Metric	TCA_1	TCA_2
$P_{c_{Hall}}$	$2.38 \cdot 10^{-6}$	$1.01 \cdot 10^{-1}$
$P_{c_{Elrod}}$	$1.79 \cdot 10^{-15}$	$6.90 \cdot 10^{-5}$

As can be seen, the probability of collision is higher for TCA_2 compared to that of TCA_1. However, the covariance of the former case was also found to be much higher, and thus it could be the case that the probability is diluted.

5.5.4. Key Takeaways Relative Orbital Parameters Metric

It was hypothesized that, because of the stability of mean orbital elements, the relative orbital parameters metric might be able to indicate the possible occurrence of a risky encounter well before TCA, based on the alignment of the miss distance. However, the use of the metric suffers from multiple drawbacks. Namely, the uncertainty on the angle separation quickly grows due to the uncertainty on the initial states. This is due to the fact that if the vectors sampled (during a Monte Carlo analysis) completely encompass the origin, any angle between the two vectors is possible. The large uncertainties significantly limit the use of the metric. Furthermore, the metric can only be used for bounded orbits, for which $\Delta a \ll 1$. Moreover, the interpretation of the metric is still uncertain, no clear probabilistic safety interpretation has been established that combines both the miss distance, the angle separation and the angular uncertainty. On top of that, an associated safety threshold needs to be available to determine when mitigation actions should be considered. This threshold will depend on the time it takes for a configuration to move from a parallel to an orthogonal alignment, which could be different for different satellite formations. A meaningful use of the metric for conjunction analysis has thus not been established.

5.6. Results Survey on Data Usage in Conjunction Analysis

The survey, developed using Survalyzer, consists of open questions, multiple choice questions, and rankings. All participants have given permission for the use of their responses in the thesis with the assurance that the responses will remain anonymous. The survey consisted of four parts. The first part focused on asking for general information from the operators, such as in which regime and on how many satellites they are operating. Using this information, the different responses can be grouped and the diversity of the responses can be evaluated. To gain insight into the relation between the satellite number and the amount of CDMs that an operator receives, it has been asked how many CDMs are received per month and how many collision avoidance maneuvers are performed per month. The second part consisted of information on whether and how operators use CDMs, which data aspects they consider leading, and what data could be included or excluded. In the third part, the novel risk metrics proposed in this thesis were briefly introduced and it was determined whether the operators would be open to the use of these metrics. Furthermore, it was studied how the operators would prefer to have the results of the metrics presented. Last, general questions were asked to inquire how multiple different risk assessments could be presented to operators. The survey received a total of fourteen responses. Most responses originate from satellite operators, but there are also two responses of SSA providers. These participants provide conjunction assessment services to satellite operators. In total, participants work for eleven distinct organizations.

5.6.1. General Information

Of all satellite operators, 100% (12) is operating in LEO, 8.3% (1) in GEO, 16.7% (2) in HEO, and 8.3% (1) in MEO. The two SSA providers are working with data from satellites in multiple regimes. As a result, it can be concluded that LEO is best represented. Operators can be grouped according to the number of satellites they are operating on. This might be useful, as the approach to conducting conjunction analysis may be very different depending on the number of satellites that need to be managed. This is also mentioned by one of the participants. That is, an operator operating on large constellations might have access to more resources compared to an operator operating on a smaller number of satellites. These might rely more on processed data due to limited available internal resources. The approach of both can thus be very different.

- The first group consists of operators operating on one to nine satellites. There are three participants present in this group, all operating on satellites orbiting in LEO.
- The second group consists of operators who operate on satellite numbers in the interval of $[10,\ 100]$ satellites. Seven participants fall in this category, including one SSA provider. All participants are operating in LEO. One operator additionally operates on satellites in MEO and GEO, and one operator additionally operates in both GEO and MEO. The SSA provider works with satellites in LEO and GEO. From this group, three participants originate from the same organization.
- The last group consists of operators who operate on $100+$ satellites. Four participants fall in this group, again including one SSA provider. The three satellite operators all operating in LEO and the SSA provider works with satellite data from satellites in all regimes.

Due to the relatively small number of participants per group, the answers will primarily be analysed collectively across all three groups. However, when relevant, differences will be highlighted.

The survey includes questions on the number of CDMs received per month and the number of collision avoidance maneuvers performed per month. Due to the small sample sizes per group, no exact relation can be established between these numbers. In general however, the number of CDMs increases significantly with a growing number of satellites, but some unexpected numbers were found in the analysis. For the first group, for example, there are two operators managing two satellites, however the answers given ranged from as few as two CDMs per month to as many as 2500 CDMs per month. A larger number of participants would be necessary to clearly study the relation between these numbers. Across all groups, the maximum number named was equal to one million CDMs per month, and 71.4% (10) of the answers reported values well above one thousand. One operator remarked that the number of CDMs received is just “too many”. These numbers further indicate the need for an effective conjunction analysis. Additionally, participants were asked about the approximate number of collision avoidance maneuvers performed per month. As noted by multiple participants, these numbers might be skewed, due to the fact that maneuvers are often combined with station-keeping maneuvers, for example. The highest number reported was equal to 300 maneuvers per month from an operator part of the third group. Almost half of the participants indicated that fewer than one maneuver is performed per month. For both event counts, a scatter plot has been made to observe the relation between the number of satellites, the number of CDMs, and the number of COLAs. Some numbers are missing, as not all operators were sure about the data. The dashed line implicates which numbers are linked to each other, meaning that the number of CDMs per month and the number of maneuvers per month are originating from the same operator. Some operators mentioned an order of magnitude (e.g. thousands, millions), for these numbers the plot shows the magnitude multiplied by five (5,000 and 5,000,000 respectively). The figure thus merely serves to indicate the overall trend, the numbers should not be considered as complete truth. The results can be seen in Figure 5.37.

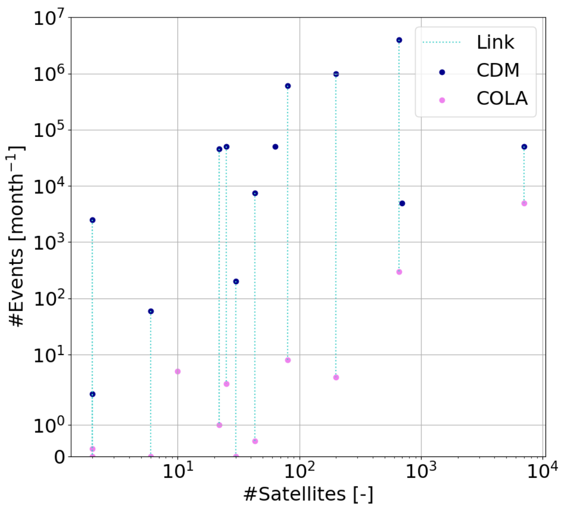

Figure 5.37: Event numbers as a function of the number of satellites.

In general, it can be seen that the higher the number of satellites, the higher the number of CDMs and collision avoidance maneuvers.

All participants use CDM data for their conjunction analysis. Seven out of the fourteen participants use additional data sources. It can be noted that none of these participants were part of the last group.

The different external data sources mentioned are:

- Own orbit information and onboard-based (e.g. GNSS data) or ground-based measurements,
- O/O ephemerides,
- Latest orbit information, such as the covariance and planned maneuvers for satellites,
- Own generated CDMs based on operational orbit screening,

- TLEs to study the history of the objects,
- SP ephemerides for analysis outside of TCA.

The use of O/O ephemeris as additional data source has been mentioned by multiple different operators. This highlights the importance of data sharing between operators.

5.6.2. Perspectives on Conjunction Data Messages

On average, the CDM is deemed effective, receiving an overall rating of 7.8 out of 10. The extent to which participants take a certain mitigation action as a result of CDM data is indicated in Figure 5.38.

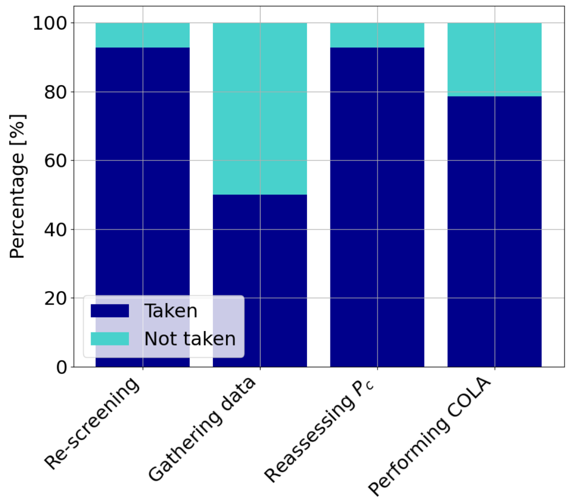

Figure 5.38: Actions taken based on CDM data.

As can be seen, thirteen participants re-screen the conjunction using O/O ephemeris and reassess the probability of collision. It must be noted, that previously, only half of the participants mentioned that extra data is used. This could be due to how the question is posed. That is, the question was open rather than multiple choice, so for operators, it was not clear what data constituted as extra data. It could be the case, that operators consider their own data not as extra data. All but three operator perform collision avoidance maneuvers based on CDM data, and seven participants also gather refined tracking data of the objects. An open question was used to understand how the operators use the CDMs to determine whether an action needs to be taken. Multiple different processes have been named. Often, the processes consist of re-screening the conjunction with data from the own satellites of the operators and deputy information either obtained from:

- CDMs,
- O/O ephemerides,
- (Additional) ground based measurements (conjunctions that are very risky or uncertain are given priority),
- Assessed size from ESA's DISCOS database.

This was also indicated in Figure 5.38. One operator mentioned that the process of making an action decision is automatic, except for the decision to perform a collision avoidance maneuver. For this, human involvement is needed. Another participant mentioned that the decision to perform a collision avoidance maneuver also depends on the opposing party and their capabilities. Apparently, some operators will always maneuver. Other third parties are difficult to reach. If the event is of high risk, the risk will then need to be mitigated. One of the SSA provides replied that multiple CDMs are used to perform comparative SSA. Some participants state that they have dedicated guidelines to determine when to take a certain action decision. These action decisions are then mostly based on the aspects given in Figures 5.39a, 5.39b, 5.39c and 5.39d, which shows the leading aspects of the CDMs on which a decision action is based. It must be noted that previously it was found that only eleven out of fourteen participants (78.6%) perform a collision avoidance maneuver based on the CDM. However, when determining which aspect is considered leading in a decision to perform a maneuver, all participants replied as can be seen in Figure 5.39c. An additional action performed by one of the operators is to assess the effectiveness of a collision avoidance maneuver. Furthermore, the operator mentioned that it is studied whether the maneuver will not cause new conjunctions.

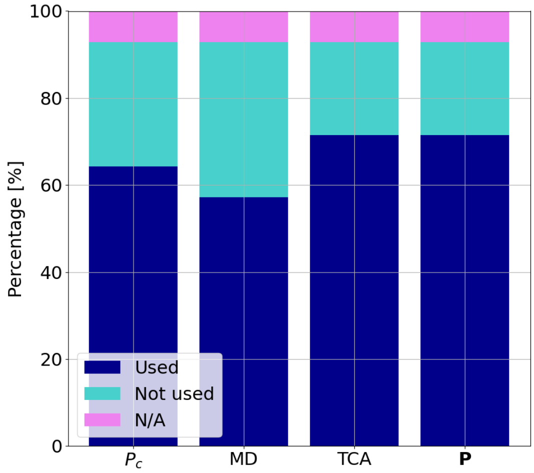

(a) Re-screening the conjunction with owner/operator ephemeris.

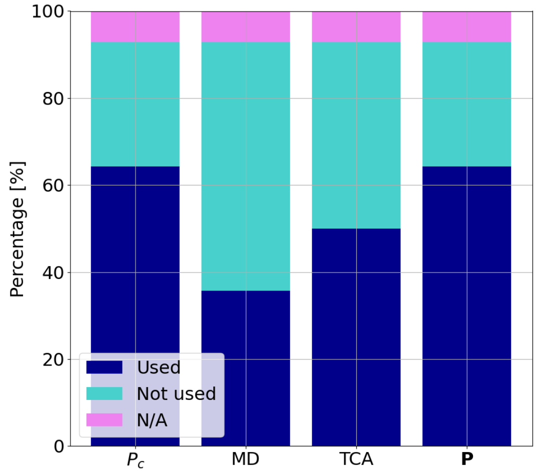

(b) Reassessing the collision probability

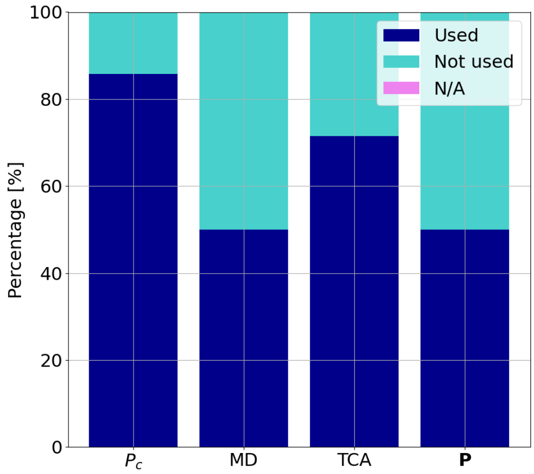

(c) Executing a collision avoidance maneuver

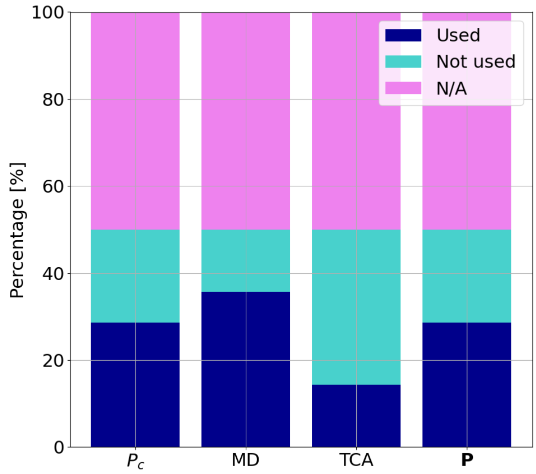

(d) Gathering refined tracking data of the objects.

Figure 5.39: Leading aspects in the decision to mitigate a collision risk, Multiple aspects could be selected.

Apart from the data present in the CDM, some other aspects are studied as well for the decision to mitigate the collision risk. For example, the update frequency of the deputy data is used. This update frequency might be used to determine the reliability of the deputy data. Additionally, the separations in the radial, along-track and cross-track directions are studied. This could be due to the reasons discussed in Chapter 3, that is, the uncertainty in the along-track direction is often more significant than the uncertainties in the radial or cross-track directions. Hence, if the miss distance is completely aligned in the along-track direction, a potential risky conjunction could occur.

The next three questions were focused on the limitations and possible extensions of CDMs. The perspectives on the limitations seem to be consistent among all participants. The foremost mentioned limitations are related to the covariance, particularly its often large size, lack of realism, and the tendency for it to be overly optimistic. Although these limitations are related to the covariance, some are conflicting. An overly optimistic covariance namely implies that the covariance is smaller than it is in reality. However, often the large covariance size is named as limitation. It could be the case that even if the covariance is too optimistic, it is still too large. Concerns were also raised about the covariance quality and the missing information on how the covariances were established. Moreover, the lack of information available on the orbit determination process in general and the effect of unknown low-thrust maneuvers on this are mentioned. To stay on the topic of maneuvers, many participants mentioned that the lack of knowledge one has about the (planned) maneuvers of other parties complicates the CA process. Third parties do not always share their maneuver data, and there is a lack of coordination on this. Commonly, it is unclear who should maneuver, and there is a lack of transparency regarding the typical actions and protocols followed by the other party. In general, a standard procedure used between different operators could help. Kerr et al. also recommended that an experienced space lawyer should review regulations on this [48]. A need for general space traffic management coordination has also been acknowledged by both Europe and the US [13]. Currently, the United States Traffic Coordination System for Space (TraCSS) and EUSST are both working on services for SSA. This is thus an active field of research. Participants of the survey also named the disagreement between different data sources and metrics as limitation, together with the missing HBR information. The last topic named is the update frequency of CDMs. The update frequency is often unknown, and the data changes within updates is significant.

Operators named multiple different aspects that they believe would be helpful to include in CDMs. Before discussing this, it is noteworthy that the format of the CDM is revised and reviewed every five years. Many inputs have already been gathered for this and the window in which new adjustments can be suggested is essentially closed, as mentioned by one of the participants. Nevertheless, the proposed aspects are briefly listed here.

- An indication of when the next CDM update becomes available or the expected time this update will take.
- Recommended maneuvers or maneuver coordination information, which is contrary to the result found by Kerr et al. [48].
- Information on how the orbit determination process has been performed and the quality thereof, or which sensor locations have been used to obtain the measurements.
- A warning when the large uncertainty might lead to misleading or diluted probabilities.
- Reliability of the covariance provided by O/Os.
- The HBR used.
- Coordinate transformation quaternions between inertial and fixed frames.
- A trend of the behavior of P_c from previous assessments.
- A link to a visualization of a 3D trend of the objects' orbits.

Only one of the participants considered the CDMs to include too much information. It is mentioned that the units and other pre-specified data provided in the CDMs could be excluded. Another operator mentioned that although the CDM does not include too much information, it includes the wrong information. The participant mentioned that the information could be overwhelming, when for example P_c is misunderstood.

5.6.3. Data Structure for Proposed Novel Risk Metrics

After the proposed metrics were briefly introduced, operators were asked whether they would be open to the use of these metrics. It must be noted that multiple operators mentioned the short introduction was not completely sufficient to give a definite answer. First, the relative orbital parameters metric is discussed. Only six out of fourteen operators state that they would consider using this metric. The follow up question was how operators would want this metric to be presented to them. The results from this question did not only provide useful insights for this presentation, but also offered valuable perspectives on the perceived usefulness of the metric from the operators' point of view. First, the presentation is discussed. If the metric would be used, at least the associated confidence interval should be presented. Two operators would then prefer the worst-case scenario angle at TCA (angle closest to an orthogonal alignment within the interval), and two would prefer the expected angle at TCA. Second, the use of the metric is discussed. Most participants considered the metric as more suitable for filtering or pre-screening of the entire catalog, rather than as a risk assessment metric for a specific event. The participants also state that this is due to the fact that the metric does not have a clear safety related conclusion, which also became apparent when analysing the metric (Section 5.5.1). Furthermore, an associated safety threshold is hard to establish, as also discussed by one of the participants. Another operator concludes that the metric would only be suitable for long-term continual encounters, which is true as the assumption $\Delta\vec{x}_K \ll 1$ should hold. That is also why the metric was deemed more suitable for formation-flying satellites, but this is of course a limitation of the metric, and might further complicate its use. Last, it has been noted that 3D geometry calculations and information are often already used based on the information presented in the CDM.

The outer probability measure metric was considered for use by ten out of the fourteen participants (one participant commented maybe). The desired presentation of the OPMs is often described as something resembling a visual scale, or a field indicating whether P_c is acceptable, unacceptable or undermined. Others would prefer to be presented just the upper and lower boundary, such that the operators can set their own safety threshold. It is mentioned that the metric could be useful for sorting conjunction events based on whether they are irrelevant, whether a maneuver should be performed or whether one should wait for more data. Different cases could then be prioritized. Furthermore, it is noted that, although the metric could be included in the CDM, the methods used for its calculation should be specified transparently and the results should be replicable. One participant namely mentioned that P_c as presented in the CDM is often replicated, instead of directly used. Furthermore, the way an operator should interpret the result of a metric should be clear, this would enhance its reliability and make communication with other operators more effective, as noted by participants. A few operators have noted that established methods of mitigating the dilution region already exist, such as $P_{c_{max}}$.

5.6.4. Data Structure for Various Risk Metrics

This section set out to determine how data should be structured if multiple different risk metrics are used, such as both P_c formulations and OPMs for example. The CDMs as provided by Privateer already include two formulations of the probability of collision, as mentioned before. However, although the formulations are different and have their own assumptions and associated drawbacks, the interpretation of the both is similar. To the contrary, when presenting both the results of P_c and U_c, the metrics can result in very different conclusions. The first question of this section explored whether participants would prefer to see the results of all hypothetically tested risk assessment metrics, or only the one indicating the highest collision risk. All participants agreed that all risk metrics should be presented, instead of only the metric representing the highest risk, except one, who replied with "Not Applicable".

The participants were asked to provide suggestions for the data structure when using multiple different metrics. One important result was that the data should at least be parsable. The following data structures were suggested:

- Present all different metrics, in a comparative method, but highlight the one that is most suitable for the specific event.
- Apply weighting factors on the metrics depending on the reliability of the metric for the specific event.
- Present all different metrics, but synthesize a global metric to get an idea of the total risk.
- Present all metrics including the context of the metric. Strong differences in the decision to mitigate per metric for a specific event should be explainable.

Notes made are again that all information should be shared transparently. Some operators have mentioned that they do not use raw metrics of CDMs at all. They always calculate the metrics internally, and review all of these calculated metrics. A metric that cannot be replicated will thus not be used. Furthermore, it was determined whether participants want the data to be presented quantitatively or qualitatively, it was noted that all participants, but one who replied "N/A", want the metrics to be presented to them quantitatively. It is also noted that, for OPMs for example, it might help to include both the quantitative boundaries together with the qualitative conclusion that can be made from these boundaries. Last, it was asked whether participants want an action advice. Eight out of all participants want an action advice.

5.6.5. Key Takeaways Survey on Data Usage in Conjunction Analysis

From the survey, it can be concluded that operators are in general content with the CDM, but the CDM could benefit from improvements on the covariance realism, size and quality. Furthermore, operators would benefit from having an indication of how long it will take to the next CDM update. When using multiple different data sources, all risk metrics should be presented to operators. Furthermore, the method of assessing the risk using a certain metric should be transparent and reproducible. There is a general interest to receive information on the reliability of risk assessment metrics, the covariance and the orbit determination process used. This reliability could be used to generate weights for the different metrics to create a global risk assessment.

6

Conclusions and Recommendations

6.1. Conclusions and Discussion

This thesis set out to explore whether a meaningful contribution could be made to expand or improve conjunction analysis. The objective of the thesis was to study whether novel risk assessment metrics could complement currently used methods, to both improve the accuracy of the collision risk assessment and the timeliness in which the risk becomes apparent. The goal was to both explore the theoretical application of the metrics and to adhere to the operational needs of satellite operators. The research aimed to answer the following question:

"How can the conjunction analysis as currently used be further expanded or improved?".

To address this question, multiple sub-questions were posed. The answers to these questions are provided and discussed below.

Question 1: "How can the performance of existing CA methods be improved via the incorporation and combination of novel risk assessment methods?". To answer this question, the risk metrics currently used in conjunction analysis and implemented in NASA CARA's SDK have been evaluated on various test cases, where known limitations of these metrics have been verified. That is, the dilution effect has been observed for large joint covariances, and it was found that the 2D P_c formulation was only valid for high-relative velocity encounters. For low-relative velocity conjunctions a Monte Carlo analysis can be used, however, its computational inefficiency is a significant drawback. Although this limitation weighs against the effect of using the 2D P_c formulation, which relies on assumptions that do not hold low-velocity encounters, Hall pointed out that for high-fidelity analysis, the use of a Monte Carlo algorithm may become prohibitive [37]. The P_c formulation derived by Hall [37] can be used for the low-relative velocity cases, as it provides an upper boundary on the probability of collision. In addition to these expected outcomes, it was found that the maximum P_c metric does not always mitigate the dilution effect completely for large joint covariances, highlighting the need for a more rigorous metric.

One of the metrics selected for implementation is the outer probability measures metric as developed by Delande et al. [21]. Outer probability measures distinguish random from systematic errors. The metric was selected due to its potential to reliably mitigate the dilution effect, without the need of historical data (WSPRT), experience (scaled P_c), or a large enough grid of scale factors applied to the covariance ($P_{c_{max}}$). Furthermore, the metric does not only provide an estimate of whether the situation is risky or not, but also evaluates whether the available data of the conjunction is sufficient to quantify the collision risk. Specifically, the upper and lower boundaries on the probability can be used, together with a safety threshold, to qualify the risk as safe, undetermined or unacceptable. If both boundaries are entirely below or above the threshold, the risk is qualified as safe or unacceptable respectively. If the safety threshold is in between the two boundaries, the risk is undetermined, and hence, additional data is required. The metric was also evaluated on the various test cases. It was found that the metric can correctly mitigate the dilution effect, even in cases where $P_{c_{max}}$ did not. Furthermore, it was observed that, if the information available on the states is correct (so no mismodelling was applied), no false negatives occur. Thus, for all risky conjunctions, the metric correctly identified the risk as unacceptable or undetermined. For mismodelled cases, random noise should be added to the propagation of the covariance, to ensure that the certainty on the states is not overestimated. The metric was able to reliable mitigate the dilution effect, however, the number of false positives did swiftly increase. Specifically, cases for which the conjunction was safe, but the covariance was large, were identified as risky, due to the conservative nature of the metric.

The other metric implemented is the relative orbital parameters metric. The concept of relative orbital parameters is currently already used for the formation control of TerraSAR-X and TanDEM-X [19]. It was expected that the metric could provide valuable information on the conjunction, specifically on the direction along which the miss distance is aligned. Furthermore, the metric is stable over time, which will be discussed in more detail in Question 2. The miss distance direction is found using the relative geometry between two orbits. That is, it has been proven that in the absence of a drift in Δa, an orthogonal alignment of the relative eccentricity and inclination vectors can lead to a joint vanishing of the separations in the radial and cross-track directions. Due to the high uncertainty in the along-track direction, the miss distance in the radial and cross-track directions should never vanish together. If this does occur, the situation is risky. Apart from the advantage of the stability of the metric, another expected advantage was that the uncertainties in the initial Cartesian states were expected to provide a small uncertainty in the angle between $\Delta\vec{i}$ and $\Delta\vec{e}$. However, the contrary proved true. Namely, when employing a Monte Carlo algorithm to find the angular uncertainty, it was found that for a small magnitude of the vectors $\Delta\vec{i}$ and $\Delta\vec{e}$, the sampled vectors will quickly encompass the origin. This implies that any angle between the two vectors can occur, leading to a large angular uncertainty. Although the uncertainty magnitude for which the origin is entirely encompassed by the sampled vectors depends on the magnitudes of the initial vectors $\Delta\vec{i}$ and $\Delta\vec{e}$, in general $\Delta\vec{x}_K \ll 1$ must hold for the metric to be employed. Thus, the expectation is that for most cases, the uncertainty on the initial states needs to be very small in order for the uncertainty on the angle to be small enough for the metric to be meaningful. This small initial uncertainty can often not be accomplished through ground-based measurements. Apart from this drawback, the interpretation of the metric proved complicated. First of all, there should be no drift in Δa, as mentioned before. Furthermore, the miss distance should be taken into account as well. That is, if the miss distance is aligned in the radial and cross-track direction, but is smaller than the HBR, the situation is still risky. No clear safety threshold has thus been established. So, although the relative eccentricity and inclination vectors seemed useful, the metric does not appear to be suitable for the risk analysis of a specific event, given the accuracy of the currently available data.

Question 2: "Is it possible to extend the risk analysis time horizon, in order to enable reliable decision making further in advance of the potential collision?". As briefly mentioned above, it has been hypothesized that the relative orbital parameters metric could be used not only to expand conjunction analysis, but also to enhance the time horizon available for decision making. Namely, as the metric uses mean orbital elements to determine the alignment of the miss distance, the metric was hypothesized to provide a more stable solution when assessing the collision risk several days before TCA. The angle behavior over time is namely stable, whilst the separations in the spatial dimensions x, y and z vary more rapidly over different updates. Although the angle proved stable over time for the TerraSAR-X and TanDEM-X conjunction, the angular uncertainty discussed above is too large to use the alignment between $\Delta\vec{i}$ and $\Delta\vec{e}$ in a meaningful way. Again, although this was only tested for the specific TerraSAR-X and TanDEM-X conjunction, it is expected that this will hold true for all cases for which the metric is applicable. This should be further verified in future research. So, although the angle behavior is stable over time, and could thus be used to predict the alignment of the miss distance forward, the uncertainty on the angle was found to be too large for the test case used in this research.

Apart from the relative orbital parameters metric employed to extend the time horizon available for decision making, some insights in the time availability have been found during the analysis of other (existing) metrics. Namely, upon analysis of the current methods used for conjunction analysis, specifically analysis of vanilla P_c, it was found that when using mismodelled dynamics to propagate the states of the potentially colliding objects, these states will drift from their actual trajectories. The longer these states are propagated with an inaccurate model, the larger this drift will be. This also has an effect on the time horizon available for decision making. Namely, when a collision will occur, but the states are propagated with an incorrect dynamical model, the states will have drifted far from their actual miss distance when assessing the risk far before TCA, due to the long propagation time. Then, the closer to TCA, the shorter the propagation time, and thus the smaller the drift from the actual trajectories. The risk will thus become apparent only shortly before TCA. Hence, mismodelling has an effect on the time horizon available for decision making, and again, the certainty on the states should not be overestimated.

Furthermore, it was found that in some cases the results of the OPM metric seemed to be more stable over time compared to the results of P_c and $P_{c_{max}}$. This could be due to the fact that far before TCA, the covariance is relatively large, and thus the credibility will be large due to the large covariance. To the contrary, P_c will be low due to the dilution effect. However, it was also found that this is not always the case, as sometimes the credibility was larger for a smaller covariance. This behavior is unexpected, and due to this reason, it cannot be verified with certainty that the metric could be used to enhance the time horizon of decision making. However, this could be analysed in future research.

Question 3: "How can the new methods be synthesized to produce useful output for operators?". To address this research question, a survey was conducted to gather insights and perspectives from satellite operators. Satellite operators are considered the end-users of risk metrics as they are responsible for the decision to mitigate a collision risk, thus, their opinions on the data output are considered leading to address this question. The survey was very valuable for the analysis, however, interpreting the various qualitative answers of different operators proved challenging. Nevertheless, key takeaways could be identified across the different responses. The research question focuses mainly on how the newly proposed metrics could be presented to operators. It is also valuable to discuss the operators' perspectives on how to structure conjunction data in general, in case potential future extensions of the research identify other promising metrics.

For the metric specific presentations, it was found that OPMs should be presented both quantitatively, i.e. the upper and (still theoretical) lower boundary should be presented, and qualitatively, i.e. the categorization of the collision risk as either safe, undetermined or unacceptable should be indicated. As the interpretation of the metric is different from the conclusions drawn from vanilla P_c, this should be clearly stated to operators. The relative orbital parameters metric was deemed less suitable for conjunction analysis, due to previously named reasons. In case such a metric would be used, the presentation should consist of the expected or worst-case scenario angle, including the confidence interval associated to it.

In general, when using multiple different risk metrics, all metrics should be presented quantitatively. For some specific metrics, an additional qualitative presentation could be valuable. Operators would benefit from an estimate of the reliability of each metric, and an additional global risk could be presented by selecting the most appropriate metric for the specific event or by adding weights to the different metrics depending on their reliability. A measure of the reliability of metrics should thus be investigated. The most important takeaway of the survey was that the metrics used should always be communicated transparently and the results should be replicable, to further enhance their reliability.

Main Question: The answer to the main research question is that current conjunction analysis can be improved using novel risk assessment metrics. Many different statistical representations of the collision risk have already been derived, including $P_{c_{max}}$, all with their different advantages and disadvantages as outlined by Hejduk et al. [42]. The OPM metric as derived by Delande at al. [21] would be a good addition to this list, due to its reliability in mitigating the dilution effect. Furthermore, it has been found that one should never overestimate the certainty on the information available, as mismodelling can lead to a wrong identification of the event and this should thus be compensated for using process noise. The time horizon in which satellite operators need to make a decision is still a subject of interest, as no clear solution has been identified to extend the time horizon available for decision making. Furthermore, a lot can be gained from the information and perspectives available from satellite operators. They have very clear views and hands on experience on the current challenges and opportunities of conjunction analysis, and thus the operational application of novel risk metrics. This could also be concluded from the research conducted by Kerr et al. [48]. It would thus be very valuable to keep operators, together with SSA providers and method developers, in the loop when extending research on how conjunction analysis could be further improved.

6.2. Recommendations

Drawing from the insights gained in this study, a series of recommendations are proposed for further research on conjunction analysis. First, findings from the survey indicate that satellite operators consider the often unrealistic covariance as problematic for conjunction analysis. The large size is named, together with the often too optimistic presentation. As was found, an overestimation of the certainty on states can lead to problems when one uses an incorrect dynamical model, but noise could compensate for this issue. For this research, the drag acceleration was mismodelled on purpose, so the size of the matrix $\mathbf{Q}$ could be established relatively easily. In reality, unless one deliberately chooses to propagate the states with a low-fidelity dynamical model, for efficiency for example, it may be difficult to determine the correct size of this matrix. This should be further investigated. Furthermore, a consequence of adding noise to the propagation, to address the former limitation, is that the covariance size will be even larger, as was already a problem implied by the latter limitation. How to achieve a balance between these two drawbacks would be an interesting topic for research. Moreover, the covariance for this research has been propagated using a linear method. The linearization error has been established to get an idea of the error this induces, however, for further research it is recommended that the method of propagating the covariance is further analysed. A method that is both accurate and efficient should be established, which could help in the reliability of the simulated conjunction. Then, the actual covariance will be non-Gaussian after propagating with a nonlinear dynamical model. This should be accounted for when determining P_c.

Another takeaway from the survey was that operators wish to gain insights into the reliability of risk assessment metrics. Furthermore, a desire to receive an indication of the covariance quality and quality of the orbit determination process were mentioned. The quality or reliability of methods used in conjunction analysis in general thus seems to be a recurrent topic of interest. For a low-relative velocity for example, it is known that the 2D P_c formulations will not be accurate due to their assumptions. However, in the CDM as given by Privateer the 2D Elrod probability is still provided for TSX/TDX conjunctions. It would be interesting if a weight or reliability could then be added to this metric, as suggested by operators. To get an idea of the reliability of the metrics, or to learn which metrics would be best suitable for a certain event, methods such as Copolla's bounds could be applied [18]. The Copolla bounds can be used to determine whether an event is of low-relative velocity. This way it can be addressed which formulation of P_c needs to be used. This study is already implemented in NASA CARA's SDK and can be taken as an example for the development of similar methods to determine which risk assessment metrics would be best suitable for a certain encounter. The reliability of the metrics then depends on the encounter at hand.

Furthermore, the time horizon, in which reliable decision making is possible, has not been enhanced. As the decision to perform a collision avoidance maneuver is critical, and it would be best if the maneuver can be performed together with a station-keeping maneuver for example, the improvement of the time horizon is still considered to be an important topic for further research. Although the relative e/i vector formulation could not provide a meaningful solution, other metrics such as the distance metrics briefly discussed may be utilized. As explained, the miss distance is currently calculated in Cartesian elements, but orbital element representations have been proposed [80] which could be useful for conjunction analysis. Due to the use of orbital elements, the result might be more reliable, although the uncertainty on the distance should be considered well, as the uncertainty on the angle separation proved to be a significant drawback. Furthermore, the distance metrics as proposed by Vananti et al. are derived for the application of tracklet linking. For conjunction analysis, the formulation should thus be altered to only take into account a linking of the position vector, instead of the whole state vector. Furthermore, in Reference [2] another metric using orbital element differences has been proposed. The representation presented in this paper requires fewer assumptions than the relative eccentricity and inclination vectors. This could thus also be investigated. Moreover, as already studied by ESA, machine learning might also be utilized to enhance the time horizon. Machine learning was considered out of scope for this research, but operators have mentioned the use of this for conjunction analysis [48]. So the study of machine learning is recommended for further research. Furthermore, other improvements in conjunction analysis that were not selected for investigation could be studied to improve the accuracy of risk assessments, such as the inclusion of attitude information.

In addition, as identified during this research, another potential application of credibility is that the difference between U_c and P_c might be used to determine which objects should be prioritized for additional data retrieval. Namely, the difference between the upper and lower boundary, $U_c - L_c$, represents the knowledge an observer is missing. The probability of collision, P_c, lies somewhere in between these two boundaries. The smaller the ignorance, the closer the boundaries are together. Although the lower boundary has not been derived yet, the difference between the credibility and probability $U_c - P_c$ could already indicate how large the amount of missing information is. Based on this, additional data retrieval might be prioritized. The outer probability measure metric might thus additionally be used as sensor tasking metric. In Reference [39] it was found that NASA CARA is currently also investigating this. The topic is thus relevant for future research.

Also, the coordination between different satellite operators on when and how to maneuver could be further improved, as suggested by multiple participants of the survey. Kerr et al. also addressed this point by recommending the review of regulations by an experienced space lawyer [48]. This recommendation is further endorsed, together with a recommendation to study how this cooperation could be established. This topic is part of the STM research area. In general, as already mentioned when answering the main research question, the insights of operators proved very valuable for this study. The operators were able to present problems and ideas arising in reality. So, a general advice would be to extend to conversation with operators, but also with SSA providers and developers.

Finally, this research has also left a couple of questions unanswered. Namely, according to the implementation of $P_{c_{max}}$ in SDK, the dilution effect should be completely mitigated, as the algorithm runs until convergence. It was however found that this is not always the case. The reason as to why $P_{c_{max}}$ does not always mitigate the dilution effect is thus not found yet. This should be investigated in more detail, as the metric is already used in practice. Furthermore, in some cases, the credibility appeared to be lower for a smaller covariance, which is unexpected. Why this phenomenon occurs, should also be thoroughly investigated, especially if the metric were to become operational as either a risk assessment metric or a sensor tasking metric. Thus, to get a complete grasp of the theory, both of these questions should be answered. Moreover, the uncertainty transformation from the initial CDM uncertainty to the angular uncertainty, has now only been tested for one test case. To be complete and thorough, various other test cases should be assessed, as discussed before.

References

[1] 18th & 19th Space Defense Squadron. *SPACEFLIGHT SAFETY HANDBOOK FOR SATELLITE OPERATORS*. 2023.

[2] Aguilar-Marsillach, D. and Holzinger, M. J. "Passively Safe Spacecraft Motion Using Reachable Sets and Orbital Element Differences". In: *Journal of Spacecraft and Rockets* 60.5 (2023), pp. 1597–1613.

[3] Akella, M. R. and Alfriend, K. T. "Probability of Collision Between Space Objects". In: *Journal of Guidance, Control, and Dynamics* 23.5 (2000), pp. 769–772.

[4] Alfano, S. "Determining Satellite Close Approached-Part II". In: *ADVANCES IN THE ASTRONAUTICAL SCIENCES* 87 (1994), pp. 233–233.

[5] Alfano, S. "A Numerical Implementation of Spherical Object Collision Probability". In: *The Journal of the Astronautical Sciences* 53 (2005), pp. 103–109.

[6] Alfano, S. "Relating Position Uncertainty to Maximum Conjunction Probability". In: *The Journal of the Astronautical Sciences* 53 (2005), pp. 193–205.

[7] Alfano, S. "Review of Conjunction Probability Methods for Short-term Encounters". In: *Advances in the Astronautical Sciences* 127.1 (2007), p. 719.

[8] Alfano, S. "Eliminating Assumptions Regarding Satellite Conjunction Analysis". In: *The Journal of the Astronautical Sciences* 59.4 (2012), pp. 676–705.

[9] Alfano, S. "Satellite Conjunction Monte Carlo Analysis". In: *Adv. Astronaut Sci* 134 (2009), pp. 2007–2024.

[10] Alfriend, K. T., Akella, M. R., Frisbee, J., Foster, J. L., Lee, D., and Wilkins, M. "Probability of Collision Error Analysis". In: *Space Debris* 1 (1999), pp. 21–35.

[11] Ardaens, J. S., D'amico, S., Kazeminejad, B., Montenbruck, O., and Gill, E. "Spaceborne Autonomous and Ground Based Relative Orbit Control for the TerraSAR-X/TanDEM-X Formation". In: *Proceedings of the 20th International Symposium on Space Flight Dynamics* (2007).

[12] Balch, M. S., Martin, R., and Ferson, S. "Satellite conjunction analysis and the false confidence theorem". In: *Proceedings of the Royal Society A* 475.2227 (2019), p. 20180565.

[13] Borowitz, M., Pérez Hernández, C., Hejduk, M., Gillet, A., Moury, M., and Faucher, P. "Comparison of European Union Space Surveillance and Tracking and TraCSS". In: *75th International Astronautical Congress (IAC)* (2024).

[14] Cai, H., Hussein, I., and Jah, M. "Possibilistic admissible region using outer probability measure theory". In: *Acta Astronautica* 177 (2020), pp. 246–257.

[15] Carpenter, J. R. and Markley, F. L. "Wald Sequential Probability Ratio Test for Space Object Conjunction Assessment". In: *Journal of Guidance, Control, and Dynamics* 37.5 (2014), pp. 1385–1396.

[16] Carpenter, J. R. "Non-Parametric Collision Probability for Low-Velocity Encounters". In: *2007 AAS/AIAA Space Flight Mechanics Meeting* No. AAS-07-201 (2007).

[17] CCSDS. "CONJUNCTION DATA MESSAGE RECOMMENDED STANDARD". 2013.

[18] Coppola, V. "Evaluating the Short Encounter Assumption of the Probability of Collision Formula". 2012.

[19] D'Amico, S. and Montenbruck, O. "Proximity Operations of Formation-Flying Spacecraft Using an Eccentricity/Inclination Vector Separation". In: *Journal of Guidance, Control, and Dynamics* 29.3 (2006), pp. 554–563.

[20] Delande, E., Houssineau, J., and Jah, M. "Physics and Human-Based Information Fusion for Improved Resident Space Object Tracking". In: *Advances in Space Research* 62.7 (2018), pp. 1800–1812.

[21] Delande, E. D., Jones, B. A., and Jah, M. K. "Exploring an Alternative Approach to the Assessment of Collision Risk". In: *Journal of Guidance, Control, and Dynamics* 46.3 (2023), pp. 467–482.

[22] Denenberg, E. “Satellite Closest Approach Calculation Through Chebyshev Proxy Polynomials”. In: *Acta Astronautica* 170 (May 2020), pp. 55–65.

[23] Denenberg, E. and Gurfil, P. “Improvements to Time of Closest Approach Calculation”. In: *Journal of Guidance, Control, and Dynamics* 39.9 (2016), pp. 1967–1979.

[24] Elrod, C., Stamey, J. D., and Hejduk, M. D. *Computational Bayesian Methods Applied to Complex Problems in Bio and Astro Statistics*. 2019.

[25] ESA. *clearspace-1*. Apr. 2024. URL: `https://www.esa.int/Space_Safety/ClearSpace-1` (visited on 09/08/2024).

[26] ESA. “ESA Space Environment Report 2024”. July 2024.

[27] ESA. *About space debris*. URL: `https://www.esa.int/Space_Safety/Space_Debris/About_space_debris` (visited on 02/06/2024).

[28] ESA. *ESA’s Zero Debris approach*. URL: `https://www.esa.int/Space_Safety/Clean_Space/ESA_s_Zero_Debris_approach` (visited on 10/01/2024).

[29] ESA Space Debris Mitigation WG. “ESA Space Debris Mitigation Requirements”. 2023.

[30] ESA Space Debris Office. “ESA’S ANNUAL SPACE ENVIRONMENT REPORT”. 2024.

[31] European Commision. *EU Space Surveillance and Tracking*. URL: `https://defence-industry-space.ec.europa.eu/eu-space/ssa-europes-eyes-space/eu-space-surveillance-and-tracking_en#:~:text=What%20is%20EU%20SST%3F,objects%20that%20orbit%20the%20Earth.` (visited on 07/20/2024).

[32] Foster, J. L. and Estes, H. S. “A Parametric Analysis of Orbital Debris Collision Probability and Maneuver Rate for Space Vehicles. NASA”. In: *National Aeronautics and Space Administration, Lyndon B. Johnson Space* (1992).

[33] Gehly, S. “State Noise Compensation”. In: AE-4898 Space debris tracking and mitigation, TU Delft. 2024.

[34] Gehly, S. “Study of Formation Flying Described by Relative Eccentricity/Inclination Vector Separation”.

[35] Geul, J. “On the Uncertainty of Space Debris Trajectory Predictions”. 2023.

[36] Ghrist, R. W. and Plakalovic, D. “Impact of Non-Gaussian Error Volumes on Conjunction Assessment Risk Analysis”. In: *AIAA/AAS Astrodynamics specialist conference* (2012).

[37] Hall, D. T. “Expected Collision Rates for Tracked Satellites”. In: *Journal of Spacecraft and Rockets* 58.3 (2021), pp. 715–728.

[38] Hall, D. “Software Development Kit: Three-Dimensional Probability of Collision (Pc) Calculations”. 2021.

[39] Hall, D. T., Baars, L. G., and Casali, S. J. “A Multistep Probability of Collision Computation Algorithm”. In: *AAS/AIAA Astrodynamics Specialist Conference*. 2023.

[40] Hall, D. T., Hejduk, M. D., and Johnson, L. C. “Remediating Non-Positive Definite State Covariances for Collision Probability Estimation”. In: *AAS/AIAA Astrodynamics Specialist Conference.* No. GSFC-E-DAA-TN44826-1 (2017).

[41] Hall, L. “The History of Space Debris”. 2014.

[42] Hejduk, M. D. and Snow, D. E. “Satellite Conjunction ”Probability,” ”Possibility,” and ”Plausibility”: A Categorization of Competing Conjunction Assessment Risk Assessment Paradigms”. In: *AAS/AIAA Astrodynamics Specialist Conference* No. GSF-E-DAA-TN71111-1 (2019).

[43] Hejduk, M. D., Snow, D. E., and Newman, L. K. “Satellite Conjunction Assessment Risk Analysis for ”Dilution Region” Events: Issues and Operational Approaches”. In: *Space Traffic Management Conference* (2019).

[44] Junkins, J. L. and Schaub, H. *Analytical Mechanics of Space Systems*. 2nd ed. American Institute of Aeronautics and Astronautics, 2009.

[45] Kahle, R., Wermuth, M., Schlepp, B., and Aida, S. “The TerraSAR-X / TanDEM-X Formation Flight: Challenges to Flight Dynamics and First Results”. 2011.

[46] Kahle, R., Schlepp, B., and Kirschner, M. “TerraSAR-X / TanDEM-X Formation Control - First Results From Commissioning and Routine Operations”. 2011.

[47] Kelso, T. S., Vallado, D., Chan, J., and Buckwalter, B. “Improved Conjunction Analysis via Collaborative Space Situational Awareness”. In: *9th Advanced Maui Optical and Space Surveillance Technologies Conference, Maui, HI* (2008).

[48] Kerr, E. and Ortiz, N. S. “State of the Art and Future Needs in Conjunction Analysis Methods, Processes and Software”. In: *Proceedings of 8th European Conference on Space Debris (virtual edition, SDC8)* (2021), pp. 20–23.

[49] Kessler, D. J. and Cour-Palais, B. G. “Collision frequency of artificial satellites: The creation of a debris belt”. In: *Journal of Geophysical Research: Space Physics* 83.A6 (1978), pp. 2637–2646.

[50] Kholshevnikov, K. V., Kokhirova, G. I., Babadzhanov, P. B., and Khamroev, U. H. “Metrics in the space of orbits and their application to searching for celestial objects of common origin”. In: *Monthly Notices of the Royal Astronomical Society* 462.2 (2016), pp. 2275–2283.

[51] Krieger, G., Moreira, A., Fiedler, H., Hajnsek, I., Werner, M., Younis, M., and Zink, M. “TanDEM-X: A Satellite Formation for High-Resolution SAR Interferometry”. In: *IEEE Transactions on Geoscience and Remote Sensing* 45.11 (2007), pp. 3317–3341.

[52] Luo, Y. Z. and Yang, Z. “A review of uncertainty propagation in orbital mechanics”. In: *Progress in Aerospace Sciences* 89 (2017), pp. 23–39.

[53] Maruskin, J. M. “Distance in the space of energetically bounded Keplerian orbits”. In: *Celestial Mechanics and Dynamical Astronomy* 108.3 (2010), pp. 265–274.

[54] Mashiku, A. K. and Hejduk, M. D. “Recommended Methods for Setting Mission Conjunction Analysis Hard Body Radii”. In: *2019 AAS/AIAA Astrodynamics Specialist Conference* No. GSFC-E-DAA-TN71115-1 (2019).

[55] McDowell, J. C. “The Low Earth Orbit Satellite Population and Impacts of the SpaceX Starlink Constellation”. In: *The Astrophysical Journal Letters* 892.2 (2020), p. L36.

[56] Montenbruck, O., Kirschner, M., and D’Amico, S. “E-/I-vector separation for GRACE proximity operations”. In: *DLR/GSOC TN* (2004), pp. 04–08.

[57] Montenbruck, O., Kahle, R., D’amico, S., and Ardaens, J.-S. “Navigation and Control of the TanDEM-X Formation”. In: *The Journal of the Astronautical Sciences* 56.3 (2008), pp. 341–357.

[58] Mooij, E. “The Space-Debris Problem”. In: AE-4898 Space debris tracking and mitigation, TU Delft. 2024.

[59] Mooij, E. and Noomen, R. “Conjunction Analysis”. In: *Safety Design for Space Operations*. 2013. Chap. 8.3, pp. 441–466.

[60] NASA. *April 1961 - First Human Entered Space*. Apr. 1961. URL: `https://www.nasa.gov/image-article/april-1961-first-human-entered-space/#:~:text=Yuri%20Gagarin%20from%20the%20Soviet,not%20land%20inside%20of%20capsule.` (visited on 02/06/2024).

[61] NASA. *July 20, 1969: One Giant Leap for Mankind*. June 2019. URL: `https://www.nasa.gov/history/july-20-1969-one-giant-leap-for-mankind/` (visited on 02/06/2024).

[62] NASA CARA. “Software Development Kit: Monte Carlo Probability of Collision (Pc) from TCA (in equinoctial elements)”. 2019.

[63] NASA CARA. “Software Development Kit: Two-Dimension Probability of Collision (Pc) Calculations”. 2019.

[64] Newman, L. K., Frigm, R., and Mckinley, D. “It’s Not a Big Sky After All: Justification for a Close Approach Prediction and Risk Assessment Process”. In: *2009 AAS/AIAA Astrodynamics Specialist Conference* No. AAS 09-369 (2009).

[65] Patera, R. P. “General Method for Calculating Satellite Collision Probability”. In: *Journal of Guidance, Control, and Dynamics* 24.4 (2001), pp. 716–722.

[66] *Privateer Wayfinder*. URL: `https://wayfinder.privateer.com/` (visited on 12/12/2024).

[67] Pu, H., Guangwei, W., Yingkai, C., and Zhaokui, W. “Reduction of Space Debris Collision Prediction Uncertainty Based on Q-Sat Precise Orbit”. In: *Space: Science and Technology* 3 (2023), p. 0005.

[68] Saingyen, P., Channumsin, S., Sreesawet, S., Puttasuwan, K., and Limna, T. “Performance Investigation of the Conjunction Filter Methods and Enhancement of Computation Speed on Conjunction Assessment Analysis with CUDA Techniques”. In: *Aerospace* 10.6 (2023), p. 543.

[69] Schiemenz, F., Utzmann, J., and Kayal, H. "Survey of the operational state of the art in conjunction analysis". In: *CEAS Space Journal* 11 (2019), pp. 255–268.

[70] Shafer, G. *A mathematical theory of evidence*. Princeton University Press, 1976.

[71] Space-Track.org. *Introduction to the API*. URL: `https://www.space-track.org/documentation` (visited on 02/13/2024).

[72] *Survalyzer Enquêtesoftware*. URL: `https://survalyzer.com/nl/` (visited on 01/22/2025).

[73] Swan, M. "Anti-satellite Tests: A Risk to The Security and Sustainability of Anti-satellite Tests: A Risk to The Security and Sustainability of Outer Space". In: *Liberty University Journal of Statesmanship & Public Policy* 3.1 (2022), p. 4.

[74] Tapley, B. D., Schutz, B. E., and Born, G. H. *Statistical Orbit Determination*. Elsevier, 2004.

[75] Tudat-Space. *Estimation Settings*. URL: `https://docs.tudat.space/en/latest/_src_user_guide/state_estimation/estimation_settings.html` (visited on 08/29/2024).

[76] U.S. Space Command Public Affairs Office. "Russian direct-ascent anti-satellite missile test creates significant, long-lasting space debris". 2021.

[77] United Nations Office for Outer Space Affairs. "Space Debris Mitigation Guidelines of the Committee on the Peaceful Uses of Outer Space". 2010.

[78] Uriot, T., Izzo, D., Simões, L. F., Abay, R., Einecke, N., Rebhan, S., Martinez-Heras, J., Letizia, F., Siminski, J., and Merz, K. "Spacecraft collision avoidance challenge: Design and results of a machine learning competition". In: *Astrodynamics* (2022), pp. 1–20.

[79] Vallado, D. A. *Fundamentals of Astrodynamics and Applications*. 4th ed. Microcosm Press, 2013.

[80] Vananti, A., Meyer zu Westram, M., and Schildknecht, T. "Metrics on space of closed orbits for near-Earth objects identification". In: *Celestial Mechanics and Dynamical Astronomy* 135.5 (2023), p. 51.

[81] Wakker, K. F. *Fundamentals of Astrodynamics*. TU Delft Repository, Delft, 2015.

[82] Zorich, V. A. *Mathematical Analysis II*. 4th ed. Springer, 2002.

A

Thesis Project Plan

In this appendix, part of the project plan established during the initial stages of the research is presented. The introduction is omitted to avoid repetition.

A.1. Methods

The expected methods that will be conducted are highlighted in this section. Before new methods can be implemented, current practice in conjunction analysis should be studied and implemented such that TCA, MD and P_c can be calculated for two potentially colliding satellites. To this end, a benchmark needs to be set up for which the correct integrator and propagator combination must be chosen, including the correct stepsize. For this baseline performance, it is important to study which different dynamical models need to be included in the propagation of the states. For example, the bodies that need to be added in the model and the order and degree of the spherical harmonics model. A balance needs to be found for the inclusion of as many accurate models as possible, and the time it will take for a propagation to run. Before the benchmark can be created, physical and benchmark errors should be chosen. Both the state and the covariance need to be propagated, both backwards and forwards. Both propagations should be tested and verified. There are different methods for propagating the covariance, thus a method both efficient and accurate should be chosen [52].

When the benchmark propagation is set up, a conjunction needs to be simulated. Then, algorithms and equations to find the corresponding time of closest approach, miss distance and probability of collision should be implemented. Algorithms should be verified before use. As mentioned before, there are some limitations on the assumptions made for the P_c calculation, the effect of these assumptions could be tested as well. For example, P_c is only valid for short encounters [10], thus testing what happens for a longer encounter can give more insights into the problem. The other assumptions can be tested as well. A Monte Carlo algorithm can also be implemented for the calculation of P_c. Although this is slow, it can give some insights into how well the 2D calculation approaches the actual collision risk.

Then the next step is to set up a simulation environment, where different conjunctions can be tested. In this simulation environment, the existing methods can be tested for multiple different types of orbits. Sun-synchronous orbits, orbits in GEO, LEO and MEO, circular orbits and highly elliptical orbits can all be tested. In the literature review, new methods that could be used to expand conjunction analysis are identified. After the simulation set up is complete and tested, new metrics can be evaluated. The new methods could be applied both individually as simultaneously, such that the combination yielding the best performance can be identified.

A.2. Tools, Algorithms & Data

For the research TUDAT will be used. The data used will be simulated in the form of conjunction simulations. Other data types, if available, could be used for further verification and testing. CDMs might be used for this regard, but a correct data source still needs to be found for this. The extra data depicted in Table J.1 thus needs to be further investigated. For the calculation of the TCA and MD the algorithm as derived by Denenberg could be used [22]. This needs to be implemented in Python. P_c can be found using the 2D calculation or a Monte Carlo algorithm analysis as introduced by Foster and Estes [32]. This also needs to be implemented in Python. The

NASA CARA team has implemented various different methods for the calculation of P_c. These methods could be used.

Type of data	File formats	Collection	Purpose	Storage	Access
Simulated data	.txt files	Simulation	Find collision risk	Gitlab	TNO and TU Delft
CDMs	.cdm	Download	Conjunction simulation	Gitlab	TNO and TU Delft

Table A.1: Data that is expected to be used.

A.3. Expected Results

The hypothesis is that the current methods used for conjunction analysis can be further improved using different methods. When assessing the performance using Type 1 and Type 2 errors, the expectation is that implementing methods such as possibility and plausibility measures (instead of the probability measure) will lead to a higher amount of false positives. This is due to the different null hypothesis defined for these different methods. For the probability, the default state is to not make a mitigation maneuver, whilst for the possibility and plausibility the default state is to make a maneuver. The amount of false negatives will consequently be decreased. When combining this with a measure that could be used for filtering potential conjunctions this might yield an optimal performance. Outer probability measures might decrease the amount of false positives due to the fact that for some detections the data will be categorized as too uncertain, and thus no mitigation measure will be taken. The results of the implementation of the distance metrics could be used to get multiple different miss distances and assess all these different distances by a threshold. Assessing a conjunction on multiple distance metrics might both yield less Type 1 and Type 2 errors. The relative motion description might yield a faster method of assessing the collision risk.

A.4. Planning

The methodology can be divided into multiple work packages divided over the different research phases. This is shown below.

Literary review (Week 1 - Week 6): Research proposal deliverable week 6

- Identify the need for conjunction analysis
- Study the current practices used in CA
- Identify the limitations of current practices
- Study new methods that could be implemented to improve CA

Research Phase 1 (Week 7 - 17): Mid Term deliverable week 16

- Find additional data apart from simulated data
- Create benchmark propagation
- Choose propagation method covariance propagation
- Implement + validate current methods for finding TCA, MD, P_c
- Verify limitations of assumptions for P_c
- Choose a couple of new methods that can be implemented and implement
- Retrieve first result

Research Phase 2 (Week 18- 28): Thesis draft deliverable week 26

- Validate results
- Find conclusion

Submission Phase (Week 29 - Week 37)

- Finish up thesis
- Prepare for defense

A Gantt chart is used to give a broad idea of the planning for the different phases. Note that research phase 1 is planned out in more detail then research phase 2. Every phase has been given some room for iteration. The milestone meeting plan can be seen in the chart. Note that the set holidays may change, and the milestones/key review/deliverables dates might thus change a bit. The initial Gantt chart is shown in Figure A.1.

After the mid-term, an updated planning was made for the second research phase, visualized in Table A.2. As can be seen, the first results were not entirely retrieved yet, as the covariance estimation was in the final stages at the start of the second research phase. Furthermore, the different metrics were not implemented yet, which was the planning according to the Gantt chart. This planning thus had to be updated.

Table A.2: Planning of the second research phase.

Week	Deliverable	Goal
18	Mid-term review	Covariance estimation finished
19		Implement first metric: Relative Parameters or OPMS + document it
20		Assess performance first metric. Define some cases with impact, and some cases without impact. Check when the OPMs assess the conjunction as impact, vs the probability of collision. Document results
21		Create interview questions and send out, implement second metric + document
22		Implement third metric + document
23		Assess newly implemented metrics + document results
24		Assess the metrics for other testcases + document results
25	Work on PPD	Every Monday + study for exam
26	Vacation	
27		Assess interview results + Finish up Monte Carlo assessment (low priority) + document + reiteration
28		Re-iteration + draft of conclusion/abstract
29	Draft Submission	Hand in thesis draft on Wednesday
30		
31	Green Light Review	Work on feedback thesis
32	Request Examination	Work on feedback thesis
33	Christmas break	
34	Christmas break	
35		Final details
36	Thesis submission	Submit final thesis
37		Prepare defense
38	Thesis Defense	
39		7 Extra vacation week for unforeseen events

A.5. Conclusions

The risk of in-orbit collisions between space objects is increasing due to the rising number of spacecrafts and space debris fragments present in highly populated regimes. The current modus operandi in studying the risk of such collisions is not representative of the complete picture. These methods may be expanded by looking at outer-probability measures, relative orbit parameterizations, and distance metrics. Furthermore, the timeliness of the data will be analysed. The different methods will be studied and tested simultaneously to see which combination of methods will yield the best performance. When a successful expansion has been found, a further goal is to present a useful output for the methods.

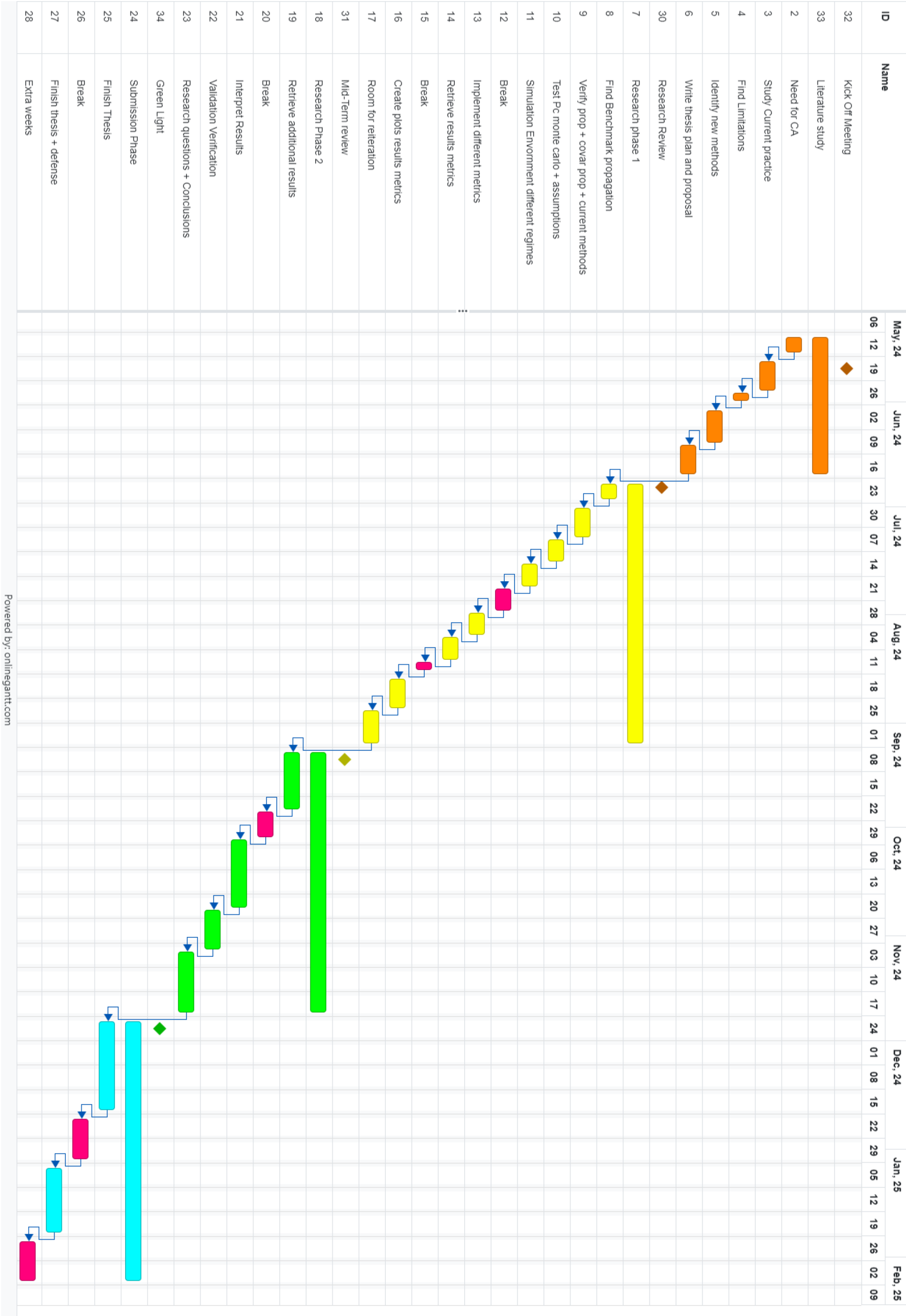

Figure A.1: Initial planning given in a Gantt chart.

B
Propagation

B.1. State propagation

The state propagation is analysed using data from the CDM associated with the first Starlink-on-Starlink test case. For the selection of the integrator, propagator and acceleration models an analysis is conducted using one of the two Starlink satellites, namely Starlink-3254. The state needs to be propagated forward and backward as mentioned in Chapter 4. The goal of the backward propagation is to propagate the satellite states from t_{TCA} to t_0. This should approximate the states used for the generation of the CDM. Using these states, a realistic conjunction scenario is simulated, providing a basis for the evaluation of different conjunction assessment metrics.

A propagation incorporates multiple error sources. The propagation will be affected by numerical errors, which can originate from both rounding and truncation errors. The latter are caused by the fact that a propagated state is an approximation of the actual state. Furthermore, the propagation leads to errors due to model simplifications and imperfect knowledge. The former error source exists due to the fact that often a simplified dynamical model is used for running efficiency. The latter error source arises from the fact that the initial state used for propagation is influenced by measurement errors, and the model description is limited in accuracy due to the available information. For example, parameters such as the drag coefficient and the solar radiation pressure coefficient are difficult to determine, as their values depend on factors such as the shape, material, and orientation of the satellite.

The accuracy of the dynamical model can be assessed by defining a high-fidelity benchmark model using TUDAT and comparing it to models where perturbations are removed one by one. By comparing the high-fidelity model with simplified models, the acceleration model for which a certain accuracy requirement is met can be established. The accuracy requirement has been set to 1 m. This requirement has been established as a CDM is published when the miss distance is less than 1 km. Thus, to be certain that the number of missed conjunctions due to the selection of the dynamical model is limited, the model requirement has been set three orders of magnitude below the CDM requirement. The state of Starlink-3254 has been propagated for seven days, as this is the common length of a screening period. The propagation has been conducted using an RKDP7 integrator with a step size of four seconds. The benchmark model included perturbing forces due to the spherical harmonics (SPH) of the Earth (degree and order 200), spherical harmonics of the Moon (degree and order 20), point mass (PM) gravity of the Sun and planets, atmospheric drag ($C_d = 2.2$, model US76), radiation pressure (RP, $Cr = 1.3$) and relativistic effects (RE). All perturbations were then either removed or simplified. The results can be seen in Figures B.1b and B.1a. In the legend, the simplifications are indicated. For more clarity, they are first explained here. “Moon PM”, indicates that the acceleration due to the spherical harmonics (degree and order 20) of the Moon is simplified to the acceleration due to the point mass gravity of the Moon. The lines with a minus before them (“-Drag”, “-RP”, “-RE”, “-Planets”), show the results for dynamical models without the respective force. For labels including “Earth” followed by two numbers, the spherical harmonics (degree and order 200) of the Earth are relaxed to a lower order and degree. The line defined by “All Simplifications” represents the model for which the simplifications that were deemed justified were relaxed or removed all at once. This thus means that the Moon is approximated as point mass, the perturbing forces of the planets were removed and the degree and order of the spherical harmonics of the Earth were set to 100. As the latter force is dominant over the other two forces, the line for this model simplifications is almost identical to the line of “Earth 100,100”.

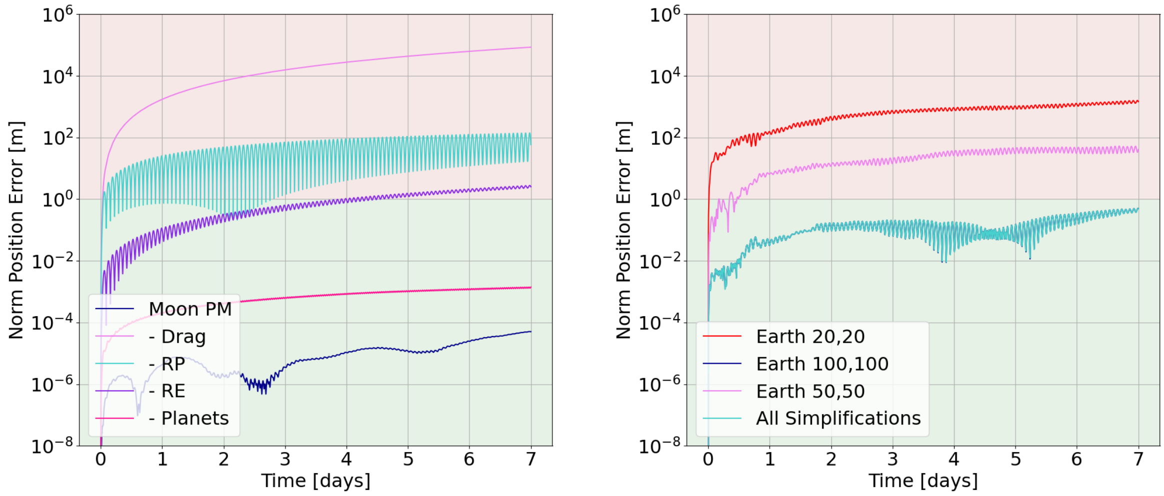

(a) General perturbations adjusted.

(b) Spherical harmonics models adjusted.

Figure B.1: Evaluation of acceleration models needed for the propagation.

As can be seen, the models needed for the requirement are of relatively high fidelity. All the planets can be left out of the simulation, and the Moon can be approximate as point mass, but the degree and order of the spherical harmonics of the Earth can not be lower than 100. This model was thus very slow to run. The CDM published on Privateer Wayfinder is however also accompanied with information on the dynamical model used. It states that the spherical harmonics model of the Earth is set to a degree and order of 20, and the third-body perturbations included are the Moon and the Sun. Thus these perturbations, together with radiation pressure and atmospheric drag are used to propagate the states backward and forward. Although the question could arise on whether this dynamical model will not lead to many missed or wrongly identified conjunctions, the use of the model can be justified by the fact that the model is also used in reality. Furthermore, the goal of the forward and backward propagation is to find the states at t_0 (the start of the screening period), such that the conjunction scenario can be predicted at t_{TCA} with identical characteristics as the scenario found in the CDM. The forward and backward propagation thus needs to be consistent, and the numerical error will be more important. Due to these reasons, and the advantage of the computational efficiency of the model, the choice was made to run the analysis with the lower-fidelity model, consistent with that used by Privateer Wayfinder.

For the analysis of the integrator type and its associated stepsize or tolerance, the numerical error is evaluated using backward and forward propagation. In principle, the object follows a trajectory determined by the laws of physics (when no thrust is used). The numerical propagator should thus give the same results when backward and forward propagating the state using an identical dynamical model. However, numerical truncation and rounding errors will cause a deviation from the initial state after propagating backward and forward. The numerical error can be established by assessing the position error after the propagations. The permissible error is set to 1 centimeter (10^{-2} m), to ensure the propagation is accurate. As objects are screened for conjunctions for approximately seven days, the forward and backward propagation is performed for seven days. For the integrator the fixed Dormand-Prince (RKDP7) integrator is used. This is an often used integrator for astrodynamics problems. The order of the integrator is not too high, which would lead to a large stepsize permissible with the requirement. This may lead to unreliable results for a fast changing dynamical model. But the order is also not too low, which would yield a very low stepsize needed to achieve the permissible error. The Cowell propagator is used for propagation, this is a straight forward and accurate propagator that is valid for many different astrodynamics problems. The propagation has been initialized at time t_{TCA}, as given in the CDM. Furthermore, the state of the first object present in the CDM is again used. This state has been back propagated from t_{TCA} to t_0. The name of t_0 might be misleading here, as this time is thus not equal to zero, but is defined as minus seven days. This time is defined as t_0 as it represents the start of a screening period for conjunction analysis. Then, to determine the error after backward and forward propagation, the state of the object is found at t_0, and again initialized for a forward propagation from t_0 back to t_{TCA}. At every epoch, the difference between the states after forward and backward propagation has then been found. Figure B.2 shows the positional error over time. As expected, the error is zero at t_0, indicated by $t = -7$ days in the plot. This is as expected, as the state at t_0 has been directly copied for the forward propagation, and thus the difference between the state at $t = -7$ days is equal to zero. The maximum error can be found at t_{TCA}, as the errors accumulate over the course of propagation. The maximum error has been found to be below 10^{-2} m when performing the analysis with a timestep of four seconds. The performance thus obeys the requirement.

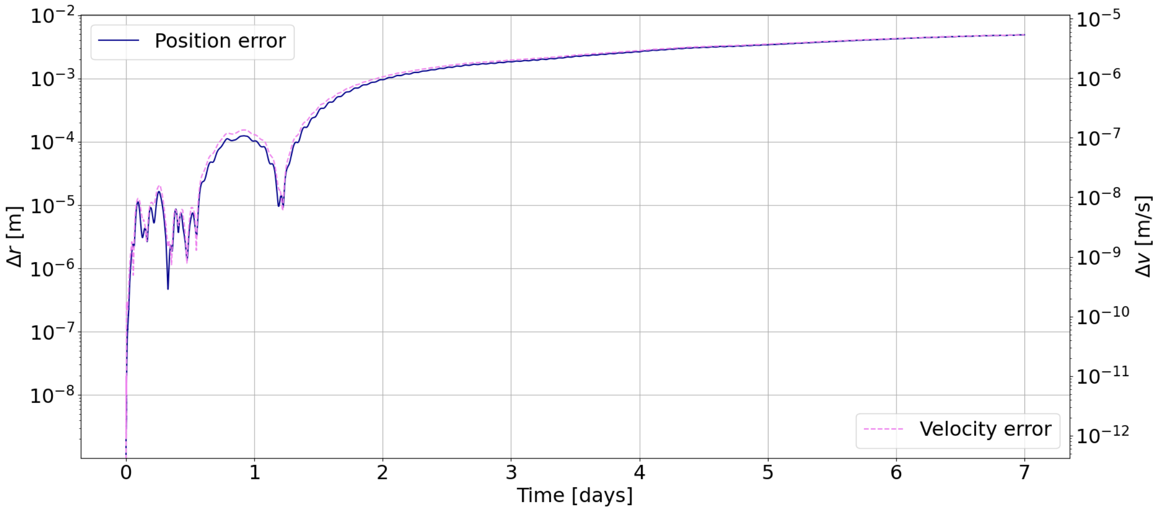

Figure B.2: Error in position and velocity after propagating backward and forward.

The backward propagation needs to be very accurate to ensure that, during the test case setup, similar states as the ones used to generate the CDM are found. When the states at t_0 are found, the requirements for forward propagation can be relaxed. Namely, the analysis will consist of finding the miss distance, time of closest approach, probability of collision, and other possible new metrics. This will often need to be done, leading to the need for an accurate but fast model. The numerical error requirement for forward propagation can be increased with an order, such that the permissible error is now set to 0.1 m. For the backward propagation, the fixed RKDP7 integrator was used for consistency. For the forward propagation, variable integrators can also be considered. These often require fewer function evaluations, and the automatic timestep adaption yields a good performance for highly elliptical orbits. To test which integrator is best suitable to be used, multiple integrators with various different stepsizes or tolerances have been tested. The results for these various integrator settings are compared to the results of the integrator settings as defined for the backward propagation. The trajectory following from the RKDP7 integrator with a stepsize of four seconds, is thus used as a benchmark. The new, to be tested, settings can be seen in Table B.1 and the results of the analysis can be seen in Figures B.3a and B.3b.

Table B.1: Integrator settings for the integrator analysis.

.	Fixed stepsizes	Variable tolerances
RKF4(5)	$[1, 5, 10, 20, 30]$	10^{-15+i}
RKF7(8)	$[20, 30, 50, 70, 80]$	10^{-15+i}
RKDP8(7)	$[10, 20, 30, 40, 70]$	10^{-13+i}
BS(2)	$[5, 10, 20, 30, 40]$	10^{-13+i}
BS(4)	$[30, 40, 55, 70, 100]$	10^{-13+i}
BS(6)	$[30, 40, 55, 70, 100]$	10^{-13+i}

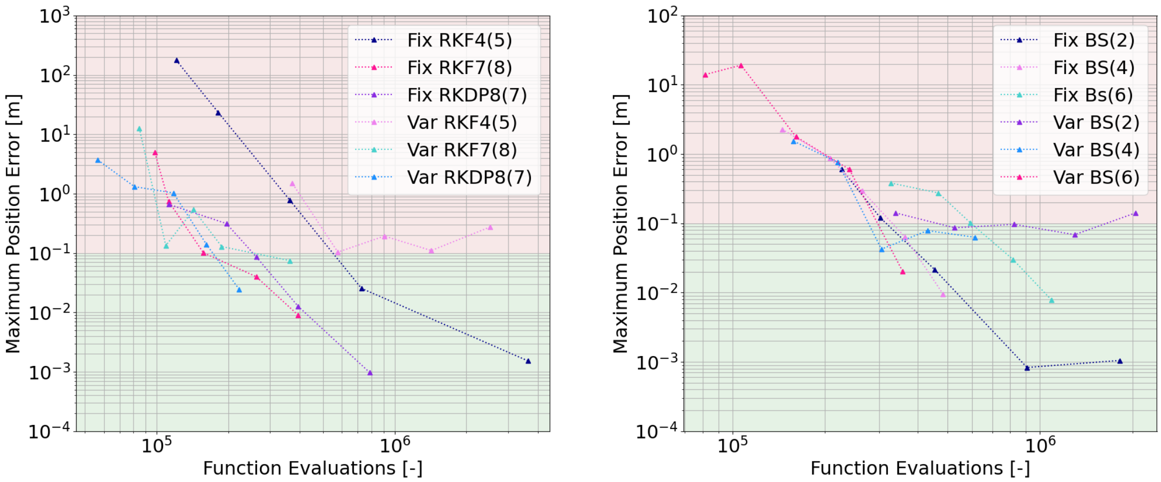

(a) Runge Kutta and Dormand Prince integrators.

(b) Bulirsch-Stoer integrators.

Figure B.3: The maximum position error as a function of the number of function evaluations.

As can be seen, the variable RK integrators use fewer function evaluations than the fixed RK integrators. For the BS integrators this effect is less visible. The fixed integrators show a more consistent behavior compared to the variable ones. Meaning that when the stepsize gets lower, the performance gets better. The trend is more smooth for the fixed integrators. This may be due to the fact that the settings for the fixed integrators are in the truncation dominated region, whilst the settings for the variable integrators are in the rounding dominated region. Both the BS6 and RKDP8(7) variable integrators show promising results. Since the fixed step RKDP7 integrator is also used for the backward propagation, the choice was made to use the variable RKDP8(7) integrator with a tolerance of 10^{-13} for the forward propagation.

The complete settings used for the backward and forward state propagation are shown in Table B.2.

Table B.2: Settings for backward and forward propagation.

	Backward	Forward
Dynamical Models	Earth spherical harmonics 20D 20O Atmospheric Drag ($C_d = 2.2$, model = US76) Sun point mass gravity Sun radiation pressure ($C_r = 1.3$) Moon point mass gravity	Earth spherical harmonics 20D 20O Atmospheric Drag ($C_d = 2.2$, model = US76) Sun point mass gravity Sun radiation pressure ($C_r = 1.3$) Moon point mass gravity
Integrator	Fixed RKDP7 $\Delta t = 4$ s	variable RKDP8(7) tolerance $= 10^{-13}$
Propagator	Cowell	Cowell

For the physical characteristics of the satellites, the DISCOS database is used.

B.2. Covariance propagation

The covariances of the states at t_0 are determined using a batch estimator. An initial uncertainty in a state is a result of multiple different aspects. First, the state estimate is influenced by measurement errors. Measurements are used to estimate the state, that is, a state is fitted to the measurements. However, there is a range of states that can fit these measurements, resulting in uncertainty. Second, the dynamical model used for the estimation process can also contribute to a deviation from the actual state, leading to additional uncertainty. Third, numerical errors occur in the orbit determination process, further contributing to the covariance, however this is not typically accounted for in the batch fitting process. As an object's state is propagated, the uncertainty in the state increases. When performing a Monte Carlo analysis for example, all the deviated states follow a different trajectory, leading to a spread of the possible states over time. This effect can be seen in Figure B.4

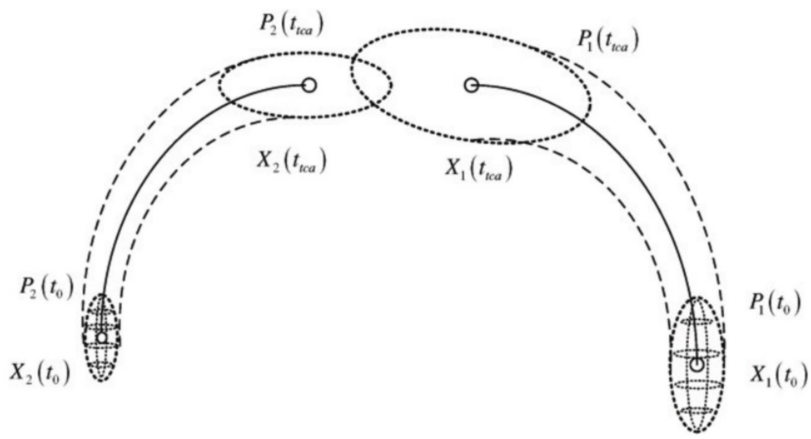

Figure B.4: The covariance growth for two space objects, from Reference [67]

A covariance matrix can be propagated using various methods. For example, a linear stochastic propagation can be used, the unscented transform method, a Monte Carlo algorithm or numerous other propagation methods. For the linear propagation the state transition matrix $\mathbf{\Phi}$ is used. The matrix $\mathbf{\Phi}$ at a certain epoch t is given by:

$$\mathbf{\Phi}(t, t_0) = \frac{\partial \vec{x}(t)}{\partial \vec{x}(t_0)}. \tag{B.1}$$

With $\vec{x}$ the state. For a propagation excluding noise, the covariance matrix $\mathbf{P}$ at time t can be found with:

$$\mathbf{P}(t) = \mathbf{\Phi}(t, t_0)\mathbf{P}(t_0)\mathbf{\Phi}(t, t_0)^T. \tag{B.2}$$

The covariance can also be propagated by performing a Monte Carlo analysis. This is the most accurate method of covariance propagation, if the number of samples used for the analysis is sufficient. States can be sampled using a multivariate normal distribution of the associated covariance. With the deviated sampled states $\vec{x}_{d_i}(t_0)$, the initial deviations in the states can be found with:

$$\Delta\vec{x}_{MC_i}(t_0) = \vec{x}(t_0) - \vec{x}_{d_i}(t_0). \tag{B.3}$$

With $\vec{x}(t_0)$ the initial state, and $\Delta\vec{x}_{MC_i}(t)$ the initial state deviation. Every sample is then again propagated for seven days. After the propagation, the deviated sample states $\vec{x}_{d_i}(t)$ are used for the computation of the covariance matrix. For time t, the mean deviated state is calculated using:

$$\bar{\vec{x}}_d(t) = \frac{1}{N}\sum_{i=1}^{N} \vec{x}_{d_i}(t). \tag{B.4}$$

With N_s the number of samples. The covariance is then computed using:

$$\mathbf{P}(t) = \frac{1}{N_s}\sum_{i=1}^{N_s} (\vec{x}_{d_i}(t) - \bar{\vec{x}}_d(t))(\vec{x}_{d_i}(t) - \bar{\vec{x}}_d(t))^T. \tag{B.5}$$

Using the state transition matrix, the linear state deviation $\Delta\vec{x}_L$ at time t can be found using:

$$\Delta\vec{x}_L(t) = \mathbf{\Phi}(t, t_0)\Delta\vec{x}_L(t_0). \tag{B.6}$$

Where $\Delta\vec{x}_L(t_0)$ represents the initial deviation $\vec{x}(t_0) - \vec{x}_d(t)$. To assess the linearization error as a result of propagating the covariance using a linear propagation model, linear initial deviations can be taken equal to the initial Monte Carlo deviations samples $\Delta\vec{x}_{MC}(t_0)$. When running the Monte Carlo analysis and the linearization propagation both for the same sample deviations $\Delta\vec{x}(t_0)$, the linearization error can be found for a single sample with:

$$\Delta\vec{r}_i(t) = \Delta\vec{r}_{L_i}(t) - \Delta\vec{r}_{MC_i}(t). \tag{B.7}$$

Where $\Delta\vec{r}_{L_i}$ and $\Delta\vec{r}_{MC_i}$ are the position vectors within the full state vectors. The linearization error $\Delta\vec{r}$ can be used to quantify the error incurred to the linearization of the problem. To find this linearization error, first it must be verified that the sample size used for the Monte Carlo analysis is sufficient. For this, a Kolmogorov-Smirnov test can be used [35]. The Monte Carlo run with 10000 samples can be divided into multiple sub-sample sets. All sets have different sizes, given by $N_s = 100,\ 200,\ 400,\ 1000,\ 2000,\ 4000,\ 6000,\ 8000$. The KS-test can be used to compare the underlying CDF of the total sample set to the CDF of one of the sub-sample sets. The KS-statistic then gives a measure of whether the sample sets originate from the same distribution. If this is the case, this would indicate that the sample size used is sufficient. It must be noted however, that when a sub-sample set encompass a small part of the total sample size, there are multiple different possibilities for the combination of different samples drawn into this set. To account for this, the test should thus be repeated multiple times, to determine the maximum KS-statistic for a certain sample size. The higher the number of sub-samples, the less times the algorithm needs to be repeated. The number of times for which the sub-samples sizes given above are run for are given by $N_R = 3200,\ 1600,\ 800,\ 320,\ 160,\ 96,\ 63,\ 31$ respectively [35]. This leads to the results shown in Figure B.5.

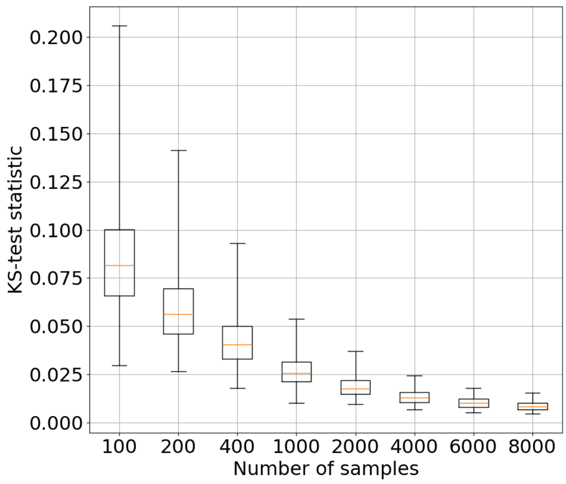

Figure B.5: Kolmogorov–Smirnov test statistic as a function of the sample size.

To determine if the sample size is sufficient, it is necessary to establish the allowable change in KS. This can be achieved by defining the maximum allowable offset in the determined linearization error. When considering only the error after a seven-day propagation, this results in the CDF shown in Figures B.6a and B.6b.

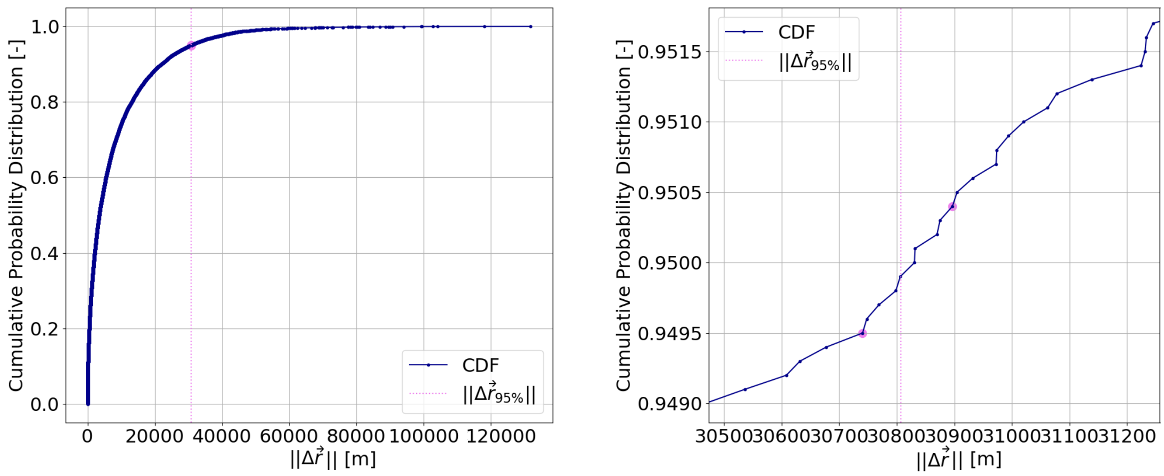

(a) CDF. **(b)** CDF, zoomed in.

Figure B.6: Cumulative probability distribution as a function of the linearization error.

To determine the linearization error, it has been determined that 95% of all the errors found, should be below the set error. This error has been marked in Figures B.6a and B.6b. Since the linearization error is only used as a measure for the error introduced by linearized propagation method, the allowed offset has been set to 10%. This ensures that the order of magnitude of the error remains similar. The allowed change in the KS statistic can then be found using:

$$\Delta\%_{KS} = \Delta\%_{\Delta\vec{r}} \nabla \Delta\vec{r}_{95\%}. \tag{B.8}$$

Where ∇ represent the gradient $\frac{\partial KS}{\partial \Delta\vec{r}}$ and was found to be equal to $5.77 \cdot 10^{-7}$. Furthermore, the linearization error at the 95^{th} percentile $\Delta\vec{r}_{95\%}$ was found to be equal to 30807.2 m, and the allowed change in the error $\Delta\%_{\Delta\vec{r}}$ was defined to be equal to 0.1. This leads to an allowed $\Delta\%_{KS}$ of 0.018. As can be seen in the figure, the maximum KS statistic found for both a sample size of 6000 and 8000 samples is below this allowed change. Thus a sample size of 10000 samples has been deemed sufficient to determine the error due to linearization. The linearization error after a propagation of seven days was found to be equal to 30807.2 m. Figure B.7 shows the error behavior over the course of propagation. The linearization errors have been chosen with a 95 percent confidence interval.

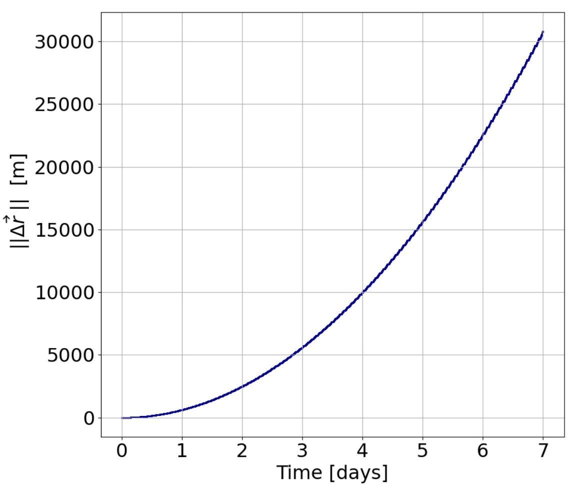

Figure B.7: The linearization error over time for a confidence interval of 95%.

As can be seen the error grows quickly over time. Although this linearization error is very significant, the linear propagation method is still used for the propagation of the covariance. This choice has been made as the time required to run multiple different Monte Carlo analysis is deemed too large for an effective analysis of different risk assessment metrics. A linearized propagation is also often used in practice, due to the same reason. Furthermore, as also mentioned in Chapter 4, it is important that the methodology used is both consistent and repeatable, which is the case for a linearized propagation. Although other propagation methods could be used, the analysis and implementation of these different propagation methods is considered out of scope for this research.

C

Covariance Estimation

A covariance matrix can be estimated using orbit determination processes. First, the general orbit determination process will be explained here. Second, the method used to estimate the covariance is described. Last, the settings for the estimation process are defined.

An orbit determination process is used to estimate the state $\vec{x}$ of a satellite at a certain time t. For this process, tracking data are needed. This data can include radar data, optical data, laser ranging data or various other data sources. The state vector is often described in Cartesian coordinates: x, y, z, v_x, v_y, v_z. When using radar tracking data, the observations often consist of the azimuth, elevation and range information. Due to the difference in coordinates, one cannot directly translate the tracking information into an estimated state for the spacecraft. The relation between the tracking observations and the state vector components is namely non-linear in nature, complicating the process [74].

When one has observations, a dynamical model can be used to approximate the reality. Using the state parameters $\vec{x}$, and the dynamical model represented by the design/information matrix $\mathbf{H}$, the observations $\vec{y}$ can be modelled using [74]:

$$\vec{y} = \mathbf{H}\vec{x} + \vec{\varepsilon}. \tag{C.1}$$

Here $\vec{\varepsilon}$ defines the error between the observations $\vec{y}$ and the modelled observations $\mathbf{H}\vec{x}$, such that $\vec{\varepsilon} = \vec{y} - \mathbf{H}\vec{x}$. The relation between the parameters and the observation is non-linear, however the matrix $\mathbf{H}$ is linearized. This is often accomplished by taking a first order Taylor series expansion and dropping higher-order terms.

To explain the covariance estimation, a linear relation between the observations and parameters is thus assumed. The objective function to minimize is defined by $J = \varepsilon^T \mathbf{P}_{yy}^{-1} \varepsilon$, with $\mathbf{P}_{yy}$ the measurement noise covariance matrix. Using the equation $\vec{\varepsilon} = \vec{y} - \mathbf{H}\vec{x}$ it can be found that:

$$J = \vec{y}^T \mathbf{P}_{yy}^{-1} (\vec{y} - \mathbf{H}\vec{x}) - \vec{x}^T \mathbf{H}^T \mathbf{P}_{yy}^{-1} (\vec{y} - \mathbf{H}\vec{x}). \tag{C.2}$$

Only the second term can be minimized, using either $\vec{x}^T = 0$ or $\vec{x}^T \mathbf{H}^T \mathbf{P}_{yy}^{-1} (\vec{y} - \mathbf{H}\vec{x}) = 0$. The latter can be rewritten such that:

$$\vec{x} = (\mathbf{H}^T \mathbf{P}_{yy}^{-1} \mathbf{H})^{-1} \mathbf{H}^T \mathbf{P}_{yy}^{-1} \vec{y}. \tag{C.3}$$

The covariance matrix of the parameters $\vec{x}$ can then be found using:

$$\mathbf{P}_{xx} = (\mathbf{H}^T \mathbf{P}_{yy}^{-1} \mathbf{H})^{-1}. \tag{C.4}$$

Such an estimation process can be performed using TUDAT. If one has an initial state available, and ground stations which can observe the object are defined, the uncertainty of the initial state can be estimated. TUDAT simulates observations made by the ground stations, which are then used to find the covariance using [75]:

$$\mathbf{P} = (\mathbf{H}^T \mathbf{W} \mathbf{H} + \mathbf{P}_0^{-1})^{-1}. \tag{C.5}$$

Where again $\mathbf{H}$ is the design matrix, found with $\mathbf{H} = \frac{\partial \vec{y}}{\partial \vec{x}}$, for which $\vec{y}$ is the vector of computed observations and $\vec{x}$ is the vector of estimated parameters, $\mathbf{P}_0$ is the initial covariance, often defined as zero, and $\mathbf{W}$ is the weight matrix [75].

The propagation settings of the estimation are set equal to the propagation settings of the backwards propagation as defined in Table B.2. This choice was made as the estimation of the covariance is still a part of the truth data generation, thus the same settings are used. For the estimation, multiple ground stations are defined to simulate the observations with settings documented by Vallado [79] in Tables 4-2, 4-3 and 4-4. The settings used for the covariance estimation are shown in Table C.1.

Table C.1: Observation settings for the covariance estimation.

Sensor	Longitude [°]	Latitude [°]	Altitude [m]	Noise Range[m]	Noise Doppler [°]	Viability [°]
Ascension, Atlantic	-7.91	-14.40	56.1	101.7	0.02655	1
Clear, AK	64.29	149.19	213.3	62.5	0.05155	1
Antigua, West Indies	17.14	-61.79	0.5	92.5	0.01815	0
Kaena Point, HI	21.57	-158.27	300.2	92.5	0.01815	0
Millstone, MA	42.62	-71.49	123.1	150.0	0.01000	0
HayStack, MA	42.62	-71.49	115.7	150.0*	0.01000*	0*

The values with a star (*) for the Haystack sensor are assumed to be the equal to the values of the Millstone radar, as no data was available in the tables for these values. As the estimation is merely used for finding a covariance matrix that rotates correctly, and the covariance is scaled after the estimation, the estimation is sufficient. The Doppler noise was found by taking the average over the elevation and azimuth noise as found in Table 4-3 [79]. Every radar was assigned a one-way instantaneous Doppler link and a one way range link. During a period of three hours, new observations are generated every 60 seconds.

The estimation has been conducted for the Starlink on Starlink conjunction. The states have been backpropagated for $\Delta t_{back} = -7$ days. The original miss distance as provided in the CDM was kept. The standard deviations estimated for the primary object at t_0 are given in Table C.2.

Table C.2: Standard deviations found after estimation.

$\sigma_x[m]$	$\sigma_y[m]$	$\sigma_z[m]$	$\sigma_{v_x}[m]$	$\sigma_{v_y}[m]$	$\sigma_{v_z}[m]$
$4.23 \cdot 10^{-2}$	$3.80 \cdot 10^{-2}$	$2.63 \cdot 10^{-2}$	$3.83 \cdot 10^{-5}$	$3.27 \cdot 10^{-5}$	$5.02 \cdot 10^{-5}$

As can be seen, the covariance is very low. It is thus too optimistic, due to the settings used to generate it. For this reason, the covariance is scaled, as further explained in the methodology.

D

Frame Rotations

An often used and in general more intuitive frame for astrodynamics problems is the RTN frame. The transformation from ECI to RTN is explained in this appendix. First the transformation matrix is calculated using the state vector $\vec{x}$, the position $\vec{r}$, the velocity $\vec{v}$ and the angular momentum vector $\vec{h}$. Another extra vector $\vec{s}$ will be defined using the angular momentum and position:

$$\begin{aligned}
\hat{r} &= \frac{\vec{r}}{||\vec{r}||}, \\
\vec{h} &= \vec{r} \times \vec{v}, \\
\hat{h} &= \frac{\vec{h}}{||\vec{h}||}, \\
\hat{s} &= \hat{h} \times \hat{r}.
\end{aligned} \tag{D.1}$$

The rotation matix $\mathbf{R}^{(RTN/ECI)}$ is then given by:

$$\mathbf{R}^{(RTN/ECI)} = \begin{bmatrix} \hat{r}_x & \hat{r}_y & \hat{r}_z \\ \hat{s}_x & \hat{s}_y & \hat{s}_z \\ \hat{h}_x & \hat{h}_y & \hat{h}_z \end{bmatrix}. \tag{D.2}$$

The rotation matrix can be applied to transform a state $\vec{x}^{(ECI)}$ in ECI to a state $\vec{x}^{(RTN)}$ in RTN by:

$$\begin{aligned}
\vec{r}^{(RTN)} &= \mathbf{R}^{(RTN/ECI)} \cdot \vec{r}^{(ECI)}, \\
\vec{v}^{(RTN)} &= \mathbf{R}^{(RTN/ECI)} \cdot \vec{v}^{(ECI)}.
\end{aligned} \tag{D.3}$$

To rotate a vector from the RTN frame to ECI, the matrix $\mathbf{R}^{(ECI/RTN)}$ can be found with $\mathbf{R}^{(ECI/RTN)} = \mathbf{R}^{(RTN/ECI)^T}$. The covariance matrices provided in the CDMs are often defined in the RTN frame, these can be rotated to ECI with:

$$\mathbf{P}^{(ECI)} = \mathbf{R}^{(ECI/RTN)} \mathbf{P}^{(RTN)} \left(\mathbf{R}^{(ECI/RTN)}\right)^T. \tag{D.4}$$

When the covariance matrix includes both the position and velocity, and is thus 6x6, the rotation matrix also needs to be 6x6. In general, this can be obtained with [74]:

$$\mathbf{R} = \begin{bmatrix} \mathbf{R}_{3\times3} & \mathbf{0}_{3\times3} \\ \mathbf{0}_{3\times3} & \mathbf{R}_{3\times3} \end{bmatrix}. \tag{D.5}$$

E

Sample Size Monte Carlo algorithm for $\sigma_{\Delta\gamma}$

The sample size needed for the transformation of the uncertainty on the initial Cartesian states to the uncertainty on the angle separation needs to be determined. For this, again the KS statistic is used[35]. As was explained in Appendix B, the allowable change in the KS statistic can be determined by defining the acceptable change in the angle separation uncertainty. This latter acceptable change has been set to be equal to 1%. As the possible angle lies within $0°$ and $180°$, this percentage leads to a maximum offset of $1.8°$. The uncertainty on the angle separation has been found as a function of the covariance size as shown in Figure 5.29. As can be seen, the approximate sizes of the standard deviations $\sigma_{\Delta\gamma}$ observed lie within an interval of $[1°, 60°]$. Although a change of $1.8°$ on an uncertainty equal to $1°$ is a significant, it is acceptable for the application of the metric, as the metric yields a stable solution over time. As was seen for the TSX/TDX test case, it takes approximately 30 days to go from an angle equal to $180°$ to $80°$, so the effect of an offset of $1.8°$ will not have a significant effect. The acceptable change in the KS statistic can then be determined by studying the CDF, as shown in Figures E.1a and E.1b.

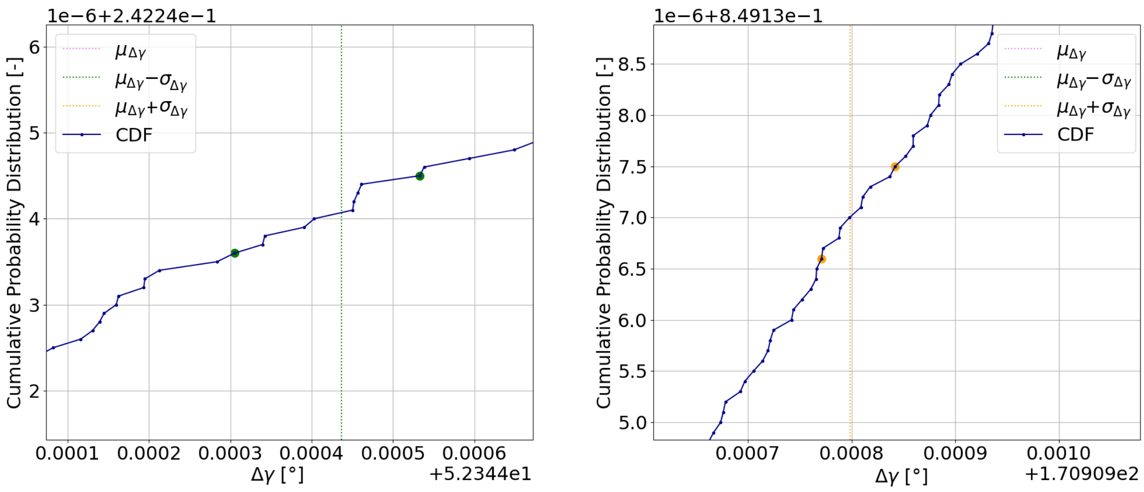

(a) CDF zoomed in on $\mu_{\Delta\gamma} - \sigma_{\Delta\gamma}$.

(b) CDF zoomed in on $\mu_{\Delta\gamma} + \sigma_{\Delta\gamma}$.

Figure E.1: Cumulative probability distribution as a function of the angle separation, zoomed in.

The gradient ∇ or $\frac{\partial KS}{\partial \Delta\gamma}$ can be found at the relevant point in the CDF. The allowed change in the angle separation $\Delta\%_{\Delta\gamma}$ was set equal to 0.01. Then the allowed offset in KS ($\Delta\%_{KS}$) can be found using:

$$\Delta\%_{KS} = 0.01\frac{\partial KS}{\partial \Delta\gamma}\Delta\gamma. \tag{E.1}$$

The gradients at $\mu_{\Delta\gamma} - \sigma_{\Delta\gamma}$ and $\mu_{\Delta\gamma} + \sigma_{\Delta\gamma}$ have been taken, and it was found that the former gradient was lower. The acceptable change in KS will thus also be lower, and if the sample size for this case is sufficient, it will thus also be sufficient for the latter case. The gradient was found to be equal to $3.95 \cdot 10^{-3}$. The angle was found equal to $50.6°$, and the allowed change in $\Delta\gamma$ was set to 1%. The allowed change in KS was found to be equal to: 0.0021.

The total sample sizes used is equal to 10 million samples. The samples sizes tested are $N_s = 100000$, 200000, 400000, 1000000, 2000000, 4000000. The number of times for which the sets are subsampled are equal to $N_R = 3200,\ 1600,\ 80,\ 320,\ 160,\ 96$ [35]. The KS-statistics can be seen in Figure E.2b. As can be seen in the figure, a sample size larger than 1 million is sufficient. As these result might change for every individual case and run, a sample size of 4 million samples is used to determine the uncertainty on the $\sigma_{\Delta\gamma}$.

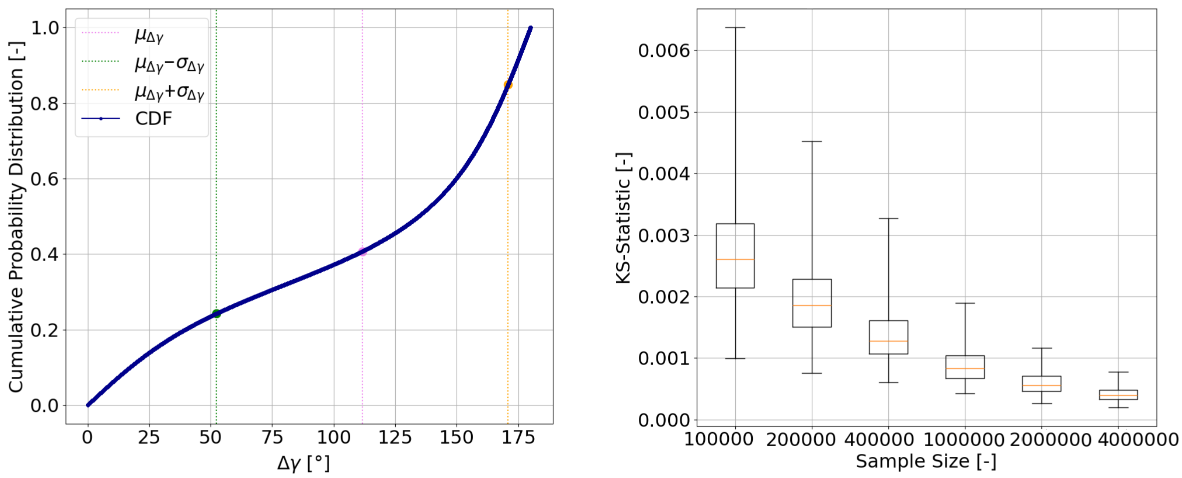

(a) CDF as a function of $\Delta\gamma$.

(b) KS statistic as a function of the sample size.

Figure E.2: CDF and KS statistic for the transformation of the initial uncertainty to the angular uncertainty.

F

Derivation Relative Orbital Parameters

F.1. Relative Eccentricity and Inclination Vectors

To find the relative eccentricity vector, the individual eccentricity vectors of both orbits can be used. From Figure 3.4a it can be observed that the eccentricity vector can be found with [34]:

$$\vec{e} = e \begin{bmatrix} \cos\omega \\ \sin\omega \end{bmatrix}. \tag{F.1}$$

The relative eccentricity vector can then be found with:

$$\Delta\vec{e} = \vec{e}_2 - \vec{e}_1. \tag{F.2}$$

Based on Figure 3.4a, the relative eccentricity vector can also be expressed as:

$$\Delta\vec{e} = \delta e \begin{bmatrix} \cos(\pi - \varphi) \\ \sin(\pi - \varphi) \end{bmatrix} = \delta e \begin{bmatrix} \cos(\varphi) \\ \sin(\varphi) \end{bmatrix}. \tag{F.3}$$

Earlier researchers have derived the relative inclination vector from Figures 3.4b and F.1 using spherical geometry.

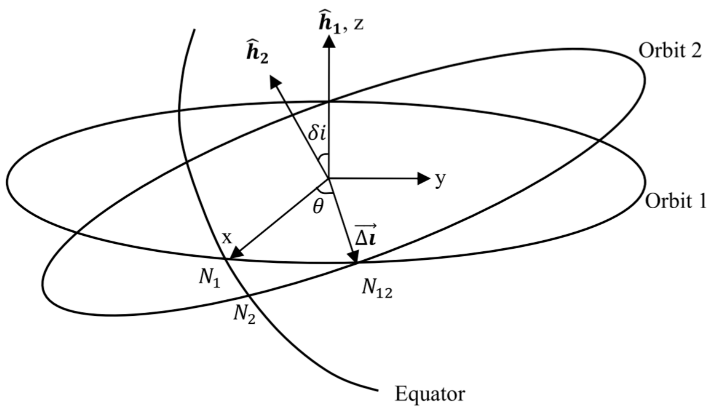

Figure F.1: Geometry of two orbits, with the relative inclination vector indicated, from Reference [34].

Specifically, it has been found that the relative inclination vector can be expressed as [34]:

$$\Delta\vec{i} = \sin\delta i \begin{bmatrix} \cos\theta \\ \sin\theta \end{bmatrix}. \tag{F.4}$$

This relative inclination vector can then be further approximated. That is, by using the spherical sine rule, one can observe that the length of N_1 to N_{12} can be expressed as θ, and by observing that the undefined angle at N_2 is equal to $\pi - i_2$, it can be found that:

$$\frac{\sin \delta i}{\sin \Delta\Omega} = \frac{\sin(\pi - i_2)}{\sin \theta}. \tag{F.5}$$

Using the fact that $i_1 \approx i_2 = i$, $\sin \Delta\Omega \approx \Delta\Omega$ and $\sin(\pi - i) = \sin \pi \cos i - cos\pi \sin i = \sin i$, it can be found that [34]:

$$\sin \delta i \sin \theta = \Delta\Omega \sin i. \tag{F.6}$$

This leads to:

$$\Delta\vec{i} = \sin \delta i \begin{bmatrix} \cos\theta \\ \sin\theta \end{bmatrix} = \begin{bmatrix} \sin\delta i \cos\theta \\ \Delta\Omega \sin i \end{bmatrix}. \tag{F.7}$$

As $\Delta\vec{i}$ can also be expressed as $\Delta\vec{i} = \begin{bmatrix} \Delta i_x \\ \Delta i_y \end{bmatrix}$, the simplified expression for Δi_x can be found using the norm of the inclination vector:

$$|||\Delta\vec{i}||^2 = \Delta i^2 = \Delta i_x^2 + \Delta i_y^2 = \Delta i_x^2 + \Delta\Omega^2 \sin^2 i. \tag{F.8}$$

Due to the small angle $\Delta\Omega$, Δi_x can be approximated as:

$$\Delta i_x \approx \Delta i. \tag{F.9}$$

Thus, the following simplification can be found:

$$\Delta\vec{i} = \sin \delta i \begin{bmatrix} \cos\theta \\ \sin\theta \end{bmatrix} \approx \begin{bmatrix} \Delta i \\ \Delta\Omega \sin i \end{bmatrix}. \tag{F.10}$$

F.2. RTN Separations

Using these relative eccentricity and inclination vectors, the separations in the RTN frame can be found. For the separation in the radial direction, a formula given in the book written by Junkins and Schaub [44] can be used [34]:

$$\frac{dM}{dE} = \frac{r}{a} = 1 - e\cos E. \tag{F.11}$$

This can be approximated as [34]:

$$\frac{r}{a} \approx 1 - e\cos M. \tag{F.12}$$

With M equal to the mean argument of latitude $M = u - \omega$. By making use of trigonometric functions, the equation reads:

$$\frac{r}{a} \approx 1 - e\cos(u-\omega) = 1 - e(\cos u \cos\omega + \sin u \sin\omega) = 1 - e\cos u\cos\omega - e\sin u \sin\omega. \tag{F.13}$$

Substituting the values for Δe_x and Δe_y, this can be written as:

$$\frac{r}{a} \approx -(e_x)\cos u - (e_y)\sin u. \tag{F.14}$$

Now, the goal is the get the radial separation, thus $\frac{\Delta r}{a}$, this can be found by calculating:

$$\frac{\Delta r_R}{a} = \frac{r_2 - r_1}{a} \approx (1 - e_{x_2} \cos u - e_{y_2} \sin u) - (1 - e_{x_1} \cos u - e_{y_1} \sin u) \tag{F.15}$$

Leading to:

$$\frac{\Delta r_R}{a} \approx -\Delta e_x \cos u - \Delta e_y \sin u. \tag{F.16}$$

Furthermore, the semi-major axis drift also contributes according to

$$\frac{\Delta r_R}{a} \approx \frac{\Delta a}{a}. \tag{F.17}$$

For the separation in the along-track direction, D'Amico et al. have stated that the following can be shown [19]:

$$\nu - M = 2e \sin M = (-2e_y) \cos u + (2e_x) \sin u. \tag{F.18}$$

With ν the true anomaly. This leads to [19]:

$$\frac{\Delta r_T}{a} \approx (\nu_2 - M_2) - (\nu_1 - M_1) = (-2\Delta e_y) \cos u + (2\Delta e_x) \sin u. \tag{F.19}$$

The drift in the semi-major axis and argument of latitude also contribute to this term, according to [19]:

$$\frac{\Delta r_T}{a} \approx \Delta u - \frac{3}{2} \left(\frac{\Delta a}{a} \right) (u - u(t_0)). \tag{F.20}$$

Using Figure 3.4b it can be seen that the cross-track separation Δr_N can be found with [34]:

$$\frac{\sin(\pi/2)}{\sin(u_2 - \theta)} = \frac{\sin \delta i}{\sin(\frac{\Delta r_N}{a})}. \tag{F.21}$$

Then, $\sin(\pi/2)$ is equal to 1, and the small angle approximation can be used for the cross-track separation ($\sin(\frac{\Delta r_N}{a}) \approx \frac{\Delta r_N}{a}$ as $a \ll r_N$), thus [34]:

$$\frac{\Delta r_N}{a} \approx \sin \delta i \sin(u_2 - \theta). \tag{F.22}$$

With $u_1 \approx u_2 = u$ and $\sin(u - \theta) = \sin u \cos \theta - \cos u \sin \theta$ one gets [34]:

$$\frac{\Delta r_N}{a} \approx \sin \delta i (\sin u \cos \theta - \cos u \sin \theta). \tag{F.23}$$

Substituting in the values found for Δi_x and Δi_y, this yields [34]:

$$\frac{\Delta r_N}{a} \approx (\Delta i_x) \sin u + (-\Delta i_y) \cos u. \tag{F.24}$$

The separation equations can then be put back in their polar representations to get insight into the angle difference. By assuming $\sin \delta i \approx \delta i$, Equation F.22 can be written as [34]:

$$\frac{\Delta r_N}{a} \approx \delta i \sin(u - \theta). \tag{F.25}$$

And Equation F.26 can be filled in with Equation F.3 to find [34]:

$$\frac{\Delta r_R}{a} \approx -\delta e \cos\varphi \cos u - \delta e \sin\varphi \sin u = -\delta e \cos(u - \varphi). \tag{F.26}$$

Lastly, Equation F.19 can be written as [19]:

$$\frac{\Delta r_T}{a} \approx 2\delta e \sin(u - \varphi). \tag{F.27}$$

The angles φ and θ in these polar representations can be found using Equation F.3 and Equation F.10.

F.3. Relation to Clohessy–Wiltshire Equations

Note the relation to the bounded CW equations, which are given by [44]:

$$\begin{aligned} \Delta r_R(t) &= A_0 \cos(nt + \alpha), \\ \Delta r_T(t) &= -2A_0 \sin(nt + \alpha), \\ \Delta r_N(t) &= B_o \cos(nt + \beta). \end{aligned} \tag{F.28}$$

As can be seen, $A_0 = a\delta e$ and $B_0 = a\delta i$. The relation of α and β can be found by using the following trigonometric functions: $\cos(-x) = \cos(x)$, $\sin(-x) = -\sin(x)$ and $\cos(\pi - x) = -\cos(x)$. Then, as $u = \omega + M$ and $M = M_0 + nt$, for the radial separation, it can be found that:

$$\begin{aligned} \Delta r_R &= -a\delta e \cos(u - \varphi) \\ &= a\delta e \cos(\pi - (u - \varphi)) \\ &= a\delta e \cos(\pi - u + \varphi) \\ &= a\delta e \cos(\pi - \omega - M + \varphi) \\ &= a\delta e \cos(\pi - \omega - M_0 - nt + \varphi) \\ &= a\delta e \cos(-nt + (\pi - \omega - M_0 + \varphi)) \\ &= a\delta e \cos(nt - (\pi - \omega - M_0 + \varphi)). \end{aligned} \tag{F.29}$$

And thus, since $A_0 = \delta a e$, from Equation F.28 it can be found that $\alpha = \omega + M_0 - \pi - \varphi$. As $u_0 = \omega + M_0$, it can be concluded that $\alpha = u_0 - \pi - \varphi$. Using α, based on Δr_T it can be derived that $\Delta r_{T_{off}} = a\delta u$.

Similarly, additionally using the trigonometric function $\sin\left(x + \frac{\pi}{2}\right) = \cos x$, the expression for β can be found by starting with the fact that:

$$\begin{aligned} \Delta r_N(t) &= B_o \cos(nt + \beta) \\ &= B_o \sin\left(nt + \beta + \frac{\pi}{2}\right). \end{aligned} \tag{F.30}$$

Hence, since $B_0 = a\delta i$:

$$\begin{aligned} u - \theta &= nt + \beta + \frac{\pi}{2} \\ \rightarrow \beta &= u - \theta - nt - \frac{\pi}{2} \\ &= u - \theta - (M - M_0) - \frac{\pi}{2} \\ &= \omega - \theta + M_0 - \frac{\pi}{2} \\ &= u_0 - \theta - \frac{\pi}{2}. \end{aligned} \tag{F.31}$$

So, the relation between the relative eccentricity and inclination vectors and the bounded CW equations are given by: $A_0 = a\delta e$, $B_0 = a\delta i$, $\alpha = u_0 - \pi - \varphi$, $\beta = u_0 - \theta - \frac{\pi}{2}$. Thus, based on β and α, it could also be determined whether a situation is risky or not.

G
Distance Metrics

Distance metrics are also important for conjunction analysis. The miss distance defines how close two satellites are together at the time of closest approach. There are actually many distance metrics that could could be used for the calculation of the miss distance. A metric, or metric space, needs to adhere to three different axioms. The metric [82]:

$$d : X \times X \to \mathbb{R}, \tag{G.1}$$

needs to adhere to the following requirements:

1. $d(x_1, x_2) = 0 \Leftrightarrow x_1 = x_2$,
2. $d(x_1, x_2) = d(x_2, x_1)$,
3. $d(x_1, x_3) \leq d(x_1, x_2) + d(x_2, x_3)$.

The most common distance metric that is known is the Euclidean distance, defined as: $r_d = ||\vec{r}_2 - \vec{r}_1||$. When determining the difference between two orbits, both orbits have uncertainties. This difference in uncertainties needs to be compensated for, which can be done by normalizing the distance. If this uncertainty follows a multivariate "normal" distribution this normalized distance is called the Mahalanobis distance [80]. The Mahalanobis distance is defined as:

$$d_M = \sqrt{(\vec{r}_2 - \vec{r}_1)^T \mathbf{P}^{-1} (\vec{r}_2 - \vec{r}_1)}. \tag{G.2}$$

Where $\mathbf{P} = \mathbf{P_1} + \mathbf{P_2}$. This distance metric can also be defined using the local orbital RTN frame [80]. When the reference frame is based on the curved trajectory of the satellite at the origin of the frame, one speaks of curvilinear coordinates [80].

Apart from spaceflight, distance metrics are often used in astronomy. One research topic in astronomy for which a distance metric is needed, is when one wants to see whether meteoroids are originating from the same parent body. Such parent bodies could be for example comets or asteroids [50]. To this extent, the orbits of the meteoroids are studied together with the difference between them. For astronomy purposes, often a five-dimensional space is spanned for the problem. The place of the object in the orbit, defined by the true anomaly, is not important when determining whether two orbits share the same origin. For spaceflight purposes however, especially conjunction analysis, the place in the orbit cannot be neglected [80]. So, metrics defined below for astronomy purposes, will later in this subsection be expanded for spaceflight purposes.

Kholshevnikov et al. defined new natural metrics which can be used for astronomy, since the metrics that are currently often used in astronomy do not fulfill all three axioms and the metrics can often not be used for circular orbits [50]. Two vectors are defined, given by $\vec{u}$ and $\vec{v}$, that are aligned with the angular momentum vector $\vec{h}$ and the Laplace-Runge-Lenz vector $\left(\frac{\vec{r} \times \vec{h}}{\mu} - \frac{\vec{r}}{||\vec{r}||}\right)$. The vectors differ in lengths from these two vectors, the lengths are given by: $||\vec{u}|| = \sqrt{p}$ and $||\vec{v}|| = e\sqrt{p}$, with p equal to semi-latus rectum. The vectors are defined by [50]:

$$\vec{\vec{u}} = \begin{bmatrix} \sin i\sqrt{p}\sin\Omega \\ -\sin i\sqrt{p}\cos\Omega \\ \cos i\sqrt{p} \end{bmatrix}, \ \vec{\vec{v}} = \begin{bmatrix} e\sqrt{p}(\cos\omega\cos\Omega - \cos i\sin\omega\sin\Omega) \\ e\sqrt{p}(\cos\omega\sin\Omega - \cos i\sin\omega\cos\Omega) \\ \cos i\sqrt{p} \end{bmatrix}. \tag{G.3}$$

The distance metric is then given by [50]:

$$d = \sqrt{\frac{(\vec{\vec{u}}_2 - \vec{\vec{u}}_1)^2 + (\vec{\vec{v}}_2 - \vec{v}_1)^2}{L}}. \tag{G.4}$$

The scalar L represents a an arbitrary factor. It was found that this metrics can be used to find the distance between two close orbits for near-Earth objects [50]. As noted by Vananti et al. (2023), this metric as created for astronomical research should be extended with a measure for the position on the orbit for spaceflight purposes. So, the orbital anomaly should be added in the equation. This can be done by adding a vector $\vec{\vec{\omega}}$, for which the alignment of $\vec{\vec{\omega}}_1$ and $\vec{\vec{\omega}}_2$ is given by $||M_2 - M_1||$, and the length of the vector is again equal to $||\vec{\vec{\omega}}|| = \sqrt{p}$ [80]. Then,

$$d = \sqrt{(\vec{\vec{u}}_2 - \vec{\vec{u}}_1)^2 + (\vec{\vec{v}}_2 - \vec{\vec{v}}_1)^2 + (\vec{\vec{w}}_2 - \vec{\vec{w}}_1)^2}. \tag{G.5}$$

Maruskin (2010) also developed a natural distance metric, which is not affected by singularities in the orbit. So the metric can be used for orbits that are rectilinear ($e = 1$), circular ($e = 0$) or have zero-inclination ($i = 0°$) [53]. The derivation of the metric can be found in Reference [53], the result is given below:

$$d = \sqrt{2(a_1^2 + a_2^2 - 2a_1a_2\cos\Delta\psi)}. \tag{G.6}$$

With:

$$\Delta\psi = \sqrt{\frac{\arccos^2(\vec{\eta}_1 \cdot \vec{\eta}_2) + \arccos^2(\vec{\xi}_1 \cdot \vec{\xi}_2)}{2}}. \tag{G.7}$$

Here $\vec{\eta}$ is equal to the sum of the Laplace-Runge-Lenz vector and the normalized angular momentum vector $\left(\frac{\vec{h}}{\sqrt{\mu a}}\right)$ and $\vec{\xi}$ is equal to the difference between the two. When expanding this equation with the orbital anomaly, Equation G.7 reads:

$$\Delta\psi = \sqrt{\frac{\arccos^2(\vec{\eta}_1 \cdot \vec{\eta}_2) + \arccos^2(\vec{\xi}_1 \cdot \vec{\xi}_2) + (M_2 - M_1)^2}{3}}. \tag{G.8}$$

With M the mean anomaly. In a similar method as for the metric of Kholshevnikov et al., the Mahalanobis distance can also be found for this metric [80].

It must be noted, that in the application as Vananti et al. [80] has defined, the distance metrics are used for tracklet linking. Tracklets are short observations of an orbit. Often there are multiple tracklets for a space debris orbit. To determine whether the tracklets are a part of the same orbit, the distance between the tracklets can be found [80]. It must be noted that for this application, all the parameters of the tracklets need to be the same. Then it can be concluded that the tracklets are pieces of the same orbit. This is not the case for a conjunction analysis, two objects only need to intersect each other's orbit. Hence, only the positions of the two objects need to be close or the same. In general, the velocities are expected to be different. This complication led to the decision to not pursue this metric during this research. It could be an interesting topic for further research however.

H

Survey on Data Usage in Conjunction Analysis

In this appendix, the survey is presented. Some figures and references are repeated here, to show the complete survey as presented to the operators. Note, the reference numbers are altered here to match the references in the bibliography.

Introduction
Thank you for participating in this survey. The goal of this survey is to gather insights into the use of Conjunction Data Messages in conjunction analysis. Your input is valuable for understanding current practices and exploring how existing warnings could be enhanced with new risk assessment metrics. The survey consists of four parts and will take approximately 20 minutes to complete. All responses will remain anonymous, and the results will contribute to a publicly available thesis project conducted at TU Delft in collaboration with TNO.

Q1 (Single Choice): Do you agree to the use of your responses in the thesis?

Yes	No

Part I: General
In this section the questions are focused on collecting general information.

Q2 (Multiple Choice): In which orbital regime are you operating?

Low Earth Orbit (LEO)	Medium Earth Orbit (MEO)	Geostationary Orbit (GEO)	Highly Eccentric Orbit (HEO)

Q3 (Open): On how many satellites are you operating?

...

Q4 (Open): How many Conjunction Data Messages (CDMs) do you approximately get per month?

...

Q5 (Open): How many collision avoidance maneuvers do you approximately execute per month?

...

Part II: Collision Warnings
In this section, we are interested in whether you use Conjunction Data Messages for conjunction analysis and want to gather your opinion on these.

Q6 (Single Choice): Do you use Conjunction Data Messages (CDMs) for conjunction analysis?

Yes | No

Q7 (Single Choice): Do you use other (extra) data types for conjunction analysis?

Yes | No

Q8 (Open): If so, which data types? Select 'N/A' if previous answer was 'No'.

... || N/A

Q9 (Single Choice): Based on a scale from 0 to 10, to what extent do you consider the current CDMs effective?

1 | 2 | 3 | 4 | 5 | 6 | 7 | 8 | 9 | 10 || N/A

Q10 (Multiple Choice): Which type of actions have you taken based on CDMs?

Re-screening the conjunction with owner/ operator ephemeris	Gathering refined tracking data of the objects	Reassessing the collision probability	Executing a collision maneuver	N/A

Q11 (Open): How do you use the given CDMs to determine whether one of these actions needs to be taken?

... || N/A

Q12 (Multiple Choice): Which data aspect in the CDMs do you consider leading in the decision to take an action?

- Re-screening the conjunction with owner/operator ephemeris:

  Probability of collision | Miss distance | Time of closest approach | Covariance || N/A

- Gathering refined tracking data of the objects:

  Probability of collision | Miss distance | Time of closest approach | Covariance || N/A

- Reassessing the collision probability:

  Probability of collision | Miss distance | Time of closest approach | Covariance || N/A

- Executing a collision avoidance maneuver:

  Probability of collision | Miss distance | Time of closest approach | Covariance || N/A

Q13 (Open): What do you consider the biggest limitations of current CDMs and/or conjunction analysis in general?

... || N/A

Q14 (Open): What additional information given in a CDM would you find helpful?

... || N/A

Q15 (Single Choice): Do you think there is too much information provided to operators?

Yes | No || N/A

Q16 (Open): If previous question was answered with 'Yes', what information could be left out of the CDMs?

... || N/A

Part III: Risk Assessment Metrics
Part of the thesis research focuses on studying novel collision risk assessment methods that can be used for conjunction analysis. Furthermore, when using multiple different risk metrics, we are interested in how these different metrics could be presented to operators. In this section, two proposed methods are briefly introduced.

Geometry can be used for assessing the collision risk between two objects. In former research on formation control and safe proximity operations [19] it has been found that the relative inclination and eccentricity vectors, which describe the orientation and shape differences between two orbits, can help to quantify the separation between the objects. Specifically, when these relative vectors are parallel to each other, either the radial or cross track separation is maximal. Whilst an orthogonal alignment of the vectors indicates that both of these separations could vanish jointly, indicating a more risky conjunction. This is depicted in Figure 3.7.

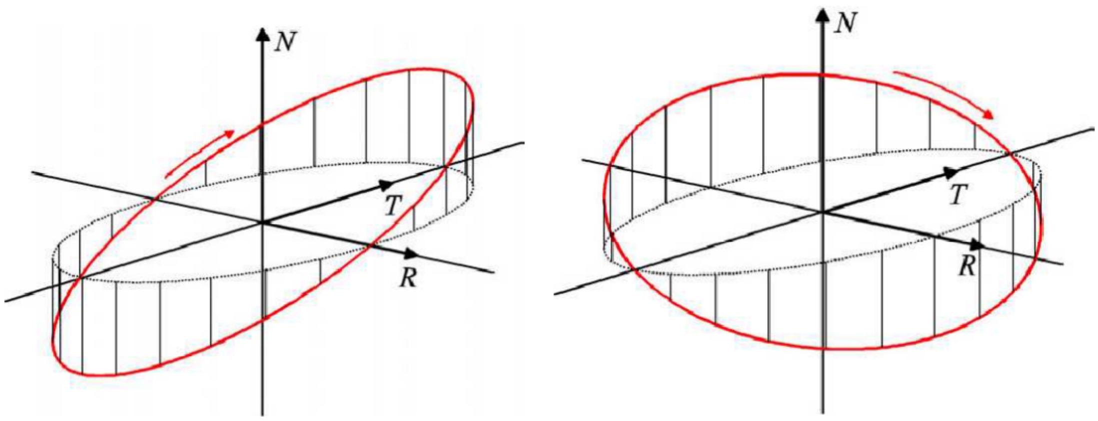

Figure H.1: Geometry of parallel (left) and orthogonally (right) aligned orbits. Source: [56]

The risk is analysed based on the angle between the relative eccentricity and inclination vectors. Currently we are studying to what extent this metric can be used for conjunction analysis purposes.

Q17 (Single Choice): Would you consider using relative orbital parameters as risk metric?

Yes | No

Q18 (Open): The collision risk is studied based on an angle separation, which has an uncertainty associated to it. How would you want this risk metric to be presented to you? For example, presenting both the expected angle and the associated confidence interval, or by displaying only the angle associated with the highest collision probability?

... || N/A

Another risk assessment that is studied is the outer probability measure metric [21]. A known issue with standard collision probability calculations is that the metric is not reliable when the uncertainty is high. To mitigate this issue, outer probability measures provide a method of qualifying the risk based on two bounds, that represent the upper probability of collision and the lower probability of collision. These bounds can be used to determine whether the information available on the space objects is sufficient for a reliable collision assessment. Operators can set a threshold that represents the acceptable probability of collision, such that:

- When both bounds are below the set threshold, the risk can be qualified as acceptable.
- When both bounds are above the threshold, the risk is non-acceptable.
- When the threshold lies in between the two bounds, the information on the conjunction is not sufficient, and the risk is undetermined.

We are currently studying whether this metric can be incorporated in current conjunction analysis and how it might complement the previously introduced geometric metric.

Q19 (Single Choice): Would you consider using outer probability measures as risk metric?

Yes | No

Q20 (open): How would you want this risk metric to be presented to you?

... || N/A

Sources:

[19] D'Amico, S. and Montenbruck, O., "Proximity Operations of Formation-Flying Spacecraft Using an Eccentricity/Inclination Vector Separation". In: Journal of Guidance, Control, and Dynamics 29.3 (2006), pp. 554–563.

[56] Montenbruck, O., Kirshner, M., and D'Amico, S., "E-/I-Vector Separation for GRACE Proximity Operations," DLR/German Space Operations Center, TN 04-08, Oberpfaffenhofen, Germany, 2004.

[21] Delande, E. D., Jones, B. A. and Jah, M. K., "Exploring an Alternative Approach to the Assessment of Collision Risk". In: Journal of Guidance, Control, and Dynamics 46.3 (Mar. 2023), pp. 467–482

Part IV: Enhanced Collision Warnings

In this section, we are looking for insights into how multiple different risk assessment metrics can be combined to provide useful and effective collision warnings for operators.

Q22 (Single Choice): If multiple different risk assessments would be used, would you want to see them all, or only the one representing the highest risk?

All risk metrics | Only the one representing the highest risk || N/A

Q23 (Open): How do you think the data should be structured if multiple risk metrics would be represented?

... || N/A

Q24 (Single Choice): Would you prefer receiving the quantitative results of a metric, or would you prefer a qualitative representation of the results?

Quantitative | Qualitative || N/A

Q25 (Single Choice): Do you want an action advice?

Yes | No

Thank you for your time and valuable input. Your responses are greatly appreciated. If you have any other remarks before submitting your answers, please provide them below.

Q26 (Open): Additional comments:

... || N/A

I

Run Matrix

Table I.1: Overview of the various test cases simulated.

Case	Miss Type	Object 1	Object 2	C_d	Noise	$P_{c_{Elrod}}$	$P_{c_{Hall}}$	$P_{c_{max}}$	$P_{c_{MC}}$	$\Delta\gamma$	OPM
1	Collision	Satellite	Satellite	·1.0		x		x			x
1	Collision	Satellite	Satellite	·0.9		x		x			x
1	Collision	Satellite	Satellite	·1.0	x	x		x			x
1	Collision	Satellite	Satellite	·0.9	x	x		x			x
1	Collision	Satellite	Debris	·1.0		x		x			x
1	Collision	Satellite	Debris	·0.9		x		x			x
1	Collision	Debris	Debris	·1.0		x		x			x
1	Collision	Debris	Debris	·0.9		x		x			x
1	Near Miss	Satellite	Satellite	·1.0		x		x			x
1	Near Miss	Satellite	Satellite	·0.9		x		x			x
1	Near Miss	Satellite	Debris	·1.0		x		x			x
1	Near Miss	Satellite	Debris	·0.9		x		x			x
1	Near Miss	Debris	Debris	·1.0		x		x			x
1	Near Miss	Debris	Debris	·0.9		x		x			x
1	Large Miss	Satellite	Satellite	·1.0		x		x			x
1	Large Miss	Satellite	Satellite	·0.9		x		x			x
1	Large Miss	Satellite	Debris	·1.0		x		x			x
1	Large Miss	Satellite	Debris	·0.9		x		x			x
1	Large Miss	Debris	Debris	·1.0		x		x			x
1	Large Miss	Debris	Debris	·0.9		x		x			x
2	Ideal	Satellite	Satellite	·1.0		x	x			x	

J CDM Identifiers

Table J.1: Identifiers of the CDMs used in this research.

Testcase	#Conjunction	Message Id
1	1	Privateer_2024 − 08 − 16T02 : 58 : 54.609134_50204_52605
2	1	Privateer_2024 − 09 − 13T00 : 33 : 03.972916_31698_36605
2	2	Privateer_2024 − 09 − 13T00 : 36 : 16.494326_31698_36605
2	3	Privateer_2024 − 09 − 13T02 : 06 : 07.800251_31698_36605
2	4	Privateer_2024 − 09 − 13T02 : 08 : 38.614173_31698_36605
2	5	Privateer_2024 − 09 − 13T03 : 41 : 44.483309_31698_36605
2	6	Privateer_2024 − 09 − 13T03 : 44 : 21.158728_31698_36605
2	7	Privateer_2024 − 09 − 13T05 : 17 : 13.03299_31698_36605
2	8	Privateer_2024 − 09 − 13T05 : 20 : 12.14009_31698_36605
2	9	Privateer_2024 − 09 − 13T06 : 50 : 01.485209_31698_36605
2	10	Privateer_2024 − 09 − 13T06 : 52 : 54.657035_31698_36605
2	11	Privateer_2024 − 09 − 13T08 : 25 : 43.638397_31698_36605
2	12	Privateer_2024 − 09 − 13T08 : 28 : 30.13528_31698_36605
2	13	Privateer_2024 − 09 − 13T10 : 01 : 17.924674_31698_36605
2	14	Privateer_2024 − 09 − 13T10 : 04 : 12.90349_31698_36605
2	15	Privateer_2024 − 09 − 13T11 : 33 : 58.876101_31698_36605
2	16	Privateer_2024 − 09 − 13T11 : 37 : 03.773749_31698_36605